Title
Performance Evaluation and Optimization of a Dual Coaxial-Cylinder System as an Ocean-Wave Energy Converter

Author
Son, Daewoong

Publication Date
2016

Peer reviewed|Thesis/dissertation

Performance Evaluation and Optimization of a Dual Coaxial-Cylinder System as an Ocean-Wave Energy Converter

by

Daewoong Son

A dissertation submitted in partial satisfaction of the

requirements for the degree of

Doctor of Philosophy

in

Engineering - Mechanical Engineering

in the

Graduate Division

of the

University of California, Berkeley

Committee in charge:

Professor Ronald W. Yeung, Chair
Professor Dennis K. Lieu
Professor Francesco Borrelli
Associate Professor Per-Olof Persson

Fall 2016

Performance Evaluation and Optimization of a Dual Coaxial-Cylinder System as an Ocean-Wave Energy Converter

Abstract

Performance Evaluation and Optimization of a Dual Coaxial-Cylinder System as an Ocean-Wave Energy Converter

by

Daewoong Son

Doctor of Philosophy in Engineering - Mechanical Engineering

University of California, Berkeley

Professor Ronald W. Yeung, Chair

This research demonstrates the design, optimization, and control of a dual coaxial-cylinder system as an ocean-wave energy converter (WEC). The coaxial-cylinder system consists of a tension-tethered vertical inner cylinder and an annular outer cylinder heaving along the outer surface of the inner cylinder. The relative heave motion between the two cylinders is used to extract energy from incoming waves. An "in-house developed" permanent-magnet linear generator (PMLG), consisting of an array of magnets mounted on the outer cylinder but moving relative to a set of coils installed inside the inner cylinder, is used to convert the mechanical movement into electrical current, thus functioning as a power take-off (PTO) unit. This research consists of the following phases.

First, the mathematical modeling, component design and fabrication of the WEC hardware, coupled with the PMLG, were developed. Verification of the predictability and viability of this coupling concept was conducted by comparing predictions with physical-model experiments of about 1:24 scale. The modeling is supplemented by relatively simple, experimentally determined, viscosity-related correction factors on theoretical hydrodynamic coefficients of damping and added mass. The wave-exciting force was well predicted. The modeling is successful for free motion of the cylinder in waves.

Second, a series of dry-bench tests on the PMLG unit was used to determine its electromechanical properties. The operating condition that enabled maximum useful power output at heave-motion resonance was investigated as a function of magnet-coil gap width and the output payload in the form of electrical resistance. Moreover, the bottom profile of the annular outer cylinder was modified into a curved shape similar to "The Berkeley Wedge" so as to reduce viscous losses and enhance the WEC performance. Viscous damping losses were reduced by as much as 70%, when compared to a flat-bottom shape. This simple change led to a three-fold increase in the heave amplitude of the outer cylinder and a two-fold increase in power output at resonance, when the WEC system was set at the optimal operating conditions.

Thirdly, to further maximize the energy-extraction capability for a wide operating range of sea-states, a nonlinear model predictive control (NMPC) methodology was developed for the coupled system. The mechanical to electrical power conversion efficiency of the PMLG, determined in Phase 2, was incorporated in this new control scheme. This NMPC process provided a strongly time-dependent PMLG damping profile in time as the control parameter. The typical optimal time-profile of this damping was found to consist of some intermediate value constrained within the specified damping capacity. To confirm the success of this NMPC strategy, this PMLG damping behavior was implemented electronically into the complete WEC system of Phase 1 and 2. The controller employs a solid-state relay based on a pulse-width modulation technique to mimic analog current flow. Experimental verification in regular and irregular sea waves confirmed this successful NMPC implementation. Peak values of energy capture and a broadened bandwidth were favorable compared to that using just passive control.

The present research, all integrated, is capable of producing a 300 kW peak-power system in, say, 3 m wave height of 8.8 sec period using a 12 m diameter WEC device. The estimated overall "wave-to-wire" capture-width efficiency is 32% relative to the diameter of the device, with the generator efficiency accounted for. The wattage goes up as the square of the wave amplitude.

To God
who gives power and strength to His people. I worship and glorify His name.

To my beloved wife, Hyejung Baik,
who has inspired and supported me with prayer, love, patience all the way.

To my beloved daughters, Christina Yuna Son and Grace Jua Son,
who are the joy of the my life.

For a man's ways are before the eyes of the LORD,
and he ponders all his paths. (Proverbs 5:21)

Be strong and courageous, for you shall cause this people to inherit the land
that I swore to their fathers to give them. (Joshua 1:6)

Fear not, for I am with you; I will bring your offspring from the east,
and from the west I will gather you. (Isaiah 43:5)

Contents

List of Figures

List of Tables

Acknowledgments

I would like to express my sincere gratitude to my advisor, Professor Ronald W. Yeung, for giving me this opportunity to engage in the ocean engineering graduate program at Berkeley and for his academic guidance and assistance. I have learned much from him both professionally and personally.

I also would like to thank Professor Dennis K. Lieu, Professor Francesco Borrelli, and Professor Per-Olof Persson for serving on my dissertation committee; Professor Alaa E. Mansour, Professor Ömer Savaş, and Professor J. Karl Hedrick for serving on my qualifying committee.

I am grateful to Nils Koliha for his initial design work on the project, Christophe Cochet and Dr. Fun P. Chau for the hydrodynamics analysis on the dual cylinders. Also, this work would not have been possible without the constant support of Dr. Nathan Tom and Valentin Belissen. Their support allowed the research to progress smoothly. Additionally, I also appreciate my colleagues and friends in the Ocean Engineering Group during my studies at Berkeley.

Finally, I would like to give my deep thank to my parents, Jaechul Son and Boknim Jin, for their love, encouragement, and prayers. Their faith in me gave the strength to stand and receive this honor.

Chapter 1

Introduction

There is a growing concern regarding environmental issues resulting from the use of fossil fuels, and the probable unreliability in its supply has led to an interest in renewable energy. The climate change report of 2014 states that continued emission of greenhouse gases will cause pervasive and irreversible impact on humans and the ecosystem [1]. At the same time, the increase in the global energy demand because of the increasing population and high living standards signifies the importance of research on renewable energy utilization. According to the International Energy Outlook 2011 by the U.S. Energy Information Administration (EIA), the energy consumption of the world will grow by more than 50% from 2008 to 2035 [2].

Covering more than 70% of the earth's surface, the ocean provides enormous energy resources such as ocean thermal, waves, tides, and offshore winds. This research especially focuses on the ocean-wave energy, where there has been considerable amount of interest since the late 1970's because of the oil crisis [3].

1.1 Background

1.1.1 Ocean-Wave Energy Resource

Ocean-waves are generated and derived from wind as it blows over the ocean surface. Once waves are created, they generally travel thousands of kilometers until their energy is dissipated on shores owing to the interaction with the seabed. In fact, worldwide potential of ocean-wave energy is estimated to be 2 TW [4], which is in the same level as that of the current world annual electricity consumption rate. Figure 1.1 shows the global distribution of the annual mean power density and mean best direction for 6-year period, using outputs from the NOAA WaveWatch III [4]. However, evidently, the distribution is not even; high wave energy resources can be found between 30 degree and 60 degree of latitude on both hemispheres, induced by prevailing winds from west to east. It should be noted that the wave power density is expressed as power per unit width of wave crest $[W/m]$.

As a source of promising renewable energy, ocean-wave energy offers significant advantages compared to other energy alternatives such as solar and wind:

1. High energy density

Waves have the highest energy density among renewable energy resources. Solar energy intensity of typically 0.1-0.3 kW/m^2 correlates to a wind energy in the range

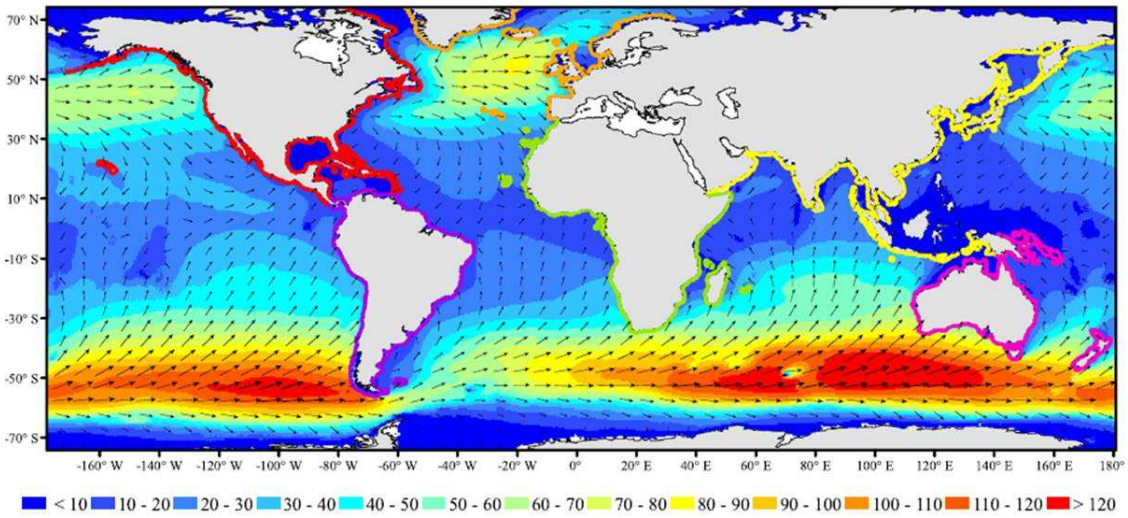

Figure 1.1: Annual average wave power density in kW/m (color) and annual mean best direction (arrow) of power density from [4]

of 2-3 kW/m^2 [5]. However, the wave-energy density level is approximately 20-30 kW/m along the coastline, as seen in Fig. 1.1.

2. Reliable predictability

Ocean-wave is continuous and sea condition can be predicted several days in advance, thus being more easily predictable than wind or solar conditions. Furthermore, the expected monthly variation in the wave energy tends to follow the electricity demand [6].

3. Negligible land use

More than 50% of the global population lives within 100 km of the coastline. Hence, wave energy can reduce the number of transmission lines and reliance on additional power stations [7], which in turn can reduce construction and operation costs.

4. Limited environmental impact

Not only is wave energy generally free from creating air pollution, but it also has low visual and noise impact, particularly for offshore and submerged devices. Furthermore, considering its high energy density, a wave-energy farm may require less area compared to other energy resources. It means that this wave-energy farm has minimal environmental potential impact.

1.1.2 Wave-Energy Converter (WEC) Technology

Although ocean-wave energy represents a fascinating solution as discussed earlier, in contrast to other renewable sources, a wide variety of concepts and designs for wave-energy converters (WECs) are being proposed and examined. This implies that the technology is relatively immature, or is in the research and development phase compared to technologies associated with other resources. The various WEC designs can be categorized by their location or type of operation [3, 8].

Depending on the installation location, the WECs can be categorized according to three different water depths: shoreline devices for less than 10 m, nearshore devices in shallow water around 20 to 30 m, and offshore devices in deep water over 40 m. With the distinction of location, the WEC designs are dependent on the mooring method. A floating device, for example, will be deployed at nearshore or offshore.

Classification of WECs based on the operation type is more widely used. Figure 1.2 illustrates an example for each of the four different types.

1. Attenuator

The attenuator is a type of floating structure that is aligned in parallel to the wave direction. The Pelamis is a well-known example of this type [9]. When it rides the incoming waves, the relative motion at the hinge between the segments is utilized to produce energy.

2. Terminator

The terminator has a principal axis perpendicular to the incident-wave direction in order to intercept waves. The oscillating water column (OWC) is an example, which is installed on shore or nearshore [10]. The water column level fluctuate owing to the wave motion and the trapped air is then compressed and expanded through a turbine. Another prototype implementation of the terminator type utilizing the crashing waves to get hydraulic pressure is now planned in Ghana [11].

3. Overtopping

The overtopping has a reservoir above the sea level. The water captured in the reservoir from the waves is released into the ocean through a low-head hydraulic turbine that generates electrical power. An example of this type is the Wave Dragon [12].

4. Point absorber

The point absorber has a small dimension compared to the wave length. For heaving point absorber, the device oscillates vertically on the surface or below the surface with respect to the reference structure. This relative motion is used to convert

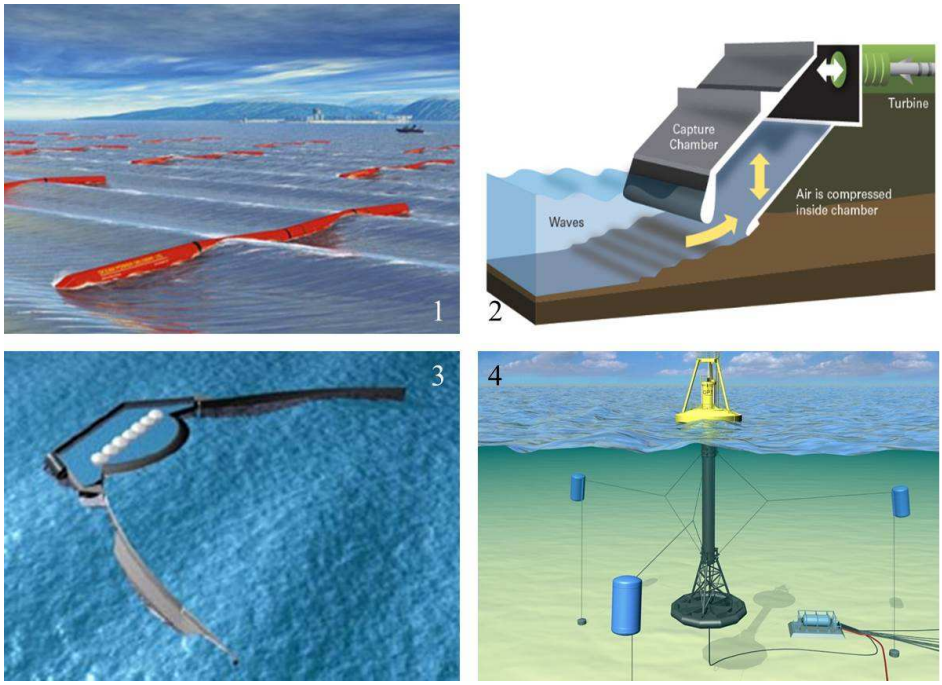

Figure 1.2: Different types of wave energy converters: 1. Pelamis (Attenuator), 2. OWC (Terminator), 3. Wave Dragon (Overtopping), 4. PowerBuoy (Point absorber)

energy from waves to electricity. One typical example of a heaving point-absorber type is the PowerBuoy, Ocean Power Technologies [13].

There are still numerous designs that cannot fit in the above classification. Even within the same group of WECs, various ideas and concepts exist. Some ideas combine the two types such as the heaving point absorber with the additional wings of the attenuator.

1.1.3 Power Take-Off (PTO)

In the process of wave-energy conversion, the wave energy is transferred to the WEC, and subsequently, the absorbed power is converted into useful electrical power. The latter conversion occurs in a power take-off (PTO) unit. The three different types of PTO for energy conversion are considered [3, 8, 14] and seen in Fig. 1.3.

1. Air/Water turbine

In this method, a turbine is deployed along the flow of fluid. The working fluid drives the turbine that is connected to an electrical generator. The bi-directional air turbine, called the Wells turbine, is widely used in OWC devices. For overtopping devices, a water turbine, such as the Kaplan turbine, is often used.

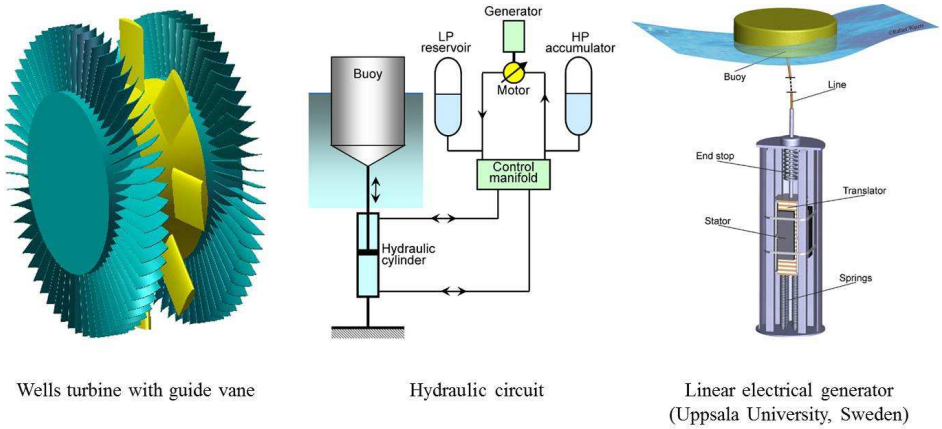

Figure 1.3: Different types of power take-off from [8]

2. Hydraulics

Waves apply large forces at low speeds. The hydraulic circuit delivers the absorbed power into the hydraulic motor to drive an electrical generator. The hydraulic PTO can be found in several types of WECs such as the Pelamis and the PowerBuoy.

3. Direct drive

The direct drive consists of a moving part named a translator and a stator containing coils. It directly converts mechanical energy into electrical energy, with no intermediate steps that exist in other PTOs. A linear generator is used in the heaving point-absorber WEC, where the translator moves with a heaving part, and the stator is mounted on a relatively stationary part.

1.2 Scope and Objectives

To harness ocean-wave energy, several technologies have been studied and proposed in recent years. As there is no predominant solution for wave-energy extraction, research on the WEC design is still quite active. In this study, a dual coaxial-cylinder system of a point absorber is considered. The inner cylinder is tension-tethered to the seabed or moored, while the annular outer cylinder floats and slides freely in the vertical direction. This design is operable without mounting on any fixed platform in the open ocean-environment. In addition, the axisymmetric point-absorber WEC can be set in resonance with the incident waves and is insensitive to the incoming-wave direction.

The two-body heaving devices that are most similar to ones used in this study can be found in Fig. 1.4; L10 Buoy of Oregon State University [15], PowerBuoy of Ocean Power

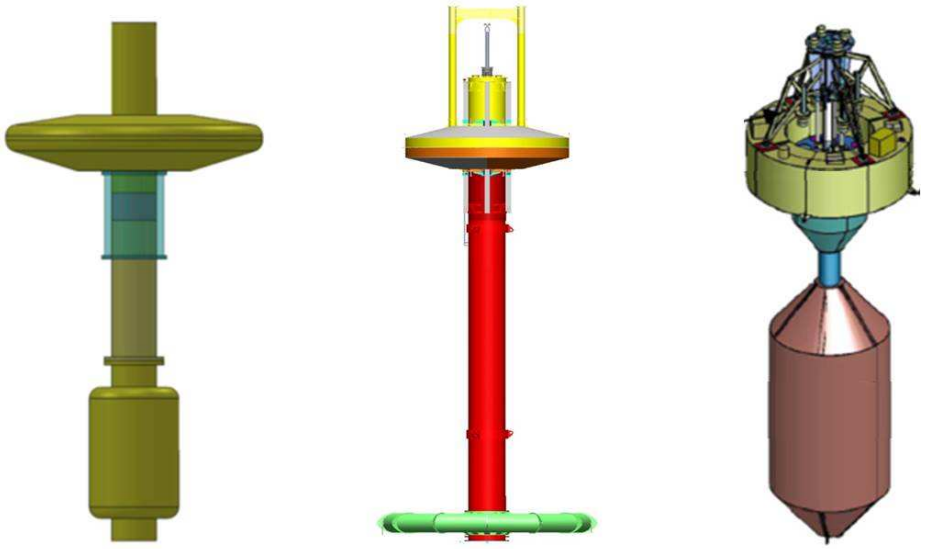

Figure 1.4: Two-body heaving point absorber wave energy converter

Technologies [13], and Wavebob [16]. Typically, the outer body of such two-body devices has a design consisting of a very high radius-draft ratio. However, the design proposed here has a low radius-draft ratio so that it can fit our experimental facility for ease of validation of the theoretical model. This lower radius-draft ratio, i.e., a deeper draft and smaller radius, leads to larger energy extraction capabilities [17].

This type of two-body heaving WEC, which is compact and self-contained, extracts wave energy by the relative heave motion using a PTO system installed between the two bodies. A direct-drive conversion system would be superior to any moving mechanical parts that involve gearing and hydraulics. For this purpose, a permanent-magnet linear generator (PMLG) is used, which includes a translator of a magnet array and a stator with coils. The in-house PMLG for this study was designed and investigated in detail for a single heaving point absorber, observed in [18], and illustrated in Fig. 1.5.

The WEC is equipped with a PTO unit that coverts the absorbed mechanical power into useful electrical power. The PTO force contributes to the motion of the mechanical system as well as to power generation. Once the WEC geometry is generally fixed, the mass and spring are considered to be constant. Moreover, the PTO setting can be tuned for efficient power extraction. An active or passive method is used to control the PTO. The passive control considers the time-averaged conditions, and therefore, eliminates the need for estimating subsequent waves [19]. The PTO damping is set to be an optimal constant value over the time during which passive control is utilized. The active control, on the other hand, optimizes the PTO setting to each wave train. The passive control is easy to understand

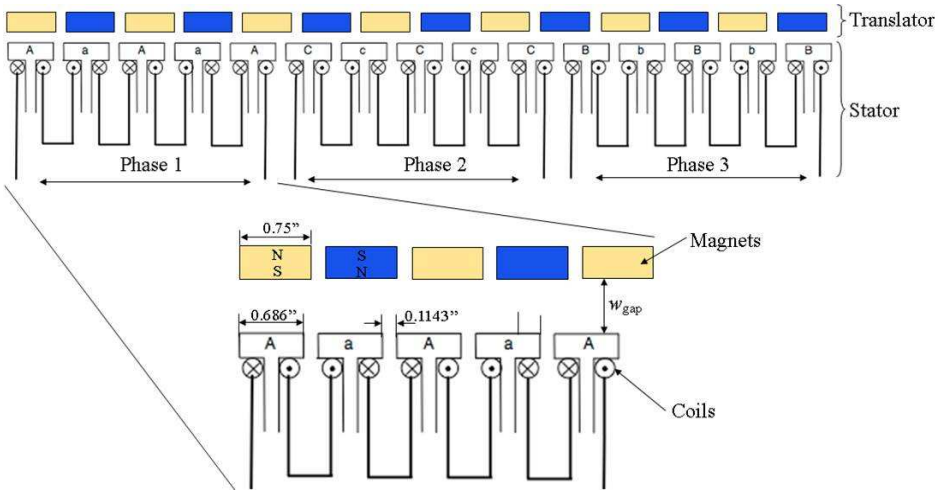

Figure 1.5: Schematic of PMLG configuration for one side from [18]

and yields a fairly simple control system, but results in low efficiency when compared to the active control strategy [20].

In summary, the aim of this research is to design a dual coaxial-cylinder WEC, using a PMLG as the PTO, and evaluate its performance in extracting energy. A further objective of this study is to optimize the system to maximize electrical power generation. The study describes the improvement of the WEC system, its enhanced the performance, and the active control of the PMLG damping as a control parameter, or more likely control time-profile function.

1.3 Outline of the Dissertation

The work is outlined in the following chapters.

Chapter 2 summarizes the mathematical modeling based on the floater hydrodynamics for the coaxial-cylinder coupled with the PMLG. In addition, it covers the energy conversion from wave to wire. This theoretical background provides predictions of WEC performance and potential directions for system optimization.

Chapter 3 is divided into two parts. The first part of the chapter provides details of the developed dual coaxial-cylinder WEC and customization of the PMLG unit that is suitable for the floating system. The second part provides characteristics of the PMLG in terms of the controllable PMLG damping and power conversion efficiency.

Chapter 4 provides optimizing the system through the bottom-shape modification of the floater and determining the optimal operating condition of the PMLG. In addition, it presents the experimental results of the coupled system in regular waves. The motion response of the floater and power extraction are compared with the theoretical predictions in the frequency domain. It also demonstrates the extent to which the performance improvements are achieved

by optimizing the bottom shape of the floater and the constant and continuous damping value of the PMLG.

Chapter 5 introduces the active control method using the model predictive control (MPC) methodology to maximize energy extraction, considering the mechanical to electrical power conversion efficiency of the PMLG. The time-domain modeling of the coupled system and constrained nonlinear-optimization problem are formulated. It provides the optimal time-varying PMLG damping values as the control parameter, and the improved performance from applying active control is compared against the passive control method for both regular and irregular waves.

Chapter 6 presents the implementation of the offline nonlinear-MPC (NMPC) results into a lab-scale model. First, the controller is proposed to manipulate the time-varying PMLG damping using a solid-state relay (SSR) and pulse-width modulation (PWM) techniques. The dry-bench tests for the chosen controller investigate the tuning mechanism of the PMLG damping value. The wet-test experiments of the NMPC-controlled system verify that there are increases in useful power extraction for both regular and irregular waves.

Chapter 7 concludes the dissertation with a summary and contributions as well as a discussion on possible future work.

The novel scientific contributions of this dissertation are summarized as follow. First, this research validates the mathematical wave-to-wire modeling of the point-absorber WEC device coupled with the PMLG, where experimentally determined viscous-related correction factors on hydrodynamic coefficients were inserted. Second, this research provides realistic solutions to optimize the energy extraction capability of the device in aspects of floater design and performance-related variables. Thirdly, this research introduced effective active control strategy using nonlinear model predictive control, incorporating power-conversion efficiency of the PMLG in the control scheme, for the fully coupled system to overcome narrow-banded performance of energy extraction. Finally, this research confirms the successful active control implementation through the proposed controller structure, which electronically control the time-dependent PMLG damping.

Chapter 2

Theoretical Modeling of the WEC System

This chapter reviews the theoretical background on hydrodynamics theory and point-absorber theory [21, 22, 23, 24, 25, 26, 27, 28, 29]. The first section summarizes the formulation for modeling the interaction between incident wave and the floating body. A linear model of the floater with PTO in the frequency domain is introduced, and forces acting on the floating body are analyzed. The solution of the floater's motion is a requisite for the energy extraction modeling in the following section. In the second section, quantification of energy transfer and WEC performance is described. Furthermore, important characteristics for the point-absorber design are explained.

2.1 Floater Hydrodynamics in Frequency Domain

2.1.1 Equation of Motion of the Floater

The schematic of the two coaxial cylinders considered in this study is illustrated in Fig. 2.1. The periodic incident wave propagating in the x-direction is described by elevation $\eta(x,t)$, and the motions of the body $\zeta_i(t)$ are defined as

$$\eta(x,t) = \Re\{Ae^{i(kx-\sigma t)}\} \tag{2.1}$$

$$\zeta_i(t) = \Re\{\mathcal{A}_i e^{i\sigma t}\} \tag{2.2}$$

where $\mathcal{A}_i$ is the complex amplitude of the body motion in the i-direction: surge ($i = 1$), heave ($i = 3$), and pitch ($i = 5$).

Per linear theory, which represents small body motions relative to their draft, this dual coaxial-cylinder behaves as a single body in the surge ($i = 1$) and pitch ($i = 5$), whereas each cylinder has independent heave motion ($i = 3$), decoupled from the surge and pitch motions [27]. Moreover, the tension-tethered inner cylinder is considered to be relatively fixed. Thus, only heave motion of the outer cylinder interacting with incident wave is needed to formulate the system dynamics. It can be modeled as a simple one degree-of-freedom mass, spring, and damper system. The forces acting on the heaving floater can be described by

$$m_2\ddot{\zeta}_3(t) = F_3^{st}(t) + F_3^{exc}(t) + F_3^{rad}(t) \tag{2.3}$$

where m_2, $\ddot{\zeta}_3(t)$ are the displaced mass and the heave acceleration of the outer cylinder. The hydrostatic restoring force is given by

$$F_3^{st}(t) = -K_{33}\zeta_3(t) \tag{2.4}$$

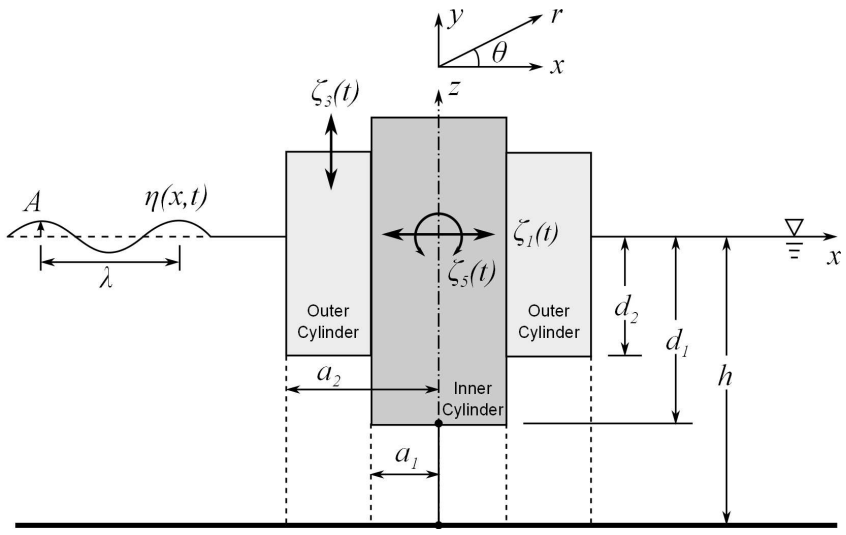

Figure 2.1: Schematic of the dual coaxial-cylinder system.

where $K_{33} = \rho g A_{wp}$ is the hydrostatic coefficient with $\rho,\ g,\ A_{wp}$ being the fluid density, gravitational acceleration, and water-plane area of the floater, respectively. The time-harmonic wave-exciting force in the vertical direction is defined as

$$F_3^{exc}(t) = \Re\{AX_3 e^{-i\sigma t}\} \tag{2.5}$$

where X_3 is the complex amplitude of wave-exciting force per unit wave amplitude. The radiation force in the vertical direction is defined as

$$F_3^{rad}(t) = -\Re\{\mu_{33}\ddot{\zeta}_3(t)\} - \Re\{\lambda_{33}\dot{\zeta}_3(t)\} \tag{2.6}$$

where μ_{33} and λ_{33} are the added mass and inviscid radiation damping coefficients, respectively. The final expression of the heaving motion of the floater defined earlier in Eqn. (2.3) is re-written as

$$(m_2 + \mu_{33})\ddot{\zeta}_3(t) + \lambda_{33}\dot{\zeta}_3(t) + K_{33}\zeta_3(t) = AX_3 e^{-i\sigma t} \tag{2.7}$$

The hydrodynamic quantities, added mass μ_{33}, radiation damping λ_{33}, and wave-exciting force amplitude X_3, can be computed by integrating appropriate potentials over the wetted surface:

$$\mu_{33} + \frac{\lambda_{33}}{-i\sigma} = \rho \int_{S_B} \phi_3 n_3 dS \tag{2.8}$$

$$X_3 = |X_3| e^{i\delta_3} = i\rho\sigma \int_{S_B} [\phi_0 + \phi_7] n_3 dS \tag{2.9}$$

where $\rho,\ \phi_0,\ \phi_3,\ \phi_7,\ n_3,\ S_B$ are the water density, the spatial potential of the incident wave, the radiation in heave, the diffraction potential, the unit normal into the body surface in vertical direction, and the wetted surface, respectively. Here, the fluid flow, described

by the spatial potential $\phi_i,\ i = 0,\ 3,\ 7$ using the linear-wave theory, must satisfy the Laplace equation in the fluid domain as well as the free-surface, seabed, body, and radiation boundary conditions. In order to calculate frequency-dependent hydrodynamic coefficients for the coaxial cylinders, a semi-analytical solution was developed previously by [30] using the method of matching eigenfunction expansions. For given geometric properties, with results of hydrodynamic coefficients from [30], the motion of the floater can be then predicted.

In a real fluid, however, viscous effects are present. To have practical value in predictions, the viscous effects have to be considered. Thus, the total hydrodynamic damping λ_T of the floater is introduced to include the viscous damping λ_{vis} to represent such additional effects:

$$\lambda_T = \lambda_{33} + \lambda_{vis} = f_{vis}\lambda_{33}, \quad \text{with } f_{vis} \equiv \frac{\lambda_T}{\lambda_{33}} \tag{2.10}$$

The heave motion response of the floater relative to the incident-wave amplitude, called response-amplitude operator (RAO), by adding Eqns. (2.1), (2.2), and (2.10) into Eqn. (2.7) is now given by

$$\left|\frac{\mathcal{A}_3}{A}\right| = \frac{|X_3|}{\sqrt{[K_{33} - \sigma^2(m_2 + \mu_{33})]^2 + [\sigma(\lambda_{33} + \lambda_{vis})]^2}} \tag{2.11}$$

It is common to write this in non-dimensional form:

$$\left|\frac{\mathcal{A}_3}{A}\right| = \frac{|\overline{X}_3|}{\sqrt{[\gamma - \overline{\sigma}^2(\overline{m}_2 + \overline{\mu}_{33})]^2 + [\overline{\sigma}^2\overline{\lambda}_T]^2}} \tag{2.12}$$

where

$$\begin{aligned}
\overline{X}_3 &= \frac{X_3}{\pi\rho g a_2^2} \\
\gamma &= 1 - \left(\frac{a_{2,in}}{a_2}\right)^2 \\
\overline{\sigma} &= \sigma\sqrt{\frac{a_2}{g}} \\
\overline{m}_2 &= \frac{m_2}{\pi\rho a_2^3} \\
\overline{\mu}_{33} &= \frac{\mu_{33}}{\pi\rho a_2^3} \\
\overline{\lambda}_T &= \frac{\lambda_T}{\pi\rho\sigma a_2^3}
\end{aligned} \tag{2.13}$$

From the above expression, the floater response can be maximized at the following so-called resonance condition:

$$\overline{\sigma}_{res} = \sqrt{\frac{\gamma}{[\overline{m}_2 + \overline{\mu}_{33}(\overline{\sigma}_{res})]}} \tag{2.14}$$

where an implicit knowledge of the added mass is required.

2.1.2 Modeling of Coupled System with PTO

A fully coupled analysis with the PTO is important to predict the power capture from waves. When the permanent magnet linear generator is attached to the wave-energy converter, an additional external electro-magnetic force $F_g(t)$ will oppose to the direction of the moving translator:

$$F_g(t) = -m_g\ddot{\zeta}_3(t) - B_g\dot{\zeta}_3(t) - K_g\zeta_3(t) \tag{2.15}$$

where $m_g,\ B_g,\ K_g$ are inertia, damping, and spring effects of the generator. From experimental analysis, the inertia and spring values are found to be negligible since they are quite small compared to the mass and spring constant of the floater itself [31]. With the dominant contribution term, the external force by PMLG becomes

$$F_g(t) = -B_g\dot{\zeta}_3(t) \tag{2.16}$$

After adding the generator force into Eqn. (2.7), the RAO expression of the floater coupled with the linear generator is now

$$\left|\frac{\mathcal{A}_3}{A}\right| = \frac{|\overline{X}_3|}{\sqrt{[\gamma - \overline{\sigma}^2(\overline{m}_2 + \overline{\mu}_{33})]^2 + [\overline{\sigma}^2\overline{\lambda}_T(1+\tilde{f})]^2}} \tag{2.17}$$

Here, $\tilde{f}$ is introduced to express the generator damping to the total hydrodynamic damping of the floater:

$$\tilde{f} \equiv \frac{B_g}{\lambda_T} \tag{2.18}$$

2.2 Power Extraction and Energy-Capture Width

The wave-energy converter absorbs the incoming-wave power, and then the PTO converts it into electrical energy. The incident-wave energy flux on the floater per unit width in deep water is given by

$$P_{wave} = \frac{1}{2}\rho g A^2 V_g = \frac{1}{8\pi}\rho g^2 A^2 T \tag{2.19}$$

where V_g is the group velocity. The time-averaged rate of work done $\overline{\dot{W}}$ by the linear generator over one period T, or the mechanical power going into the generator, can be expressed as

$$\begin{aligned}
\overline{\dot{W}} &= \frac{1}{T}\int_{t-T/2}^{t+T/2} B_g\dot{\zeta}_3^2(t)dt \\
&= \frac{1}{T}B_g|\mathcal{A}_3|^2\sigma^2\int_{t-T/2}^{t+T/2}\sin^2\sigma t dt \\
&= \frac{1}{2}B_g|\mathcal{A}_3|^2\sigma^2 \\
&= \frac{\pi}{2}\rho(ga_2)^{\frac{3}{2}}|\mathcal{A}_3|^2\overline{\sigma}^3\tilde{f}\ \overline{\lambda}_T
\end{aligned} \tag{2.20}$$

When combined with the motion response of the floater Eqn. (2.17), the time-averaged mechanical power per wave-amplitude squared A^2 becomes

$$\frac{\overline{\dot{W}}}{A^2} = \frac{\pi}{2}\rho(ga_2)^{\frac{3}{2}}\overline{\sigma}^3\tilde{f}\ \overline{\lambda}_T\left|\frac{\mathcal{A}_3}{A}\right|^2 \tag{2.21}$$

At resonance frequency, it achieves the maximized time-averaged mechanical power:

$$\left.\frac{\overline{\dot{W}}}{A^2}\right|_{res} = \frac{\pi}{2}\rho(ga_2)^{\frac{3}{2}}\frac{|\overline{X}_3|^2}{\overline{\sigma}_{res}\overline{\lambda}_T}\frac{\tilde{f}}{(1+\tilde{f})^2} \tag{2.22}$$

In terms of wave-energy absorption efficiency, a capture width C_w is used, which is the effective width of the wave front from which the energy is extracted. From Eqns. (2.19) and (2.22), the capture width at the resonance is then given by

$$\begin{aligned} C_w = \frac{\overline{\dot{W}}}{P_{wave}} &= \frac{\pi\rho a_2\sqrt{ga_2}}{V_g}\frac{|\overline{X}_3|^2}{\overline{\sigma}_{res}\overline{\lambda}_T}\frac{\tilde{f}}{(1+\tilde{f})^2} \\ &= \frac{2\pi k a_2^2}{\overline{\sigma}_{res}^2}\frac{|\overline{X}_3|^2}{\overline{\lambda}_{33}f_{vis}}\frac{\tilde{f}}{(1+\tilde{f})^2} \\ &= \frac{2ka_2^2}{\overline{\sigma}_{res}^4}\left[\frac{\pi\overline{\sigma}_{res}^2|\overline{X}_3|^2}{\overline{\lambda}_{33}}\right]\frac{1}{f_{vis}}\frac{\tilde{f}}{(1+\tilde{f})^2} \\ &= \frac{1}{k_{res}}\left[\frac{\pi\overline{\sigma}_{res}^2|\overline{X}_3|^2}{2\overline{\lambda}_{33}}\right]\frac{1}{f_{vis}}\eta_{me} \end{aligned} \tag{2.23}$$

where η_{me} is defined as the mechanical efficiency:

$$\eta_{me} = \frac{4\tilde{f}}{(1+\tilde{f})^2} \tag{2.24}$$

In addition, the bracket term represents the Haskind's relation which is reciprocity relationship between the wave-exciting force and the radiation damping. For example, the wave-exciting force for heaving motion is given by [30, 32]

$$\frac{X_3}{\pi\rho g a_2^2} = \left[\frac{2D\overline{\lambda}_{33}}{\pi k a_2}\right]^{1/2} \tag{2.25}$$

where $D = \tanh kh + kh(1-\tanh^2 kh)$.

This capture width expression Eqn. (2.23) allows one to identify several important facts in the absorber design:

1. The mechanical efficiency η_{me} can be maximized by tuning the generator damping B_g to the total hydrodynamic damping λ_T, i.e. $\tilde{f} = 1$ at resonance frequency.

2. If the Haskind's relation for deep water is used, the bracket term becomes unity.

3. If the fluid were inviscid, $f_{vis} = 1$, and the above two items are true, then the well-known inviscid-fluid result is recovered: $k_{res}C_w = 1$, or $C_w = \lambda/2\pi$.

4. In a viscous fluid, the capture width C_w is reduced by the viscous factor of $1/f_{vis}$; the reduction of f_{vis} is seen to be important.

If the floater is not operating at resonance frequency, the generator damping to maximize energy extraction is no longer equal to the total damping of the floater. To find the optimal constant and continuous generator damping at each of the frequencies, Eqn. (2.21) is partially differentiated with respect to the $\tilde{f}$:

$$\begin{aligned}\frac{\partial}{\partial \tilde{f}}\left(\frac{\overline{\dot{W}}}{A^2}\right) =& \frac{\pi}{2}\rho(ga_2)^{\frac{3}{2}}\,\overline{\sigma}^3\,\overline{\lambda}_T|\overline{X}_3|^2\,\frac{\partial}{\partial \tilde{f}}\left\{\frac{\tilde{f}}{[\gamma-\overline{\sigma}^2(\overline{m}_2+\overline{\mu}_{33})]^2+\overline{\sigma}^2\overline{\lambda}_T(1+\tilde{f})]^2}\right\}\\ =& \frac{\pi}{2}\rho(ga_2)^{\frac{3}{2}}\,\overline{\sigma}^3\,\overline{\lambda}_T|\overline{X}_3|^2\,\frac{[\gamma-\overline{\sigma}^2(\overline{m}_2+\overline{\mu}_{33})]^2+\overline{\sigma}^4\overline{\lambda}_T^2(1+\tilde{f})}{\{[\gamma-\overline{\sigma}^2(\overline{m}_2+\overline{\mu}_{33})]^2+\overline{\sigma}^2\overline{\lambda}_T(1+\tilde{f})]^2\}^2}\\ =& 0\end{aligned} \tag{2.26}$$

After re-arranging to create an expression for the $\tilde{f}$ value, it can be expressed as

$$\tilde{f} = \sqrt{1+\mathcal{F}(\sigma)}, \quad \mathcal{F}(\sigma) = \left\{\frac{[\gamma-\overline{\sigma}^2(\overline{m}_2+\overline{\mu}_{33})]}{\overline{\sigma}^2\overline{\lambda}_T}\right\}^2 \tag{2.27}$$

Again, this expression confirms that the value of $\tilde{f}$ should be unity at resonance frequency. When the frequency moves away from resonance, the optimal constant generator damping increases rapidly, see Fig. 2.2.

The above discussion does not take into account the mechanical to electrical energy conversion by PTO, which may not be 100% as the PTO is not perfect. If the energy is dissipated through the applied load resistor of impedance R with a current of intensity $I(t)$ and a voltage drop across the resistor $V(t)$, the time-averaged electrical power output is

$$P_{el} = \frac{1}{T}\int_{t-T/2}^{t+T/2}\frac{V^2(t)}{R}\,dt = \frac{1}{T}\int_{t-T/2}^{t+T/2} RI^2(t)\,dt \tag{2.28}$$

Thus, the useful power output will depend on the mechanical-electrical power conversion efficiency η_{el} of the PTO, that is

$$\eta_{el} = \frac{P_{el}}{\overline{\dot{W}}} \tag{2.29}$$

Finally, the *effective* capture width $C_{w|out}$ at the resonance frequency, including the power conversion efficiency and use of the Haskind's relation, becomes

$$C_{w|out} = \frac{P_{el}}{P_{wave}} = \eta_{el}C_w = \frac{1}{k_{res}}\frac{1}{f_{vis}}\eta_{el}\eta_{me} \tag{2.30}$$

Eqn. (2.30) provides clear directions to increase the effective capture width:

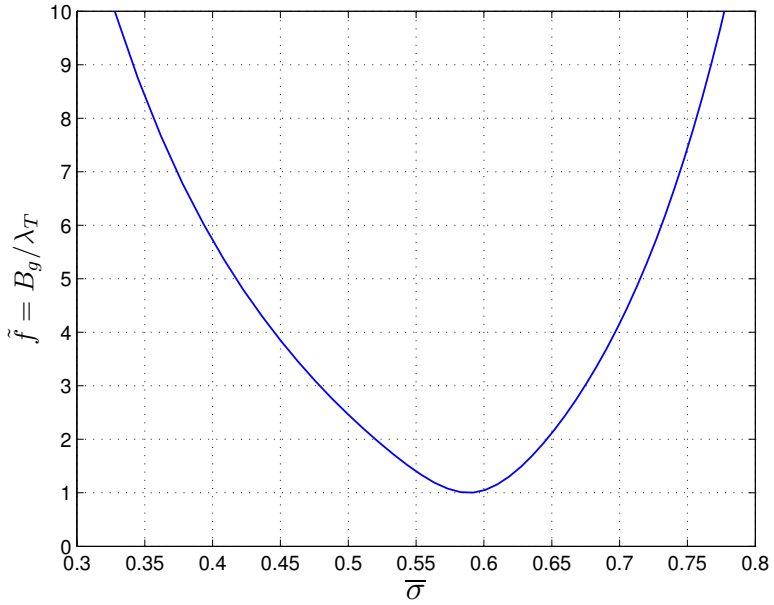

Figure 2.2: Optimal constant and continuous generator damping as a function of frequency

1. Decrease f_{vis} to increase the floater motion response.

2. Match the generator damping B_g to achieve $\eta_{me} = 1$.

3. Increase η_{el} for more electrical power output.

Since the capture width and the effective capture width have a length scale, they are normalized by the diameter of the floater:

$$\overline{C}_w = \frac{C_w}{2a_2}, \quad \overline{C}_{w|out} = \frac{C_{w|out}}{2a_2} \tag{2.31}$$

2.3 Summary Remarks

In this chapter, the linear wave-body interaction model for a oscillating WEC coupled with PMLG unit has been briefly reviewed. Also, the power extraction from wave to wire has been described. This mathematical expression with viscous correction term for the fully coupled system provides performance predictions in terms of the motion response of the floater and wave-energy extraction, which will be used to validate performance in chapter 4. The theoretical analysis permits discussions on the WEC design aspects as well as the operating aspects that can maximize the energy extraction from the incident wave. This findings, Eqn. (2.24) and (2.30), were initially reported in [33].

Chapter 3

Experimental Program

The wave-energy converter studied here mainly consists of the dual coaxial-cylinder and the in-house built permanent-magnet linear generator [29]. The first section of this chapter describes the overall system configurations and instrumentation used for wave-tank measurements. The next section presents properties of the PMLG such as the power-extraction damping value and mechanical to electrical power conversion efficiency. For this purpose, dry-bench tests were carried out by varying the two tuning parameters: magnet-coil gap width and applied or output load resistor.

3.1 Experimental Set-Up

3.1.1 The Dual Cylinders

The coaxial-cylinder system fabricated for testing is shown in Fig. 3.1. The inner cylinder is moored to the bottom of the wave-tank and stabilized by a highly tensioned mooring cable due to the excessive buoyancy, producing about 35 kg of pretension in the mooring line. The stabilized inner cylinder helps the stability of the floating outer cylinder to stay in an upright position. The annular outer cylinder is ballasted by putting weights between the inner and outer shells of the outer cylinder to meet the target resonance frequency. The inner cylinder was fabricated using a cylindrical PVC pipe, with a bottom cap of high-density polyethylene (HDPE). For the annular outer cylinder, the inner shell of a PVC pipe was connected to the outer shell of the outer cylinder which was fabricated using a HDPE water tank.

In this study, a mooring cable is designed to rigidly tether the inner cylinder down. However, when it is too expensive to install a high-stiffness mooring system for deep water, a change in boundary condition of the inner cylinder is needed. The effect of the stiffness of the mooring cable on the performance of the coaxial-cylinder WEC system was analyzed by [34, 35]. The two limiting cases of the free floating inner cylinder and the fixed inner cylinder were considered. It was found that both the freely floating inner cylinder with no mooring cable and the fixed inner cylinder with an infinitely stiff mooring cable are viable. The two limiting cases showed similar performance of the capture width, albeit with very different optimal generator damping. Therefore, the analysis indicates that the forthcoming results with the fixed inner cylinder in heave motion is still reliable, even if a highly tensioned mooring cable is impractical to install. However, an ill-chosen stiffness may eliminate the relative heave motion between the cylinders and lead to no power extraction.

The relative heave motion between the two cylinders is made possible by the use of a pair of heave rods with linear bearings. Also, three tiny rollers were installed on the upper

Table 3.1: Geometric parameters of the model and wave-tank facility (see Fig. 3.6)

Inner cylinder radius	a_1	[m]	0.137
Inner cylinder length	l_1	[m]	1.803
Inner cylinder draft	d_1	[m]	1.067
Outer cylinder inside radius	$a_{2,in}$	[m]	0.151
Outer cylinder outside radius	a_2	[m]	0.254
Outer cylinder length	l_2	[m]	1.067
Outer cylinder draft	d_2	[m]	0.635
Water depth	h	[m]	1.500
Non-dim. target resonance frequency	$\overline{\sigma}_{res}$	-	0.583
Target resonance wave period	T_{res}	[s]	1.735
Wave-tank length	l_T	[m]	68.0
Wave-tank width	w_T	[m]	2.44
Wave-tank depth	h_T	[m]	1.80
Non-dim. the first cut-off frequency	$\overline{\sigma}^1_{wall}$	-	0.808
Non-dim. the second cut-off frequency	$\overline{\sigma}^2_{wall}$	-	1.144
Non-dim. the third cut-off frequency	$\overline{\sigma}^3_{wall}$	-	1.401

and lower ends of the outer cylinder circumferentially to ensure a constant gap between the two cylinders. The cylinders are placed in the middle of the wave-tank to avoid any wall effect. In addition, the floater was designed to have a resonance frequency lower than the first cross-wave cut-off frequency of the wave tank. The interference occurs from the channel wall at cut-off frequencies [36], which is give by

$$\frac{kw_T}{2\pi} = n \tag{3.1}$$

where w_T is the tank width and n is an integer. Detailed geometric parameters of the system and wave-tank facility used in this study are listed in Table 3.1.

3.1.2 The Permanent-Magnet Linear Generator (PMLG) Unit

The translator of the PMLG, consisting of the magnet array, is connected to the outer cylinder through a translator supporter, while the stator of the coils is installed with its

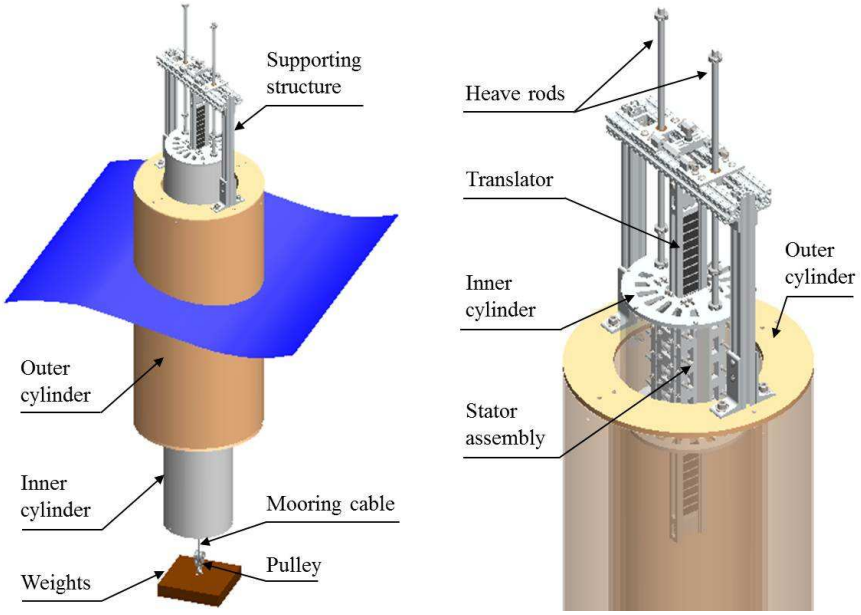

(a) Schematic design of the system

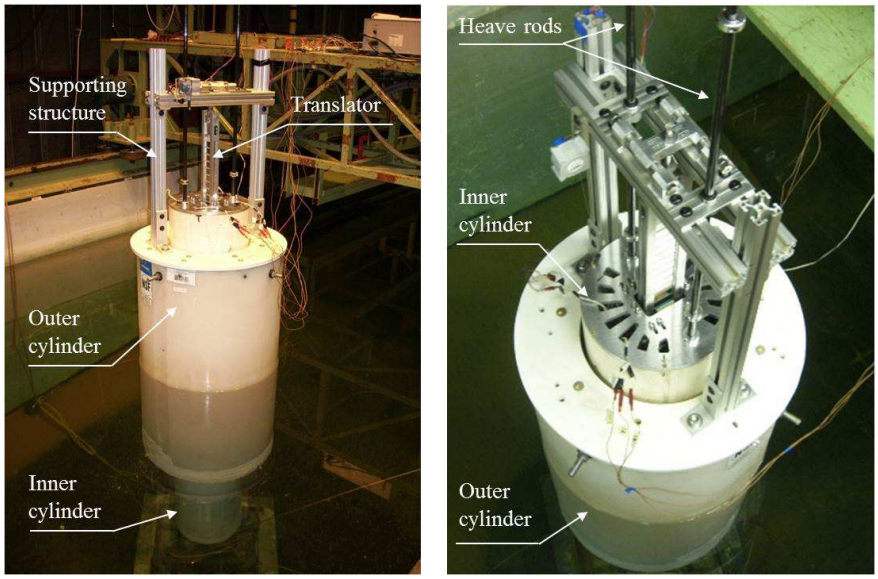

(b) Photographic view of the system

Figure 3.1: Overview of the developed dual coaxial-cylinder system

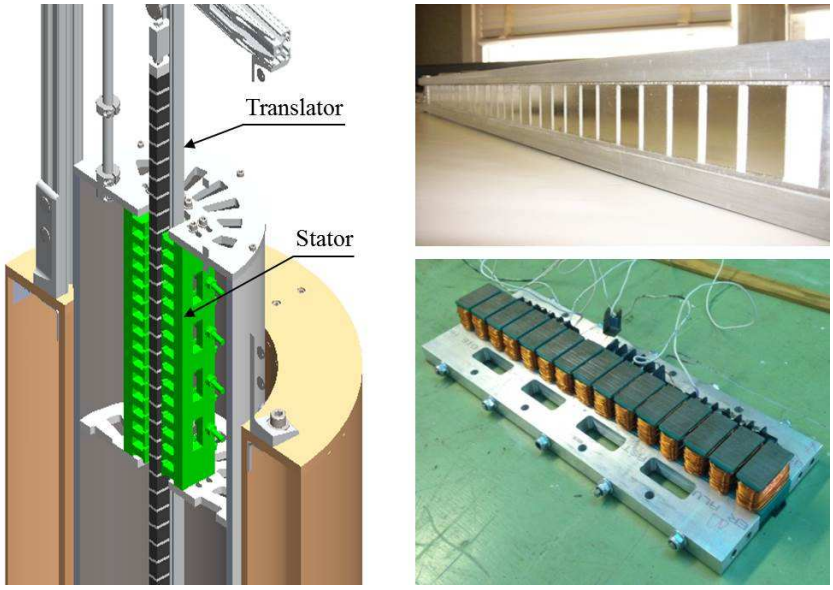

Figure 3.2: The PMLG: cross-section view of the system (left), the translator of magnet array (right top), and the one-sided stator (right bottom)

upper part inside the inner cylinder, illustrated in Fig. 3.2. The translator is 0.762 m long with 34 pairs of magnets placed with alternating polarity. Each magnet measures 1.905 cm $\times$ 5.08 cm $\times$ 0.635 cm, but the thickness was doubled by joining one to the other to increase flux density through the magnet [37]. The stator is composed of two columns of 15 teeth of 0.305 m long, and 5 adjacent teeth become one phase which yields 3 phases on one-side. The detailed PMLG design configuration and analysis are described in [26] and referenced in part here.

The coaxial-cylinder system is designed to be constrained to only pure heave motion, but it does not completely eliminate small undesired relative motion such as surge, pitch, and yaw. These undesired motions cause a high risk of the magnets and coils colliding onto each other because of the strong mutual attraction force between them. The previous design for a single cylinder in [26] had a horseshoe type shape for the stator structure, which resulted in an non-controllable magnet-coil gap width w_{gap} over time, causing a high risk of collision when small undesired motions occurred. Hence, a rigid supporting structure decoupling the heave motion from other motions was needed. A new supporting structure of the translator and the stator assembly was designed and fabricated in order to improve the reliability of and increase the stiffness of the assembly by [37]. Figure 3.3 depicts a supporting structure for the translator [29]. It decouples the heave motion from all other undesired motion by using a horizontal slider and a ball joint that allows three degrees-of-freedom rotation and two translations perpendicular to the vertical direction. A closed-type structure for the stator enables a magnet-coil gap width w_{gap} to be both smaller and more consistent over time, see Fig. 3.4 [29]. The thickness of replaceable cylindrical spacers is directly equal to

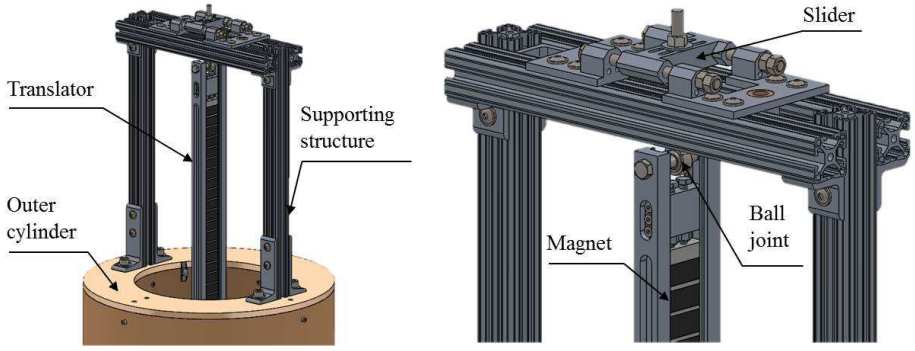

Figure 3.3: Far-view and close-view of translator structure

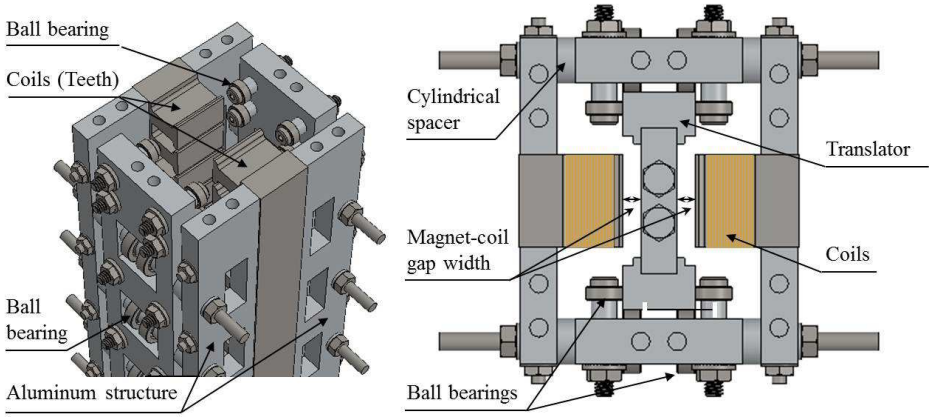

Figure 3.4: Close-view of stator assembly and top-view of stator-translator assembly

the magnet-coil gap width w_{gap}, which makes gap width easier to control.

3.1.3 Measurements

As the translator moves with the outer cylinder due to an incident wave, an electric current is induced in the stator. Each phase of stator is connected to a variable load resistor in which the energy is absorbed or dissipated. The three phases of the output are connected in a wye-winding, and the voltage drop across the load resistor was then measured, which is depicted in Fig. 3.5.

The experiments were conducted at UC Berkeley Richmond Field Station Model Testing Facility, which is a flap-type wave-maker at one end and a beach on the other, see Fig. 3.6. During tests in the wave-tank, the relative displacement between the two cylinders was measured to investigate the motion response of the system. Incident-wave elevation was measured using a capacitive wave gauge, positioned at 10 m ahead of the coaxial-cylinder. Various frequencies of the incident wave were applied during the experiments. To measure

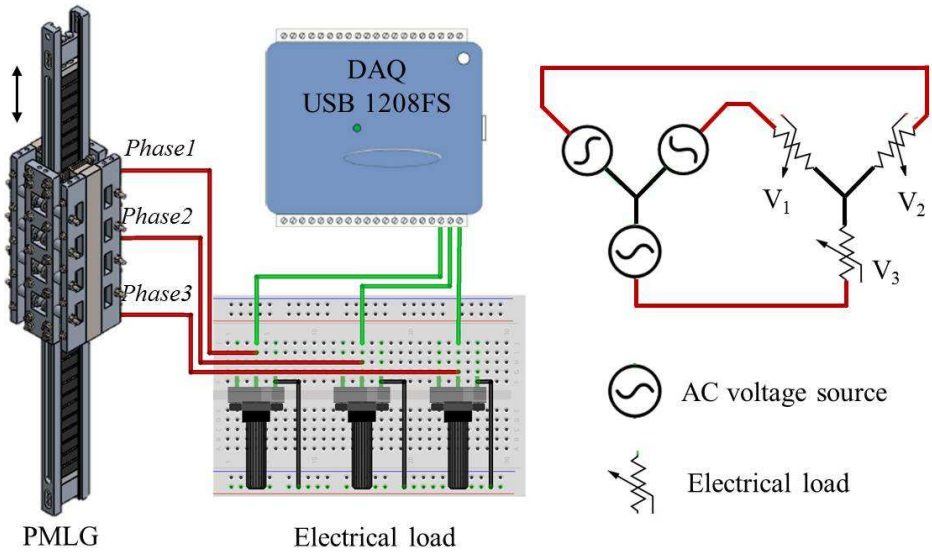

Figure 3.5: Schematic of wye-winding of 3-phase with electrical loads

Table 3.2: Measurement instrumentation

Measurement	Sensor	Model	Specifications
Displacement	String potentiometer	SP1-50, Celesco	0.25% accuracy
Wave elevation	Capacitance wave gauge	Type 201, DHI	<1 mm resolution
	with amplifier	Type 108, DHI	0.1% nonlinearity
Force	Custom strain gauge	-	-
	with amplifier	Model DMA, Interface	0.01% nonlinearity

the wave-exciting force, a strain-gauge force block was used by the outer cylinder being restricted in heave motion.

All data was collected at 200 Hz, with the use of USB-1208FS data acquisition unit from Measurement Computing Corporation. The measurement instruments are shown in Fig. 3.7, which specifications listed in Table 3.2. Each of the sensors was calibrated to get the expected value from the voltage output of sensors.

Figure 3.6: Wave-maker facility at the UC Berkeley Richmond Field Station, referred to in Table 3.1

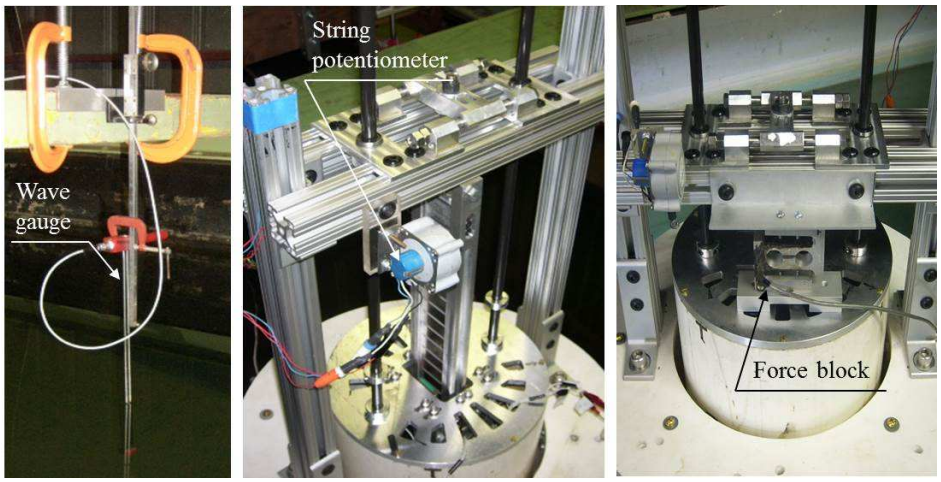

Figure 3.7: Instrumentation: wave gauge (left), string potentiomenter (middle), and z-force block (right)

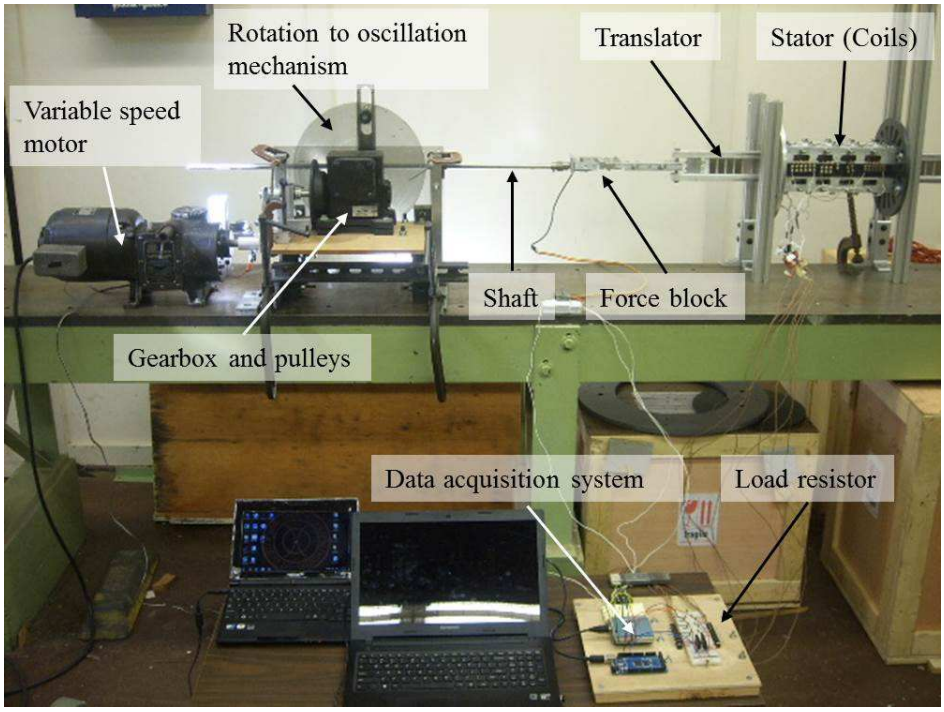

Figure 3.8: Dry-bench test configuration

3.2 Dry-Bench Test of PMLG unit

3.2.1 Bench-Test Apparatus

Before coupling the PMLG unit with the coaxial-cylinder, a dry-bench test was completed to evaluate its properties, i.e. generator damping B_g and power conversion efficiency η_{el}. Figure 3.8 shows the dry-bench test configuration. A variable speed motor drives the translator passing through the stator assembly, and a gearbox with rotating disk between them converts rotation to time-harmonic oscillational motion. Since the strain-gauge force block was installed between the shaft and the translator, the horizontal force required to move the translator was measured. During the experiments, the displacement of the oscillation and the electrical power output dissipated in the applied load resistor were also measured.

Collected displacement $\zeta_3(t)$ and generator force $F_g(t)$ data were processed using Fourier series representation to make a smooth signal, shown in Fig. 3.9:

$$\begin{aligned} \zeta_3(t) &= \alpha_1 \cos\sigma t + \alpha_2 \sin\sigma t \\ F_g(t) &= \beta_1 \cos\sigma t + \beta_2 \sin\sigma t \end{aligned} \tag{3.2}$$

Of note the force data contains noise from the cogging force of the PMLG and undesired test-bed vibrations. Using the reconstructed data, the generator damping coefficient B_g from

the prescribed model of the generator force in Eqn. (2.16) is determined [37]:

$$B_g = \frac{\alpha_1\beta_2 - \alpha_2\beta_1}{\sigma(\alpha_1^2 + \alpha_2^2)} \tag{3.3}$$

Once the PMLG damping value B_g is found, the time-averaged mechanical power is then computed from Eqn. (2.20). The time-averaged electrical power given by Eqn. (2.28) is determined by measuring the voltage drop across the applied load resistor at each phase. Finally, the conversion efficiency of the PMLG η_{el} is obtained by calculating the ratio of the mechanical to electrical power, defined in Eqn. (2.29).

3.2.2 Performance Characterization of the PMLG

In order to model the developed PMLG performance, the electromagnetic equations with a lumped magnet circuit analysis can be used, which provide an analytical solution to predict the magnetic flux available for power conversion and electromagnetic damping as a function of applied load register [38]. However, this study focused on the experimental approach for the performance characterization of the PMLG.

The linear generator damping B_g can be controlled by the connected load resistor R and the magnet-coil gap width w_{gap}. In order to determine the generator damping B_g and power conversion efficiency η_{el}, the load resistance R and the magnet-coil gap width w_{gap} were varied.

In open circuit, the damping $B_{g|\infty}$, corresponding to infinite resistance ($R = \infty$), which only depends on magnet-coil gap width w_{gap}, was obtained. It includes the residual electromagnetic damping related to cogging, eddy current losses, and bearing friction etc. Figure 3.10 represents measured $B_{g|\infty}$ at the resonance frequency, and an appropriate empirical fitting form was chosen as

$$B_{g|\infty}(w_{gap}) = \alpha + \frac{\beta}{(w_{gap}/\gamma)^n} \tag{3.4}$$

where α=4.74 N/(m/s), β=0.65 N/(m/s), γ=1.52 cm, and n=2.11.

By subtracting $B_{g|\infty}$ from the measured generator damping B_g of the closed circuit, the generator damping contributed by electromagnetic forces can be deduced. Each series of experimental values of $B_g - B_{g|\infty}$ as a function of w_{gap} is very well fitted by an exponential function for different R value, as shown in Fig. 3.11. With the re-designed PMLG assembly, a very small gap can be reachable even when a very higher value of the generator damping B_g is required. The exponential fitting curves follow the form of

$$B_g(R, w_{gap}) - B_{g|\infty}(w_{gap}) = A(R)e^{-B(R)\cdot w_{gap}} \tag{3.5}$$

with

$$\begin{aligned} A(R) &= 47.02 + \frac{27747.03}{(R + 5.19)^{1.69}} \text{ N/(m/s)}, \quad (R \text{ in ohms}) \\ B(R) &= -0.0005R^2 - 0.02R + 3.18 \text{ cm}^{-1}, \quad (R \text{ in ohms}) \end{aligned} \tag{3.6}$$

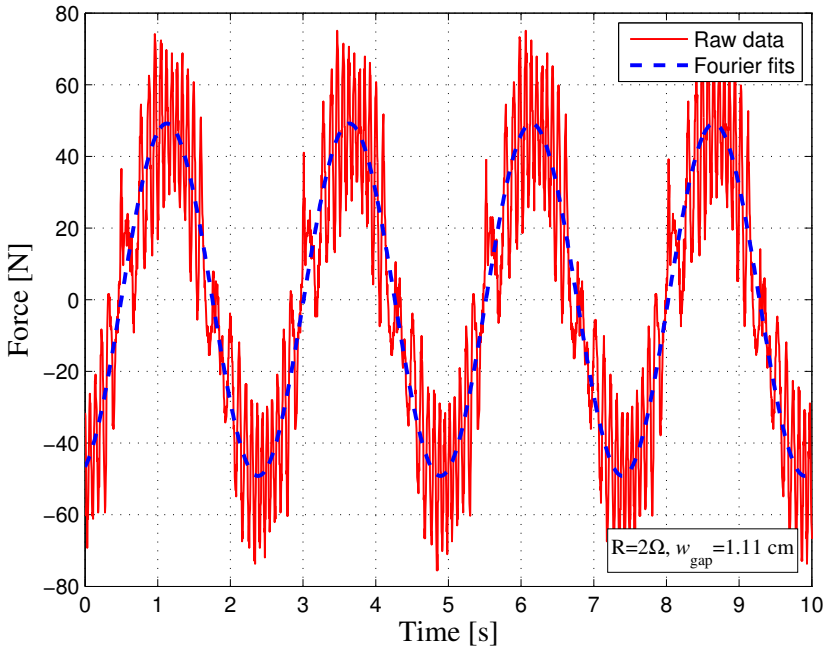

(a) Force measurements

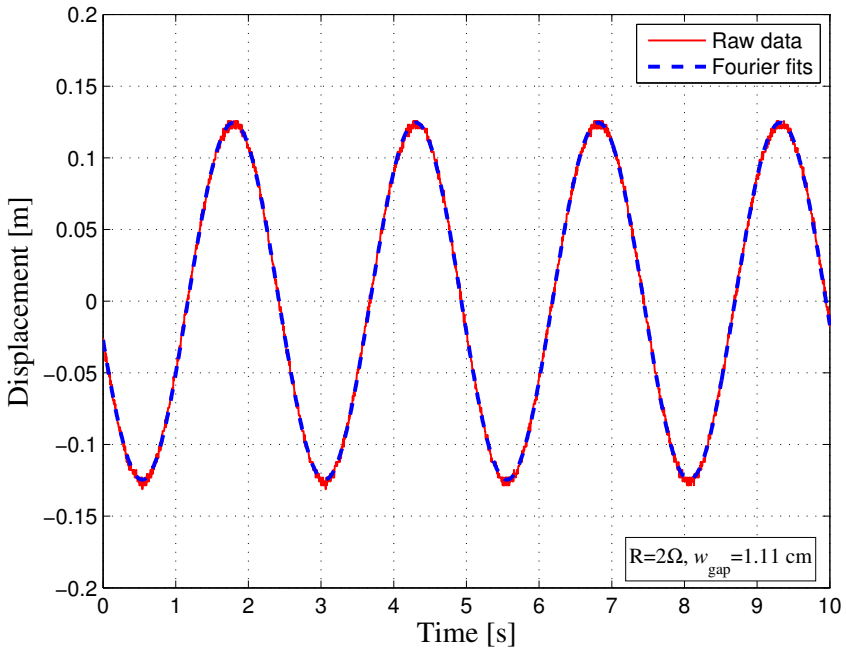

(b) Displacement measurements

Figure 3.9: Measured and reconstructed data by fourier fitting data from bench test

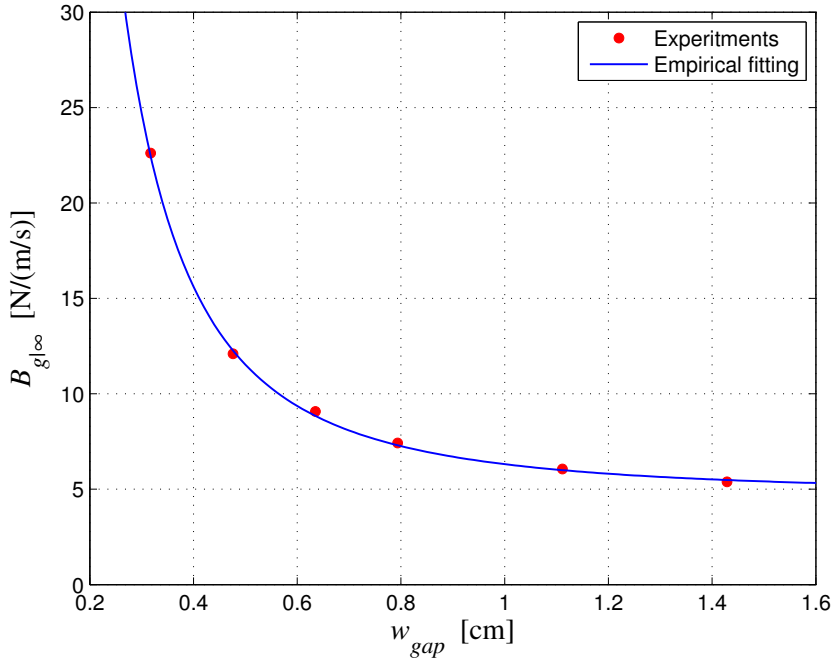

Figure 3.10: Generator damping at infinite resistance, with empirical fitting

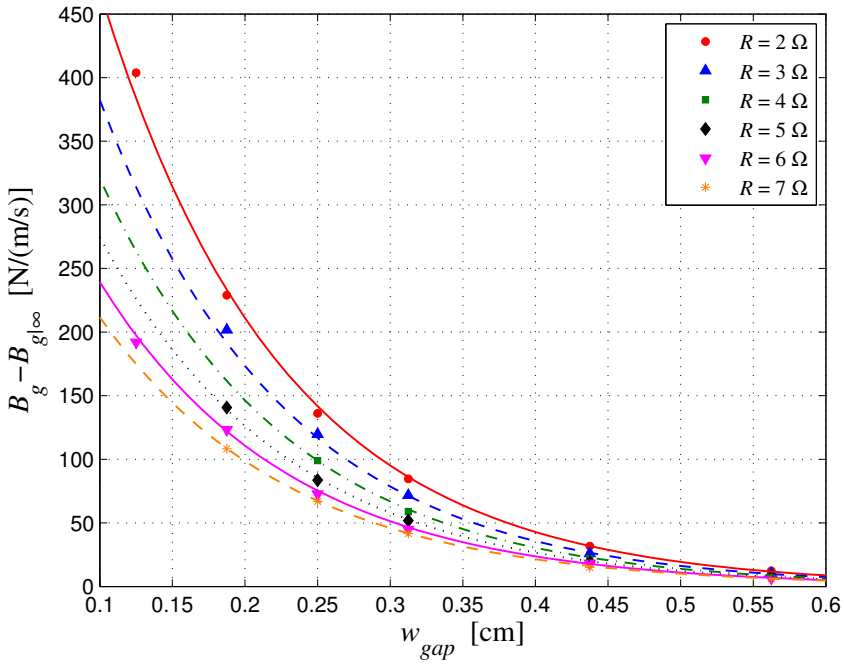

Figure 3.11: Generator damping due to electromagnetic force, with empirical fitting

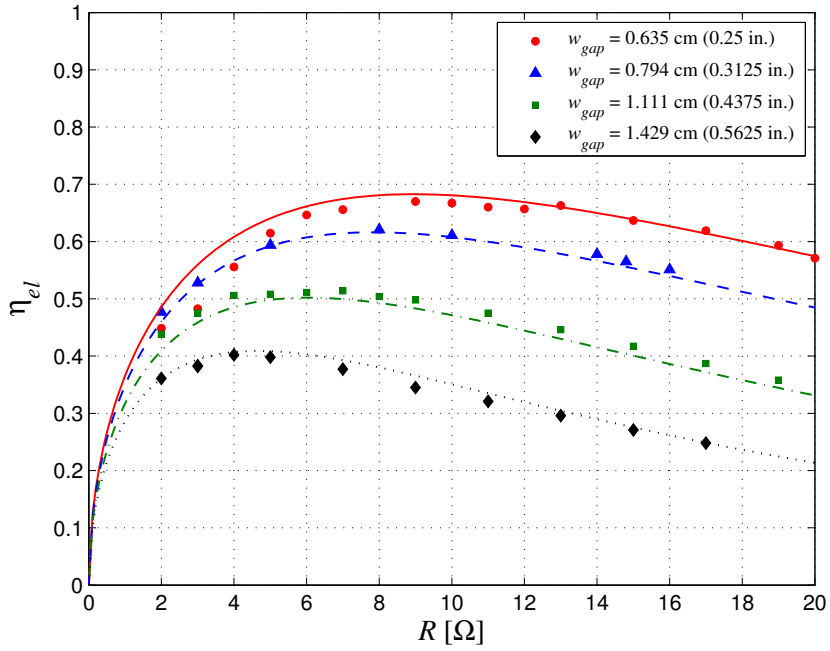

Figure 3.12: Mechanical to electrical conversion efficiency of the PMLG, with empirical fits

An empirical form for the total generator damping $B_g(R, w_{gap})$ is then obtained from the above two fits:

$$B_g(R, w_{gap}) = A(R)e^{-B(R)\cdot w_{gap}} + \left[\alpha + \frac{\beta}{(w_{gap}/\gamma)^n}\right] \tag{3.7}$$

The conversion efficiency of the PMLG is found in Fig. 3.12, where experimental results from the dry-bench test and the wave-tank test were drawn together. It is clear that for each value of w_{gap}, there is a specific value of resistance R that maximizes the electrical conversion efficiency. For mechanical to electrical conversion efficiency $\eta_{el}(R, w_{gap})$, a possible empirical formula is

$$\eta_{el}(R, w_{gap}) = \frac{A(w_{gap}) \cdot R^n}{[R + C(w_{gap})]^m} \tag{3.8}$$

with

$$\begin{aligned} A(w_{gap}) &= (1.03e^{-0.65w_{gap}})(15.05e^{-0.82w_{gap}})^{(m-n)}\left(\frac{m}{n}\right)^m, \quad (w_{gap} \text{ in cm}) \\ C(w_{gap}) &= \left(\frac{m-n}{n}\right)15.05e^{-0.82w_{gap}}, \quad (w_{gap} \text{ in cm}) \\ n &= 0.5 \\ m &= 4.0 \end{aligned} \tag{3.9}$$

3.3 Summary Remarks

A self-contained WEC consisting of two coaxial cylinders has been developed. A direct-drive energy conversion system using the PMLG has been used to extract the wave-energy from the relative heave motion between the two bodies. The PMLG unit has been customized for the floating system.

This chapter has also presented characteristics of the PMLG from the dry-bench tests. As a result, the PMLG damping coefficient and the power-conversion efficiency are experimentally determined as functions of two parameters: the applied load resistance and magnet-coil gap width. These results can provide some guidelines to select the best operating settings of (R, w_{gap}) when the useful electrical power output is considered.

Chapter 4

Performance Optimization and Validation

The mathematical modeling in chapter 2 provided potential directions to increase the energy capture. The dry-bench tests of chapter 3 characterized the PMLG for power extraction. Approaches to optimize the performance of the WEC system [29] are covered in the first section of this chapter. One concept involves bottom-shape modification of the floater and determination of the optimal operating conditions. Next, the experiments of the developed physical system in lab-scale are carried out to validate the theoretical prediction in regular waves. It includes wave-exciting force, free-motion response without the PMLG, and performance of the fully coupled system. Therefore, this chapter examines and compares the performances of the coaxial-cylinder WEC system for both different bottom shapes with theoretical predictions.

4.1 Optimizing the Performance of the System

4.1.1 Modification of the Bottom Shape of Floater

For energy extraction, as discussed in Eqns. (2.23) and (2.30), the performance of the WEC is always degraded by viscosity effects. Therefore, one way to enhance the performance is to reduce the viscosity effects. In particular, the shape of the floater plays an important role in determining hydrodynamic coefficients, especially damping, which is strongly related to the body motion [39]. The flat-bottom (FB) shape of the floater causes significant separation losses in the fluid and its energy cannot be recovered. To reduce viscosity effects, a special geometry of a highly asymmetrical, needle-like curved surface for one side and a flat for the other side, following The Berkeley Wedge (TBW) [40] is imported. This patented design was found to have minimal viscous effects. Figure 4.1 shows the Berkeley Wedge design as a shape smoother at the bottom of the floater. To fabricate the BW-shaped bottom, 38 ABS plastic sheets of 0.25 in thickness, with the same inner radius and different outer radius following the BW profile, were layered. The stepped surface of the multi-layered BW bottom was redeemed by water putty, and then coated with epoxy resin for hardening and waterproofing, see Fig. 4.2. It was then connected to the bottom of the floater using bolts. The draft of the modified floater was adjusted to produce the same resonance frequency as that for the FB floater. The dimensions of the Berkeley Wedge and new draft are listed in Table 4.1.

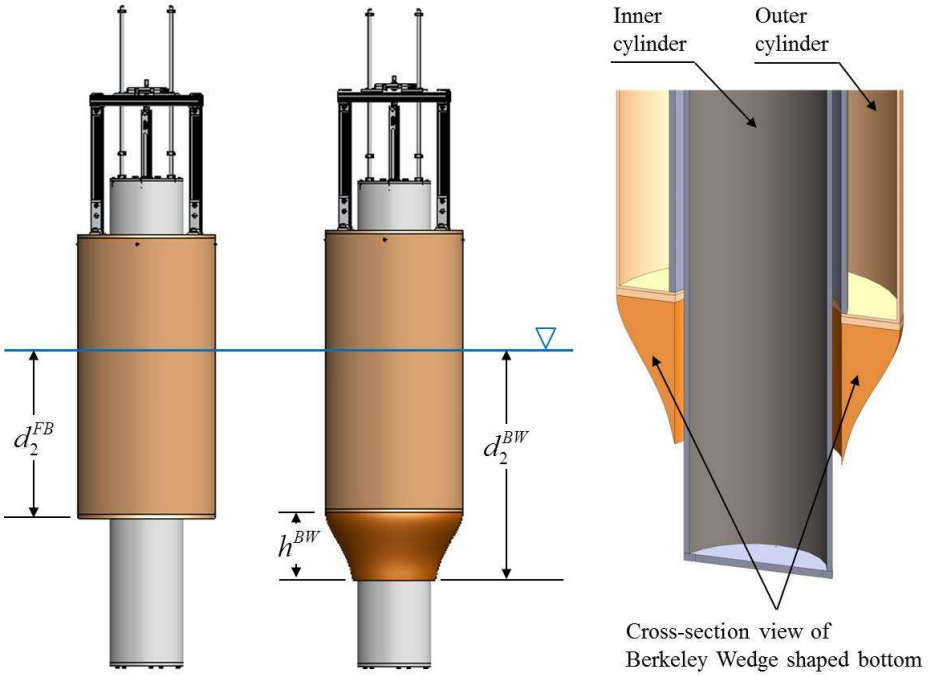

Figure 4.1: Flat and the Berkeley-Wedge bottom shape of the floater

Figure 4.2: Fabrication of the Berkeley-Wedge bottom shape of the floater and close-view of bottom installed in wave-tank (right)

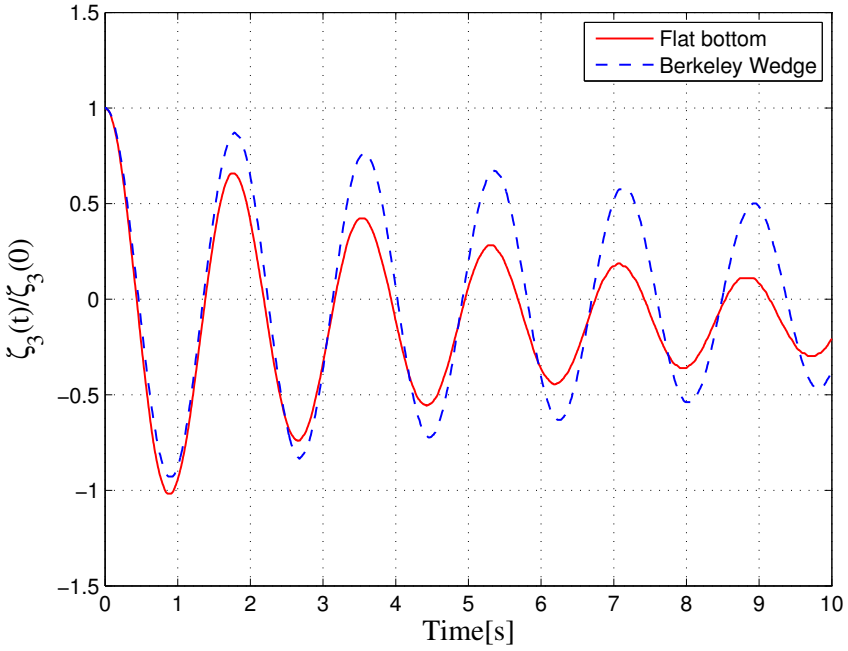

Figure 4.3: Time history of the heave oscillation from free-decay tests

4.1.2 Determination of Viscous Effects from Free-Decay Tests

The viscous effects must be known in order to predict the WEC performance precisely. Moreover, since the reduction of viscous effects is expected with the BW-shaped bottom of the floater, free-decay tests were completed without a linear generator. To do this, the outer cylinder is released from a certain initial position. The recorded oscillation motion in time series shows a typical underdamped mechanical system because the motion of the floater gradually decreases to its steady-state position, which is shown in Fig. 4.3. This result gives the resonance period of the floater and experimentally determined hydrodynamic coefficients, such as added mass and damping, including viscous effects using the logarithmic-decrement method.

Table 4.1: Draft adjustment and dimensions of Berkeley-Wedge bottom shape

Outer cylinder draft, Flat Bottom	d_2^{FB}	[m]	0.635
Outer cylinder draft, Berkeley Wedge	d_2^{BW}	[m]	0.845
Berkeley Wedge shape height	h^{BW}	[m]	0.235
Berkeley Wedge shape weight		[Kg]	15.65

From the successive maximum or minimum peaks $\zeta_{3,p}$ and $\zeta_{3,p+1}$ with times T_p and T_{p+1}, the damped natural frequency σ_d and the logarithmic decrement δ are calculated:

$$\sigma_d = \frac{2\pi}{T_{p+1} - T_p} = \frac{2\pi}{T_d} \tag{4.1}$$

$$\delta = \ln\left(\frac{\zeta_{3,p}}{\zeta_{3,p+1}}\right) = \xi\sigma_n T_d = \xi\sigma_n \frac{2\pi}{\sigma_d} = \xi\sigma_n \frac{2\pi}{\sigma_n\sqrt{1-\xi^2}} = \frac{2\pi\xi}{\sqrt{1-\xi^2}} \tag{4.2}$$

where σ_n is the undamped natural frequency of the system defined as Eqn. (2.14), and ξ is the damping ratio given by

$$\xi = \frac{\lambda_T}{2(m_2 + \mu_{33})\sigma_n} = \frac{\delta}{\sqrt{4\pi^2 + \delta^2}} \tag{4.3}$$

The oscillation displacement in time series directly provide the resonance time period T_d and the logarithmic decrement δ. In calculation, the first 2 or 3 peaks are used since error from bearing friction is accumulated as motion decreases with time. From the definition of the undamped resonance frequency in Eqn. (2.14), the added mass μ_{33} is experimentally found. Finally, Eqn. (4.3) determines the viscous effect on damping at resonance frequency by subtracting the analytical radiation damping for the inviscid fluid: $\lambda_{vis} = \lambda_T - \lambda_{33}$.

As a result, the correction factors to better predict the performance on the damping f_{vis} and the added mass q are determined for the different bottom shapes. The correction factors were integrated into the analytical solutions that were derived only for the flat bottom by [30], see Table 4.2. Indeed, the viscous damping is significant, as expected, about 7.5 times higher than wave damping for the flat bottom. Due to the bottom shape modification, the total damping of the floater is significantly reduced by 67%.

4.1.3 Optimal Operating Conditions

The generator damping highly affects the power extraction and the overall system behavior. Thus, an appropriate generator damping must be chosen to increase the instantaneous power output. According to the previous discussion, the combination of (R, w_{gap}) of the linear generator must be selected to create the required damping value B_g. It is desired to achieve $\tilde{f} = 1$ to maximize the defined mechanical efficiency η_{me} from Eqn. (2.23). From

Table 4.2: Non-dimensional hydrodynamic coefficients and determined correction factors at resonance frequency

	$\overline{\lambda}_{33}$	$\overline{\lambda}_T$	$\tilde{f}_{vis} = \overline{\lambda}_T/\overline{\lambda}_{33}$	$\overline{\mu}_{33}$	$\overline{\lambda}_{exp}$	$q = \overline{\mu}_{33,exp}/\overline{\mu}_{33}$
FB	0.029	0.245	8.448	0.254	0.347	1.366
BW	-	0.080	2.753	-	0.147	0.578

the experimentally obtained total damping λ_T at the resonance frequency and the empirical expression of Eqn. 3.7, the non-dimensional generator damping factor $\tilde{f} = B_g/\lambda_T$ can be calculated. Figure 4.4 represents the contour map of $\tilde{f}$ for both the FB and BW-shaped floaters. It can be seen that a wide range of damping values is reachable by choosing a combination of (R, w_{gap}). In the case of the BW, $\tilde{f}$ is obviously much higher than in the case of the FB for the same (R, w_{gap}) because of the significant reduction of the total damping λ_T. As defined in Eqn. (2.24), the mechanical efficiency η_{me} is plotted in Fig. 4.5. It has the same iso-curve as that of $\tilde{f}$.

Even though it is obvious that the capture width C_w is maximized at exactly $\tilde{f} = 1$, it does not guarantee the maximized electrical power output, or effective capture width $C_{w|out}$, because of the conversion efficiency η_{el} of the PTO. The maximum effective capture width $C_{w|out}$ is equivalent to the maximum of the product $\eta_{me}\eta_{el}$ from Eqn. (2.30), not just η_{me}. This signifies that it is not necessary to maximize $\tilde{f}$ to 1. From the empirically determined electrical conversion efficiency η_{el} in Eqn. 3.8, iso-curves are plotted in Fig. 4.6. And then, results of product $\eta_{me}\eta_{el}$ are shown in Fig. 4.7. From this contour plot, the optimal operating point of (R, w_{gap}), which results in the highest effective capture width $C_{w|out}$, can be determined.

Hence, the optimal operating conditions for both different bottom shapes are as follows:

- Flat bottom (FB): $(R, w_{gap}) = (11.0\ \Omega, 0.635\ \text{cm})$, corresponding to $\tilde{f} = 1.58$
- Berkeley Wedge (BW): $(R, w_{gap}) = (9.0\ \Omega, 1.11\ \text{cm})$, corresponding to $\tilde{f} = 1.80$

Even though B_g does not exactly match λ_T, i.e. $\tilde{f} = 1$, the mechanical efficiency η_{me} does not drop dramatically near $\tilde{f} = 1$, which is seen in Fig. 4.8, while the difference in electrical conversion efficiency η_{el} is sufficiently large so that the product of the two efficiencies is higher than when $\tilde{f} = 1$.

4.2 Experimental Results and Validation

4.2.1 Heave Wave-Exciting Forces

The measured non-dimensional wave-exciting force amplitude $|\overline{X}_3|$ of the outer cylinder relative to the incident wave is presented with the theoretical predictions obtained from [30] as a function of non-dimensional frequency (Fig. 4.9). Note that the theoretical prediction is for the flat-bottom floater. Remarkably, these measurements show that there is no significant difference between the two different bottom shapes over the frequency range shown. A comparison with the theoretical predictions establishes that the Haskind's relation is valid even in viscous fluid, and can be applied to both cases.

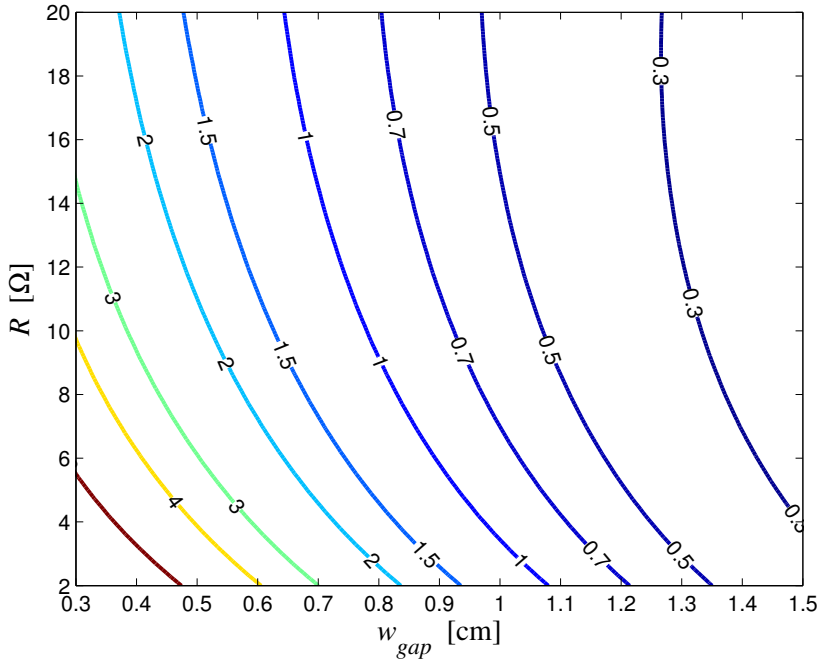

(a) Flat bottom

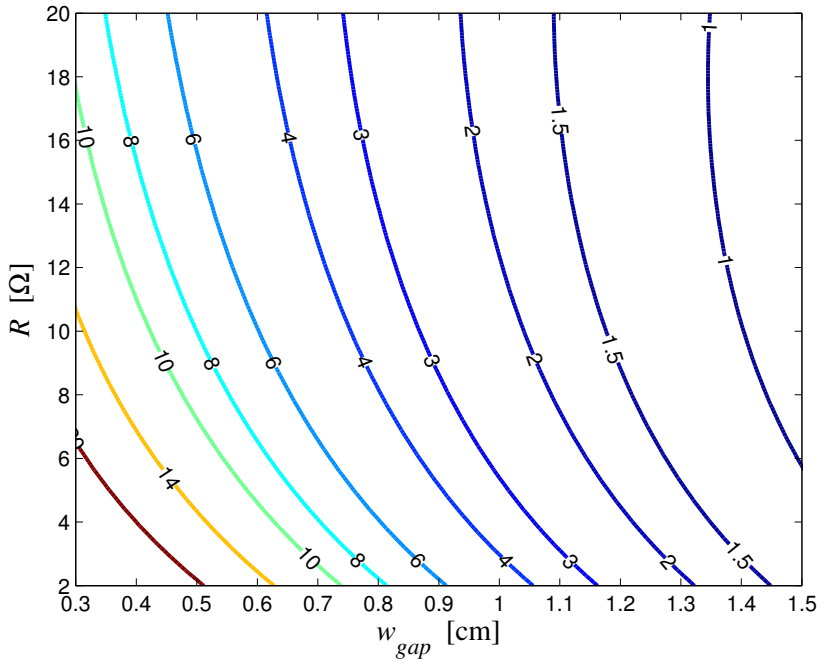

(b) Berkeley Wedge

Figure 4.4: Contour plot of $\tilde{f}$ from empirical expression of B_g

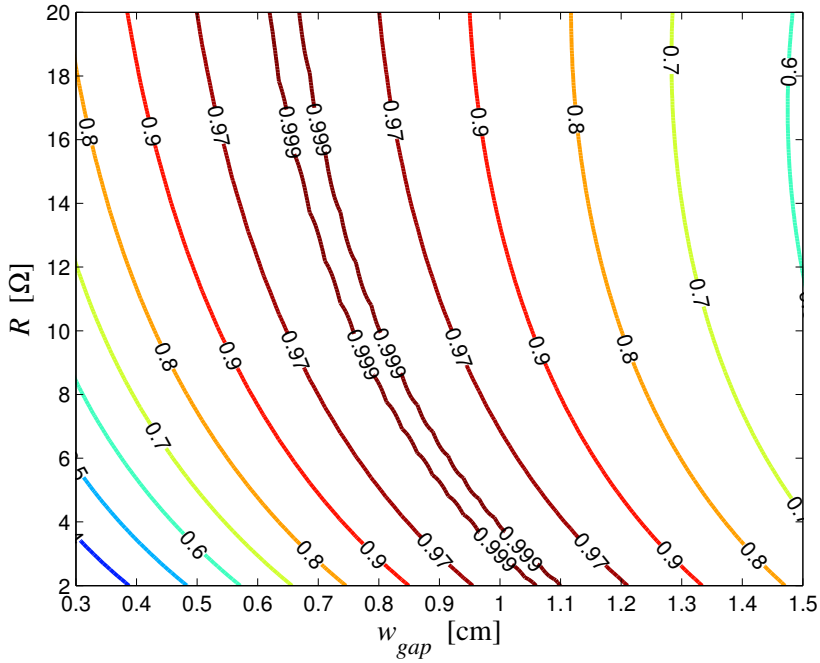

(a) Flat bottom

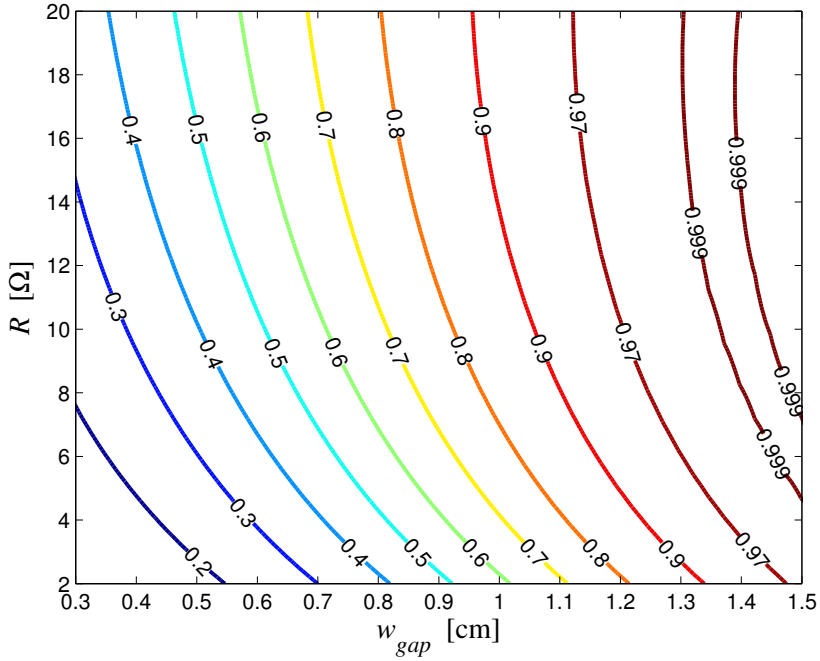

(b) Berkeley Wedge

Figure 4.5: Contour plot of η_{me} from empirical expression of B_g

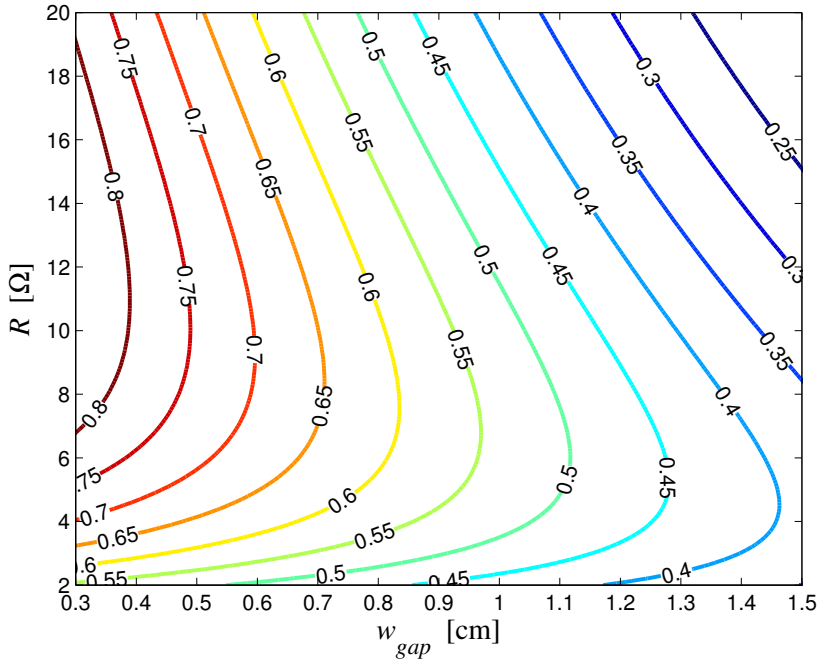

Figure 4.6: Contour plot of η_{el} from empirical expression of B_g

4.2.2 Free-Motion Response

The relative heave motion response between the two cylinders to the incident-wave amplitude can be predicted from Eqn. (2.12) with use of hydrodynamic properties and viscous corrections. The frequency-dependent added mass, radiation damping, and wave-exciting force with phase angle are shown in Fig. 4.10. These values were obtained by [30] for given geometric properties, see Table 3.1.

The floater motion response for the flat-bottom shape without the PMLG, i.e. $B_g = 0$, is shown in Fig. 4.11. The prediction of heave motion with viscosity factor on damping f_{vis} follows the general trend of experimental results, but the peak value is slightly off from the measurements. The experimental non-dimensional resonance frequency $\overline{\sigma}$ is around 0.567 (1.78 sec), whereas the target non-dimensional resonance frequency is 0.583 (1.735 sec). The viscous effect q on the theoretical added mass shifts the predicted RAO curve to the left, and a better agreement with experimental results is observed. It is also observed that the RAO reaches unity in the low frequency limit and zero in high frequency.

Figure 4.12 presents the heave amplitude in response to the incident wave for both types of bottom shapes with $B_g = 0$. In order to better predict the performance, the correction factors on the damping f_{vis} and on the added mass q experimentally determined at resonance frequency are integrated into the analytical solutions that were derived for the flat bottom. Predictions from the theoretical results agree well with the measurements for both different

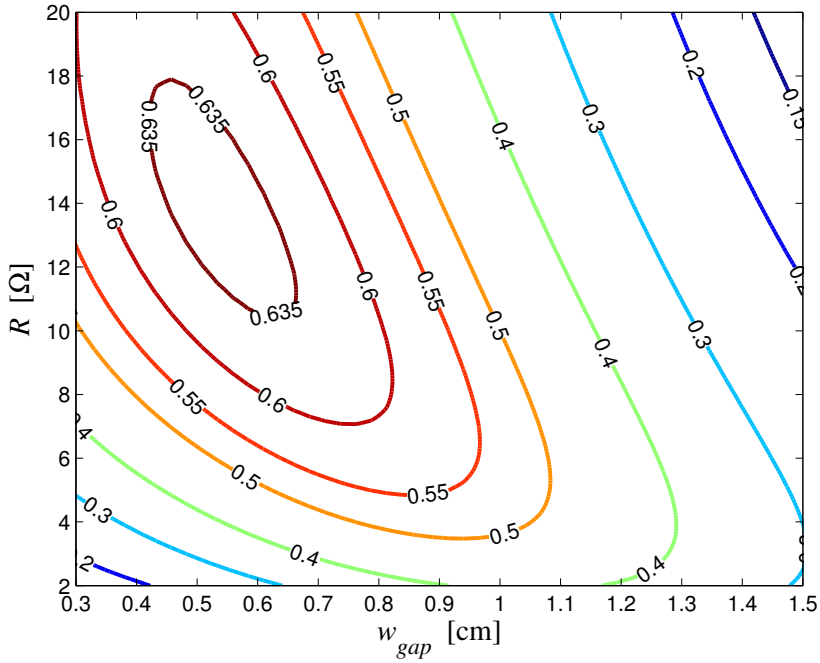

(a) Flat bottom

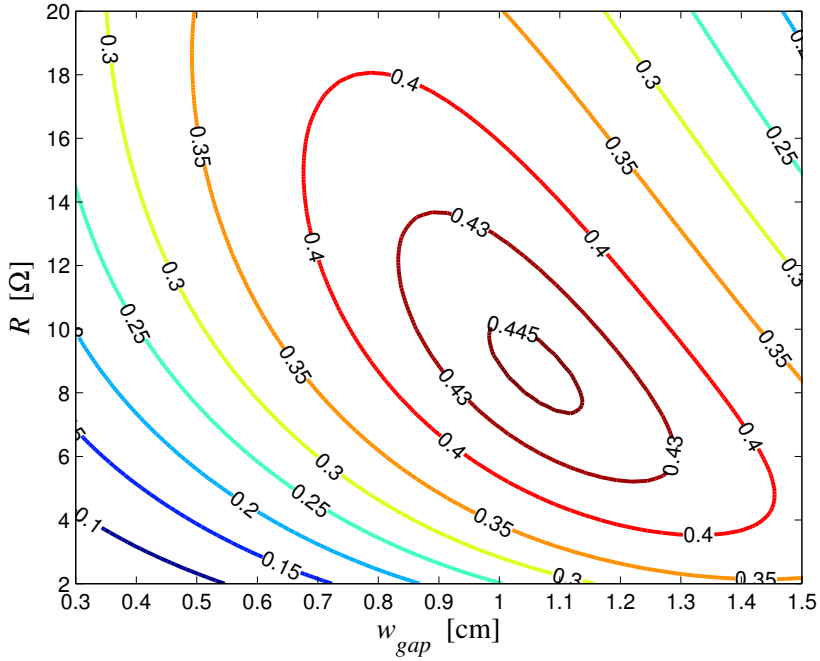

(b) Berkeley Wedge

Figure 4.7: Contour plot of $\eta_{me}\eta_{el}$ from empirical expression of B_g

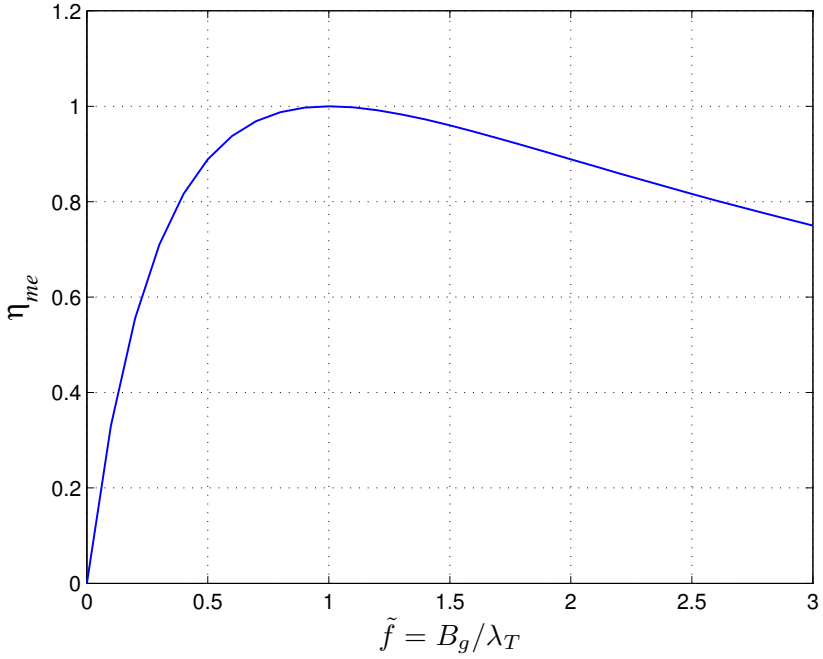

Figure 4.8: Contour plot of η_{el} from empirical expression of B_g

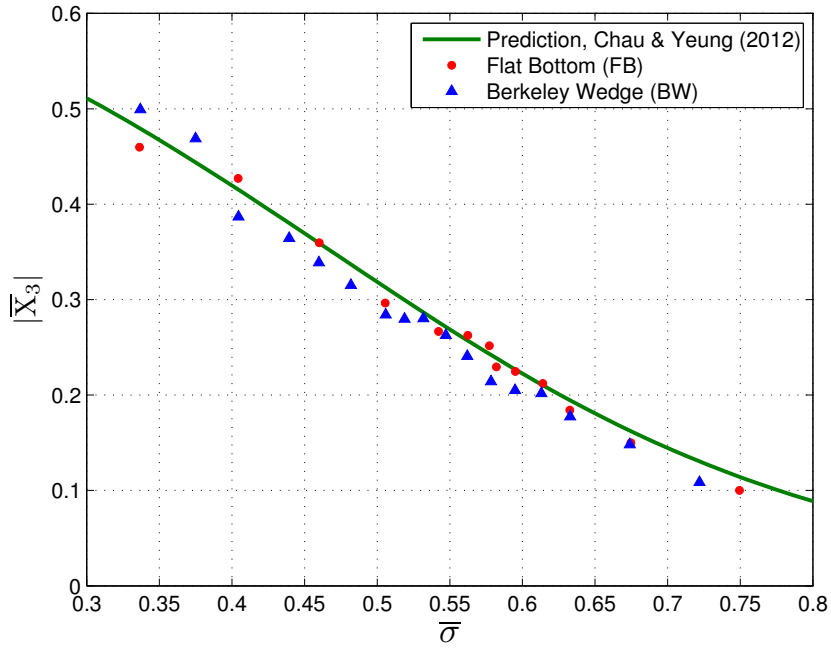

Figure 4.9: Predicted (curve) and measured (symbols) non-dimensional wave-exciting force

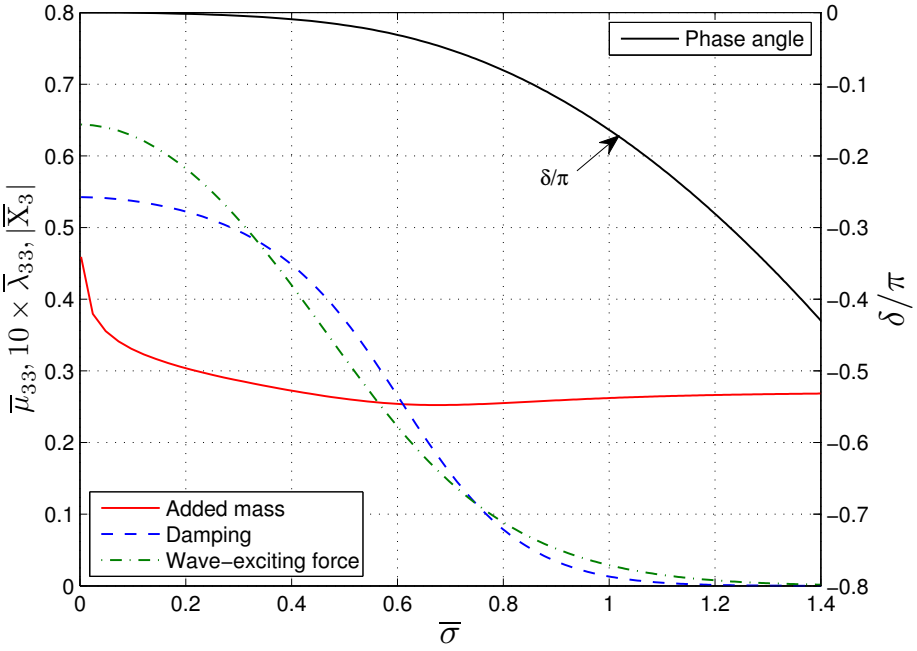

Figure 4.10: Non-dimensional hydrodynamic coefficients from [27] for the flat bottom

bottom shapes. The BW bottom led to a 3 times increase in motion response, as a result of the reduction of viscous damping f_{vis}.

4.2.3 Performance Assessment of the Fully Coupled System

Performance of the fully coupled coaxial-cylinder with the PMLG for both the flat bottom (FB) and the Berkeley Wedge (BW) shapes is measured with different generator damping values of $\tilde{f} = B_g/\lambda_T$. To have different damping values, different operating conditions of (R, w_{gap}) were selected with the optimal operating conditions calculated in the previous section, listed in Table 4.3.

Measured heave RAO for the different bottom shapes are shown in Fig. 4.13. The RAO increases for both shapes with decreasing $\tilde{f}$, or decreasing the generator damping B_g, as can be expected. Furthermore, the theoretical predictions with corrections of f_{vis} and q are well matched by the experimental measurements. In terms of the bottom shape optimization of the floater, the BW shape led to a 3 times increase in amplitude for the same value of $\tilde{f}$, due to the much lower viscous damping while the bandwidth becomes more narrow.

Figure 4.14 presents the non-dimensional capture width $\overline{C}_w$ as a function of non-dimensional frequency as well as the heave RAO. The measurements also match quite well with the predictions. The RAO and capture width peak out simultaneously at the resonance frequency. It is also observed that the capture width is maximized for $\tilde{f} = 1$, which is expected from

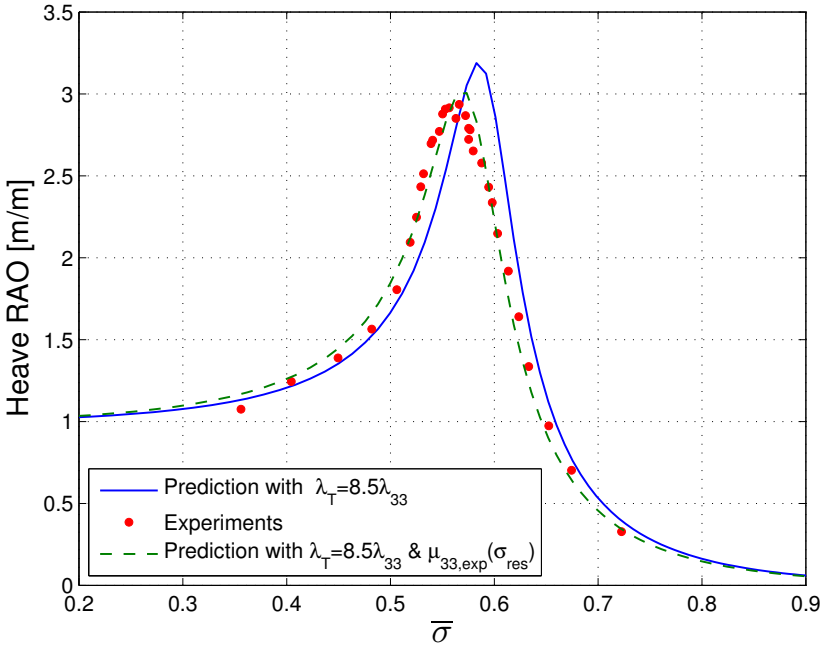

Figure 4.11: Measured free motion response and prediction with correction factors for flat bottom shape floater

Table 4.3: Operating condition of PMLG for experiments

	R [Ω]	w_{gap} [cm]	$\tilde{f}$
FB	4.0	1.150	0.26
	7.5	0.889	1.04
	11.0	0.635	1.58
	7.0	0.635	2.15
	2.1	0.635	4.16
BW	9.0	1.429	0.98
	9.0	1.111	1.80
	17.0	0.635	4.08
	9.0	0.635	5.88

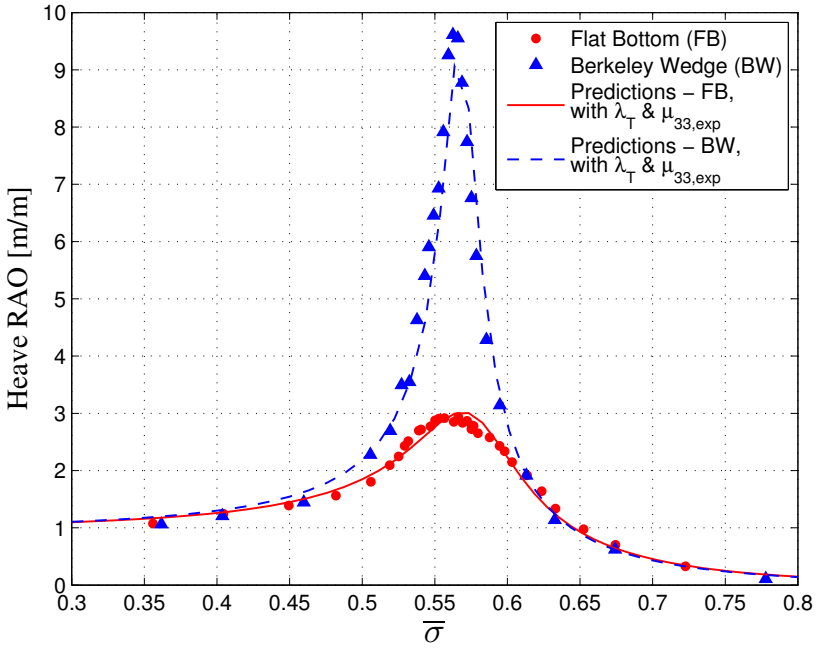

Figure 4.12: Predicted and measured free motion response of the floater

the earlier discussion. Similarly to the heave RAO results, the peak value of the absorbed energy is increased by about 3 times because of the BW shape.

The non-dimensional effective capture width $\overline{C}_{w|out}$, which accounts for the electrical conversion efficiency η_{el} from the capture width results, is plotted in Fig. 4.15. It is demonstrated that the optimal operating point determined from $\eta_{me}\eta_{el}$ in the previous section led to the maximum effective capture width, or maximum electrical power output. Furthermore, the maximum of $\overline{C}_{w|out}$ at resonance frequency increased by a factor of 2 because of the change in the bottom shape. As the damping factor $\tilde{f}$ increases towards the optimal value for both cases, peak value and bandwidth increase. Once the $\tilde{f}$ increases over the optimal damping value, the peak decreases while the bandwidth continues to increase [34]. Numerical details on the performance optimization measured at resonance frequency are listed in Table 4.4.

4.3 Summary Remarks

Improvements have been made to enhance the performance of the wave-energy extraction. The geometrical modification of the floater's bottom and the selection of the optimal generator damping value, which are based on the interpretation of the mathematical expression describing the power extraction by the WEC, were implemented.

Effects of the modified bottom shape, adopted from the Berkeley Wedge design, on the

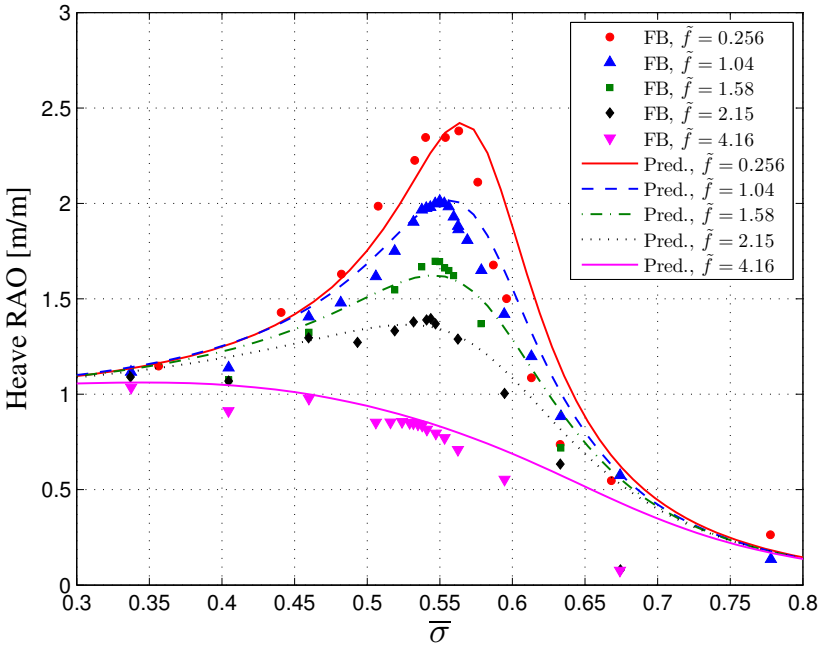

(a) Flat bottom

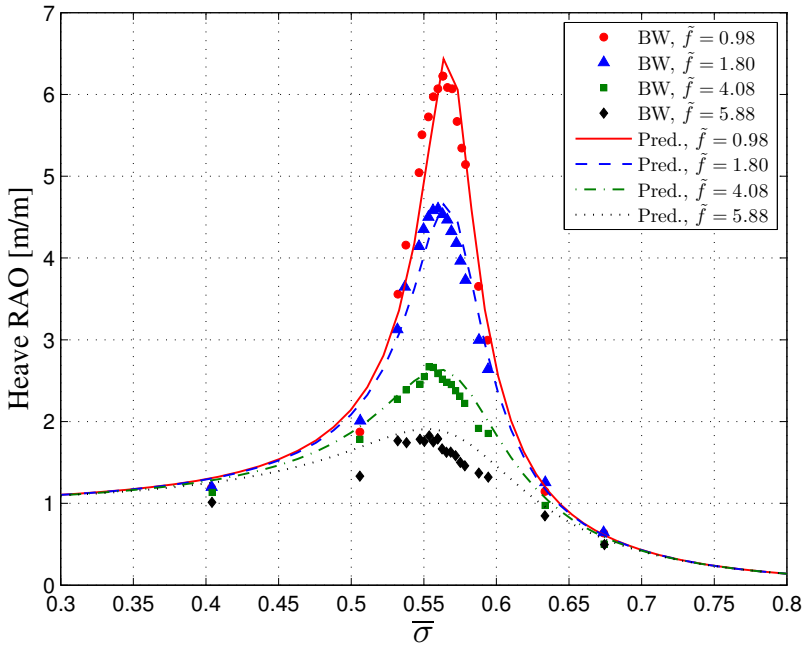

(b) Berkeley Wedge

Figure 4.13: Measured (symbols) and predicted (curves) heave RAO for the FB and BW shapes

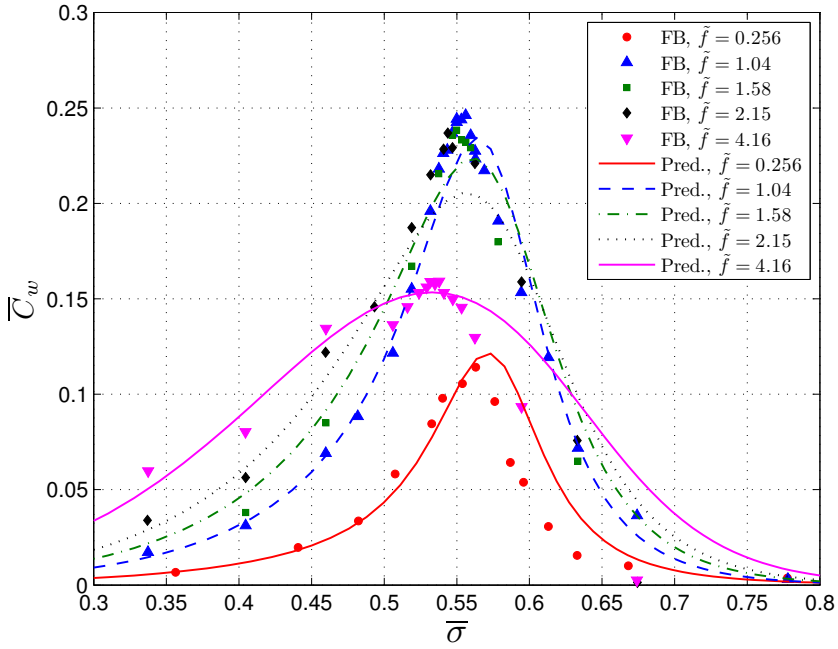

(a) Flat bottom

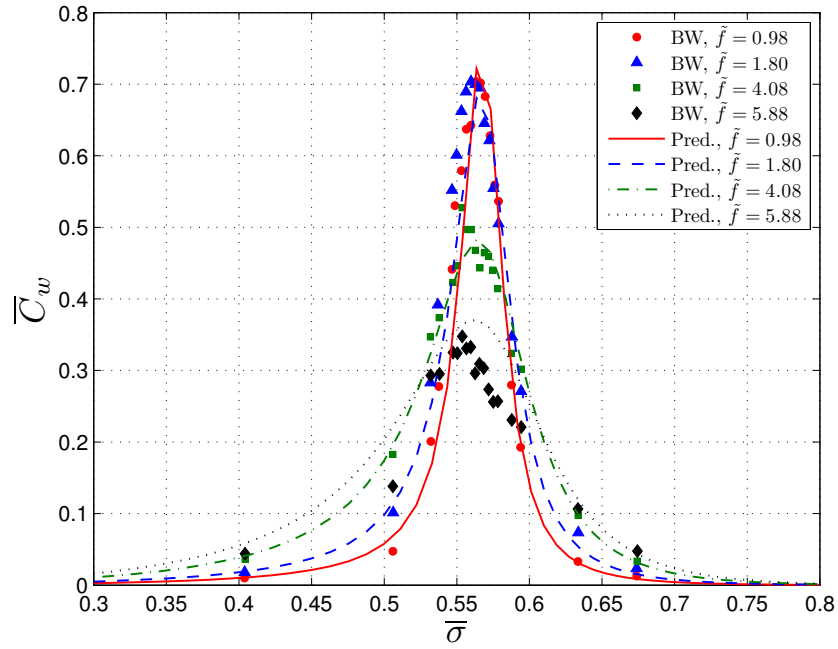

(b) Berkeley Wedge

Figure 4.14: Measured (symbols) and predicted (curves) non-dimensional capture width for the FB and BW shapes

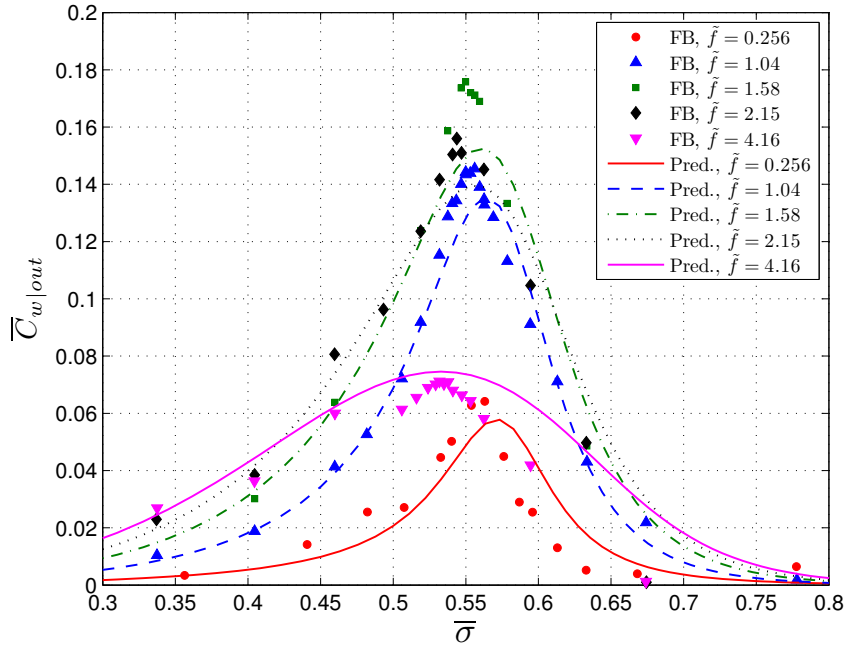

(a) Flat bottom

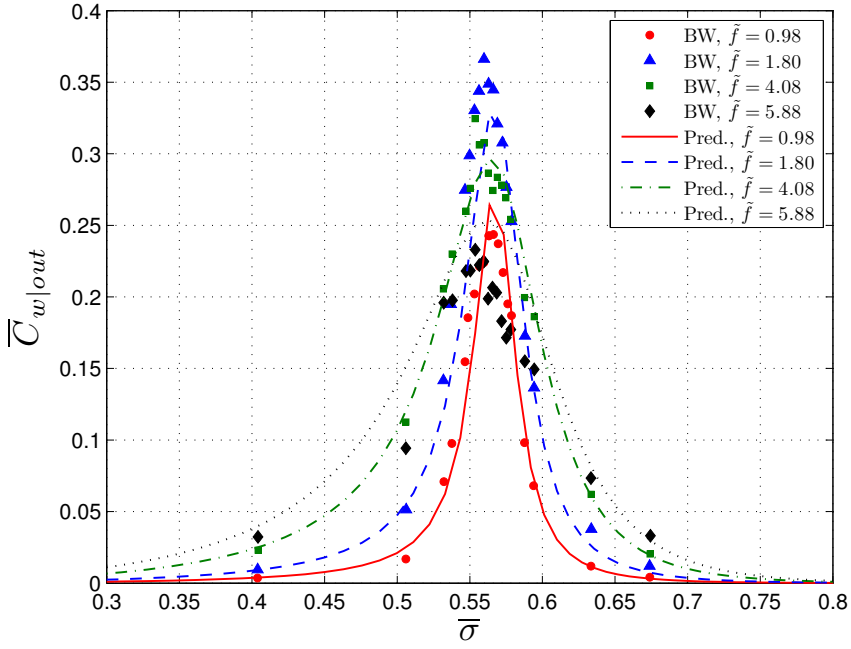

(b) Berkeley Wedge

Figure 4.15: Measured (symbols) and predicted (curves) non-dimensional effective capture width for the FB and BW shapes

Table 4.4: Experimental results of performance optimization at resonance frequency

		$\tilde{f}$	η_{me}	$\overline{C}_w$	η_{el}	$\overline{C}_{w\|out}$
FB	max. $\overline{C}_w$	1.04	0.999	0.246	0.58	0.144
	max. $\overline{C}_{w\|out}$	1.58	0.949	0.238	0.66	0.176
BW	max. $\overline{C}_w$	0.98	0.999	0.704	0.34	0.244
	max. $\overline{C}_{w\|out}$	1.80	0.918	0.703	0.50	0.366

viscous losses were found from free-decay tests. At resonance frequency, this feature of shaping led to a 67% total damping reduction of the floater, compared to the flat-bottom results. Moreover, an empirically fitted formula of the PMLG unit on the mechanical and electrical efficiency provided the best operating conditions for the generator in terms of the resistor value and magnet-coil gap width, maximizing the useful power output.

This chapter has also presented the wave-tank experiment results to validate the theoretical prediction of the WEC performance. The predictions, based on the inviscid linear-wave theory, were modified by using experimentally determined correction factors on hydrodynamic coefficients to take into account viscous effects. The measurements have shown that the theoretical model was able to predict the performance of this coaxial-cylinder system well.

Furthermore, the performance comparison for both different bottom shapes has demonstrated that the Berkeley Wedge shape led to a three-fold increase in the motion and capture width, and a two-fold increase in the effective capture width, when set at the optimal operating conditions of the PMLG.

Chapter 5

Active Control of the WEC System - Theory and Formulation

The previous chapter showed that modified bottom shape of the floater to reduce viscous separation and optimized operating conditions in terms of load resistance and magnet-coil gap width for PMLG have increased the overall energy extraction efficiency, even in passive control method. However, performance of the dual coaxial-cylinder WEC noticeably decreased when it was operated outside of its resonance frequency. This drawback can be potentially overcome by incorporating an active control, because it has ability to increase the peak capture width and simultaneously widen the bandwidth. For this purpose, active control based on nonlinear model predictive control (NMPC) methodology is applied to a candidate, but realistic, dual coaxial-cylinder wave-energy device with the objective of maximizing energy extraction over a range of incident-wave conditions. The power-conversion efficiency of the PMLG can be included in the control scheme to determine the optimal generator damping profile as a control input. This chapter introduces the overall procedure of the NMPC methodology applied into the current WEC system. In addition, the performance with ideal (100%) or actual power-conversion efficiency of the PMLG is compared to each other and to that of a constant damping value.

5.1 Overview of Active Control

Many control strategies for improving WEC energy extraction in arbitrary sea states have been actively studied [41, 42, 43]. Reactive control, or phase control, is the most well-known control methodology [44]. It tunes the WEC to resonate with incident-wave frequency to have the velocity of the floater in phase with wave-exciting force, which theoretically leads to the maximum energy absorption. It also has been called complex-conjugate control because the optimal impedance of the PTO device should be matched with the complex-conjugate of the intrinsic impedance of the WEC.

To accomplish this task, the floater can be locked in displacement for a certain time period by a mechanical or electrical mechanism, and then released to oscillate at desired wave conditions. This approach, namely latching control, can be a way to realize the reactive control, or phase control [45, 46, 47]. Even though it is a simple concept to control the system, a large reactive or latching force to lock the floater in has to be applied with fast response time, which will be impediment in practice.

These active control approaches definitely increase the energy extraction compared to the passive control, i.e., without control. However, these methods may not be effective for

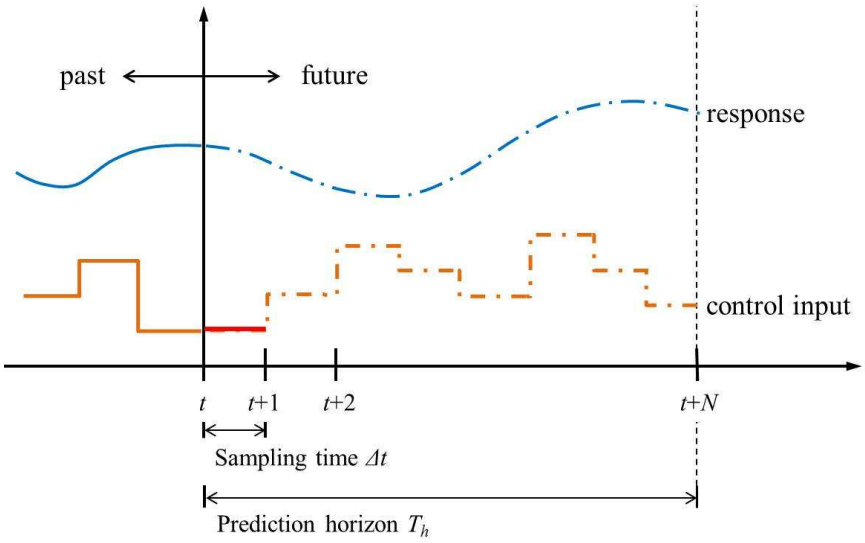

Figure 5.1: Principle schematic of model predictive control strategy, where $t + j$ stands for $t + j\Delta t$

real-time control because they are based on the frequency-domain analysis.

5.2 Model Predictive Control Strategy

Model predictive control (MPC) is an advanced control methodology based on a time-domain analysis. The MPC technique is quite simple and straightforward to understand. It is also suitable for handling the constraints explicitly. Basically, MPC predicts the future response of the system to find optimal control input. Figure 5.1 describes the general procedure and principle of the MPC strategy:

- At time t, a discrete optimal control problem is solved over a finite future time horizon T_h of N steps with a prediction of response or state.
- Only the first value of computed optimal control input is applied to the system, which is indicated by red line.
- At the next time step $t + 1$, the window of prediction horizon T_h is shifted, and the optimization problem is repeated.

A MPC applied into ocean-wave energy converter enables the optimization of energy capture in real-time under certain given constraints, such as motion limitation and device capability [48, 49, 50, 51, 52, 53, 54, 55]. Because MPC considers constraints in a control scheme, a MPC controlled-WEC system exhibits better performance than other adaptive

control strategies: velocity-proportional control, approximate complex conjugated control, approximate optimal velocity tracking, and phase control by latching and clutching [53]. The cited references mentioned previously have been focused to find optimized velocity of the floater and reaction force from the PTO, which allow problem to be solved as a convex quadratic programming (QP) problem that has fast execution algorithm.

Moreover, nonlinear model predictive control (NMPC) was introduced to account for nonlinear effects from mooring force [56] or a time-varying PTO damping [57, 58]. They have found that the optimal control is of bang-bang control sequence [57, 58, 59]. In particular, the work referenced in [58] formulated the PTO force as a function of instantaneous damping and floater velocity. The study focused on solving the time-varying PMLG damping as a controllable parameter without incorporating active elements for reactive force control. This can be a more practical approach to controlling the PMLG, and it prevents feeding energy back into the waves. Aside from theoretical simulations, the effectiveness of the implemented NMPC was experimentally validated by setting an electrical on-off activation period on the PMLG [60].

The current study is mainly based on the previously constrained NMPC work conducted by [58]. However, previous research on control strategies applicable to the WEC was mainly aimed at maximizing power absorption from incoming waves. In reality, the mechanical to electrical power conversion efficiency of the PTO is also a critical factor in determining the useful electrical power output. Thus, this study is to investigate the benefits of NMPC technology by incorporating the electrical conversion efficiency of the PMLG for the model-scale dual coaxial-cylinder WEC system so as to maximize useful electrical power output.

One of the difficulties in wave-energy extraction is the wave-forecasting problem, which is still challenging and untapped. For real-time control of the WEC system, prediction of the incident-wave field for short term is an essential part of the control process because of the non-causal nature of the wave-exciting force. However, in this study, prediction of incident-wave elevation is assumed to be perfect, and so wave-exciting force is a known factor.

5.3 Mathematical Modeling of WEC in Time Domain

5.3.1 Dynamics of the Fully Coupled System

To implement the NMPC methodology on the WEC, time-domain analysis, instead of frequency-domain analysis, is needed to allow for a controller input on a wave-by-wave basis. Under the linear-theory assumptions, equation of motion of the floater Eqn. (2.3) with linear generator force $F_g(t)$ is given by

$$m_2\ddot{\zeta}_3(t) = F_3^{st}(t) + F_3^{exc}(t) + F_3^{rad}(t) + F_g(t) \tag{5.1}$$

The hydrostatic restoring force $F_3^{st}(t)$ and the generator force $F_g(t)$ with the dominant term are already introduced in Eqn. (2.4) and Eqn. (2.16), respectively. The frequency-dependent hydrodynamic coefficients such as added mass, wave damping, and wave-exciting

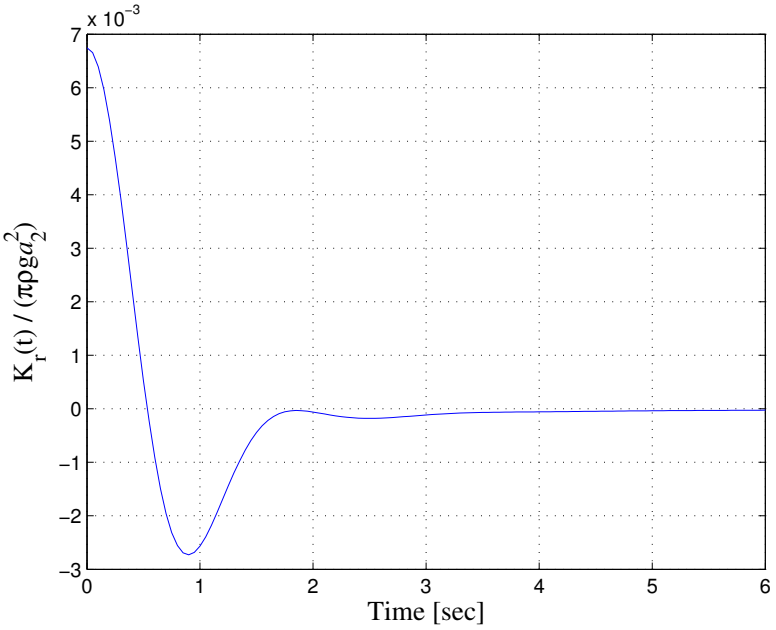

Figure 5.2: Non-dimensional radiation impulse response function

force are related to the time-domain analysis through the Fourier transform. Thus, the radiation force and the wave-exciting force in the time domain are expressed by convolution operators. The wave-radiation force in the time domain from [61, 62] can be expressed as

$$F_3^{rad}(t) = -\mu_{33}(\infty)\ddot{\zeta}_3(t) - \int_0^t K_r(t-\tau)\dot{\zeta}_3(t)\ d\tau \tag{5.2}$$

where $\mu_{33}(\infty)$ is the added mass at infinite frequency and the convolution integral represents the fluid memory effect where K_r is the causal radiation impulse response function, or retardation. It describes that the radiation force consists of the inertial reaction of the fluid when the body starts to move and continuous reaction for subsequent time as convolution term. It can be computed by the inverse Fourier transform of either added mass μ_{33} or wave damping λ_{33}, which is shown in Fig. 5.2:

$$\begin{aligned} K_r(t) &= -\frac{2}{\pi}\int_0^\infty \sigma[\mu_{33}(\sigma) - \mu_{33}(\infty)]\sin\sigma t\ d\sigma \\ &= \frac{2}{\pi}\int_0^\infty [\lambda_{33}(\sigma) - \lambda_{33}(\infty)]\cos\sigma t\ d\sigma \end{aligned} \tag{5.3}$$

The wave damping at infinite frequency usually vanishes, i.e., $\lambda_{33}(\infty) = 0$, see Fig. 4.10. The wave-exciting force can be expressed as

$$F_3^{exc}(t) = \int_{-\infty}^\infty K_e(t-\tau)\eta(0,t)\ d\tau \tag{5.4}$$

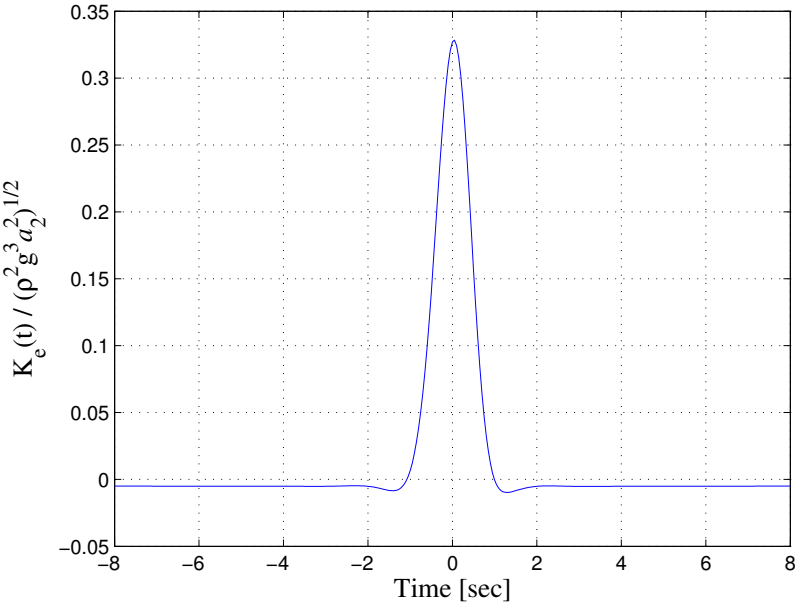

Figure 5.3: Non-dimensional wave-exciting force impulse response function

where $\eta(0,t)$ is the incident-wave elevation at the cylinder axis. The impulse response function K_e can be obtained from the inverse Fourier transform of the complex wave-exciting force amplitude per unit incident-wave amplitude X_3, see Fig. 5.3:

$$\begin{aligned} K_e(t) &= \frac{1}{2\pi}\Re\left\{\int_{-\infty}^{\infty} X_3(\sigma)\ e^{i\sigma t}\ d\sigma\right\} \\ &= \frac{1}{2\pi}\Re\left\{\int_{0}^{\infty} [X_3(\sigma)e^{i\sigma t} + X_3(-\sigma)e^{-i\sigma t}]\ d\sigma\right\} \\ &= \frac{1}{\pi}\int_{0}^{\infty} [\Re\{X_3(\sigma)\}\cos\sigma t - \Im\{X_3(\sigma)\}\sin\sigma t]\ d\sigma \end{aligned} \tag{5.5}$$

The non-causality function K_e implies that the wave-exciting force is independent of the floater motion. In other words, the force induced by wave exerts before wave reaches the body origin. It can be approximated to the solution of the causal function, like the radiation force, with a positive time shift [63]. Non-causal problem do indeed require prediction of the incident wave. However, in this research, the incoming-wave elevation is assumed full knowledge, so once $X_3(\sigma)$ is known, the wave-exciting force is used as the given input for simulation.

Finally, inserting all of these, the equation of motion for the outer cylinder can be re-

written as

$$[m_2 + \mu_{33}(\infty)]\ddot{\zeta}_3(t) + [\lambda_{vis} + B_g(t)]\dot{\zeta}_3(t) + K_{33}\zeta_3(t) + \int_0^t K_r(t-\tau)\dot{\zeta}_3(t)\ d\tau = \int_{-\infty}^{\infty} K_e(t-\tau)\eta(0,t)\ d\tau \tag{5.6}$$

Or, with known input of wave-exciting force:

$$[m_2 + \mu_{33}(\infty)]\ddot{\zeta}_3(t) + [\lambda_{vis} + B_g(t)]\dot{\zeta}_3(t) + K_{33}\zeta_3(t) + \int_0^t K_r(t-\tau)\dot{\zeta}_3(t)\ d\tau = \Re\{|X_3(\sigma)|e^{i\delta_3}\}\eta(0,t) \tag{5.7}$$

Here, the linear-viscous damping term λ_{vis} is inserted in order to model the effect of a real fluid. This integro-differential equation of Eqn. (5.6) forms a time-variant system with a controllable input of generator damping $B_g(t)$ and an uncontrollable input of wave-exciting force.

5.3.2 State-Space Realization for Convolution Term

It is efficient to calculate time-domain analysis using the state-space realization method [63, 64, 65, 66, 67, 68]. The convolution integral of the radiation force is considered as an output of a time-invariant linear sub-system with an input $\dot{\zeta}_3(t)$:

$$\begin{aligned} \dot{X}_r(t) &= A_r X_r(t) + B_r \dot{\zeta}_3(t) \\ \int_0^t K_r(t-\tau)\dot{\zeta}_3(t)\ d\tau &\approx C_r X_r(t) \end{aligned} \tag{5.8}$$

where $X_r(t)$, A_r, B_r, and C_r are an n-th order radiation state matrix, an $n \times n$ state matrix, an $n \times 1$ input matrix, and a $1 \times n$ output matrix, respectively. The state-space realization is available in the MATLAB function *imp2ss* which is based on Hankel singular value decomposition that produces high-order system with over 200 states.

The order of radiation states should be large enough to describe the impulse response K_r well, but small enough to simplify the system and to reduce the computational cost. Figure 5.4 shows the contribution of each state to describe whole system. As a result, first two states mainly contribute to the behavior, and small values over six-order can be discarded. A reduced-order model is achieved by using the MATLAB function *balmr*. To evaluate the quality of the reduced model for the impulse response function more precisely, R^2-value can be used [67]:

$$R^2 = 1 - \frac{\sum(K_r^{IFT} - K_r^i)^2}{\sum(K_r^{IFT} - K_r^m)^2} \tag{5.9}$$

where K_r^{IFT} is from the direct inverse Fourier transform considered as a reference, K_r^m is the mean value of reference, and K_r^i is the reduced model having i number of states.

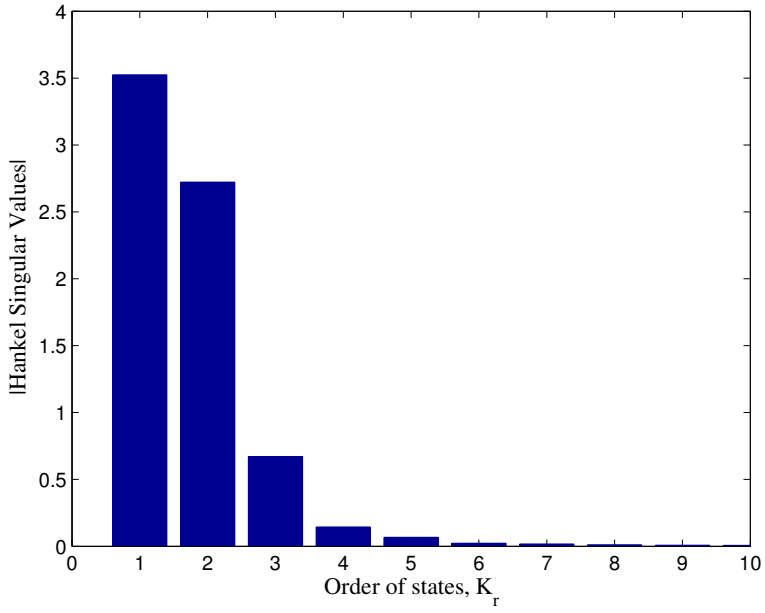

Figure 5.4: Hankel singular value of impulse response function

The reduced-order impulse response functions are shown in Fig. 5.5 with the reference computed directly from the inverse Fourier transform, using the radiation damping values of Eqn. (5.3). As a result, a mere three radiation states are enough to approximate K_r accurately with over 0.99 R^2-value, see Table 5.1.

5.3.3 Formulation into Stat-Space Representation

The heave equation of motion for the outer cylinder in time domain of Eqn. (5.7) can now be expressed with three radiation states $X_r(t)$ in the state-space form:

$$\dot{X}(t) = A(t)X(t) + B\eta(t) \tag{5.10}$$

Table 5.1: R^2-value of reduced model for radiation convolution term.

Model order	2	3	4	5	8
R^2-value	0.9631	0.9988	0.9989	0.9999	0.9999

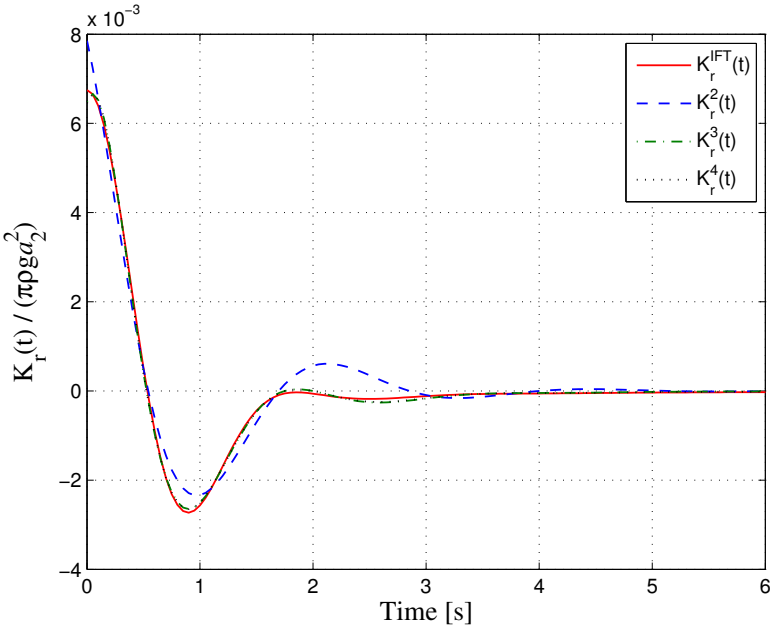

Figure 5.5: Non-dimensional impulse response function with reduced-order model

where

$$A(t) = \begin{bmatrix} A_r & 0 & B_r \\ 0 & 0 & 1 \\ \frac{-C_r}{m_2+\mu_{33}(\infty)} & \frac{-K_{33}}{m_2+\mu_{33}(\infty)} & \frac{-[\lambda_{vis}+B_g(t)]}{m_2+\mu_{33}(\infty)} \end{bmatrix} \tag{5.11}$$

$$X(t) = \begin{bmatrix} X_{r1}(t) \\ X_{r2}(t) \\ X_{r3}(t) \\ \zeta_3(t) \\ \dot{\zeta}_3(t) \end{bmatrix}, \quad B = \begin{bmatrix} 0 \\ 0 \\ 0 \\ 0 \\ \frac{\Re\{|X_3(\sigma)|e^{i\delta}\}}{m_2+\mu_{33}(\infty)} \end{bmatrix} \tag{5.12}$$

The system state matrix $A(t)$ includes the unknown time-dependent generator damping $B_g(t)$ which is now to be determined as the controllable input.

5.4 Nonlinear-MPC Programming

5.4.1 Objective Function and Constraints

A continuous optimization problem to find local solution forms mathematically

$$\begin{aligned} \min_{x \in R^n} \quad & f(x) \\ \text{s.t.} \quad & g(x) \leq 0 \\ & h(x) = 0 \\ & x_L \leq x \leq x_U \end{aligned} \tag{5.13}$$

where $f(x)$ is the objective function, $g(x)$ and $h(x)$ are constrain functions, and the vectors x_L and x_U are the bounds on the variable x. The functions $f(x)$, $g(x)$, and $h(x)$ can be nonlinear and non-convex, but should be twice continuously differentiable.

Ocean-wave energy is transferred to the WEC, and then the PTO converts the absorbed mechanical power into useful electrical power. During the power transferring process, the maximum power absorbed from the waves does not guarantee a maximum electrical power output. The mechanical to electrical power conversion process depends upon the efficiency of the PTO system η_{el}, as discussed in the previous chapter. Since this research aims to maximize the electrical power output, the conversion efficiency of the PMLG η_{el} should be inserted into the control algorithm.

Upon multiplying the absorbed power Eqn. (2.20) by the conversion efficiency η_{el}, an objective function can mathematically define an objective function for NMPC in order to maximize the electrical power output over a time horizon T_h as

$$\begin{aligned} &\max_{B_g} \int_{t_0}^{t_0+T_h} \eta_{el} B_g(t) \dot{\zeta}_3^2(t)\ dt \\ &= \min_{B_g} \int_{t_0}^{t_0+T_h} \{-\eta_{el} B_g(t) \dot{\zeta}_3^2(t)\ dt\} \end{aligned} \tag{5.14}$$

Since the NMPC solves the optimization problem in discrete time, the objective function in discrete time is now given by

$$\min_{B_g} \sum_{k=1}^{N} \{-\eta_{el} B_g(k) \dot{\zeta}_3^2(k) \Delta t\} \tag{5.15}$$

where $N = T_h/\Delta t$ is the number of time steps within the horizon T_h and Δt is sampling time.

Furthermore, a quadratic penalty term for the generator force change is included for a smoother PMLG response and better numerical stability [26, 50, 56, 69]. It may also reflects some energy losses for the PMLG operation and the resistive loss when adjusting the generator damping to the desired value. In addition, for overall reasonable operation, two

physical states are constrained: generator damping capacity and motion amplitude of the floater. One constraint on the damping capacity is that it is limited by the allowable PMLG damping $B_{g|max}$. The other constraint is that a physical overlap between the translator and the coils must be maintained, and heave motion is restricted to $\pm l$, with l being 0.216 m, subtracting length of the stator from length of the translator and then divided by 2. The discrete-time objective function, including the penalty term, subject to constraints is now

$$\begin{aligned} \min_{B_g} \ & \sum_{k=1}^{N} \Big\{ -\eta_{el} B_g(k) \dot{\zeta}_3^2(k) + Q_p [\Delta B_g(k) \dot{\zeta}_3(k)]^2 \Big\} \Delta t \\ \text{s.t.} \ & 0 \leq B_g(k) \leq B_{g|max} \\ & -l \leq \zeta_3(k) \leq l \end{aligned} \tag{5.16}$$

where $\Delta B_g(k) = B_g(k) - B_g(k-1)$ and Q_p is a positive penalty weight.

5.4.2 Efficiency of the PMLG in the objective function

In PMLG design, the generator damping B_g and the conversion efficiency η_{el} are regulated by the magnet-coil gap width w_{gap} and the applied load resistor R connected to the coils. When the w_{gap} is set, the damping B_g is regulated by the change of resistance R. The conversion efficiency η_{el} of the PMLG used in Eqn. (5.16) needs to have expression as a function of generator damping B_g for consistency of the objective function. A plausible fits of η_{el} as a function of B_g for different w_{gap} reconstructed from Eqn. (3.8) to insert into the objective function is

$$\eta_{el}(B_g, w_{gap}) = \frac{A(w_{gap}) \cdot B_g^n}{[B_g + C(w_{gap})]^m} \tag{5.17}$$

Figure 5.6 shows the reconstructed power conversion efficiency of the PMLG η_{el} from the empirical fits as a function of its damping B_g for different magnet-coil gap width w_{gap}. Each gap width w_{gap} has different peak of η_{el} within adjustable range of B_g. As w_{gap} decreases, a peak efficiency increases with shifting towards higher damping B_g value, and range of damping B_g to be controlled is getting widen.

5.4.3 Approach for Simulation

In this study, time-varying PTO damping $B_g(t)$ is now considered as a physical controllable input. Thus, the constrained NMPC algorithm determines the optimal control input $B_g(t)$ in order to maximize useful power output over a time horizon, which minimizes the objective function.

The optimization was designed to find optimal local time-varying solutions through iteration using a nonlinear solver. In this work, the Interior Point Optimizer (IPOPT) solver was used with HSL libraries [70]. In addition, the Berkeley Library for Optimization Modeling (BLOM) was used, which is a Matlab/Simulink toolbox [71]. Within this toolbox, intuitive

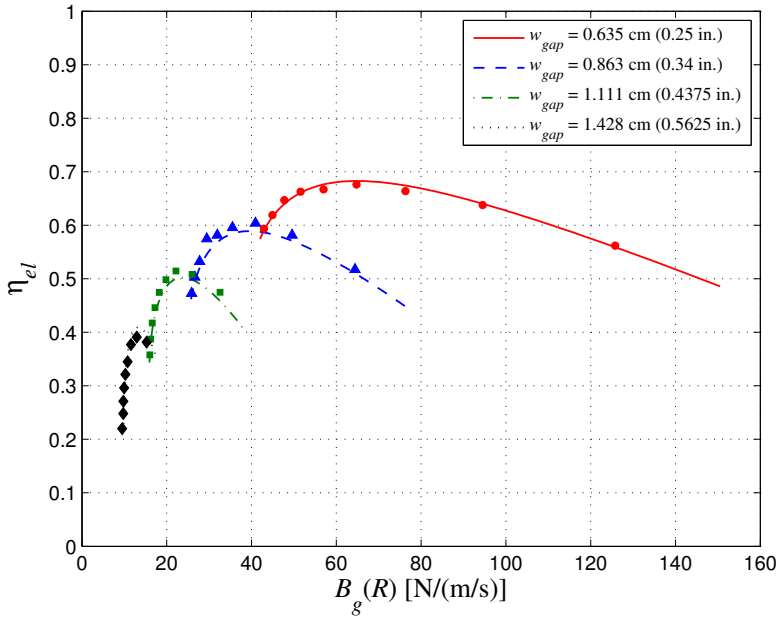

Figure 5.6: Energy conversion efficiency of the PMLG as a function of generator damping for different magnet-coil gap width

blocks are used to automatically formulate the nonlinear optimization problem. Then, the problem is exported to a solver. Figure 5.7 shows the constructed optimization problem of the system expressed in Eqns. (5.10) and (5.16) using the BLOM function blocks.

5.4.4 Effect of Simulation Parameters on Results

Several tuning parameters for the simulation are believed to affect the WEC system response: the time horizon T_h, time step Δt, and the penalty weight Q_p. Here, the simulation sensitivity to these tuning parameters is addressed.

The penalty weight Q_p can be intuitively selected to prevent fast erratic change in generator force, but should be small compared to the main term described in Eqn. 5.15. If the penalty weight has a large value, it leads to less PMLG reaction dynamics and poor performance. It is observed that the generator force no longer changes with Q_p for Q_p less than 10^{-4}, see Fig. 5.8. In addition, a value lower than $Q_p = 10^{-6}$ is sufficient in the simulation to have stable time-averaged power absorption for any wave periods presented in Fig. 5.9.

The effect of time horizon and time step on energy-capture performance was carried out at resonance frequency, which is shown in Fig. 5.10. A study of time horizon variation showed that dependency on time horizon disappears, regardless of the time step size, when information from two periods ahead is known. Moreover, the smaller time step gives better performance in general, but it consumes more time and its effect is negligible if the time

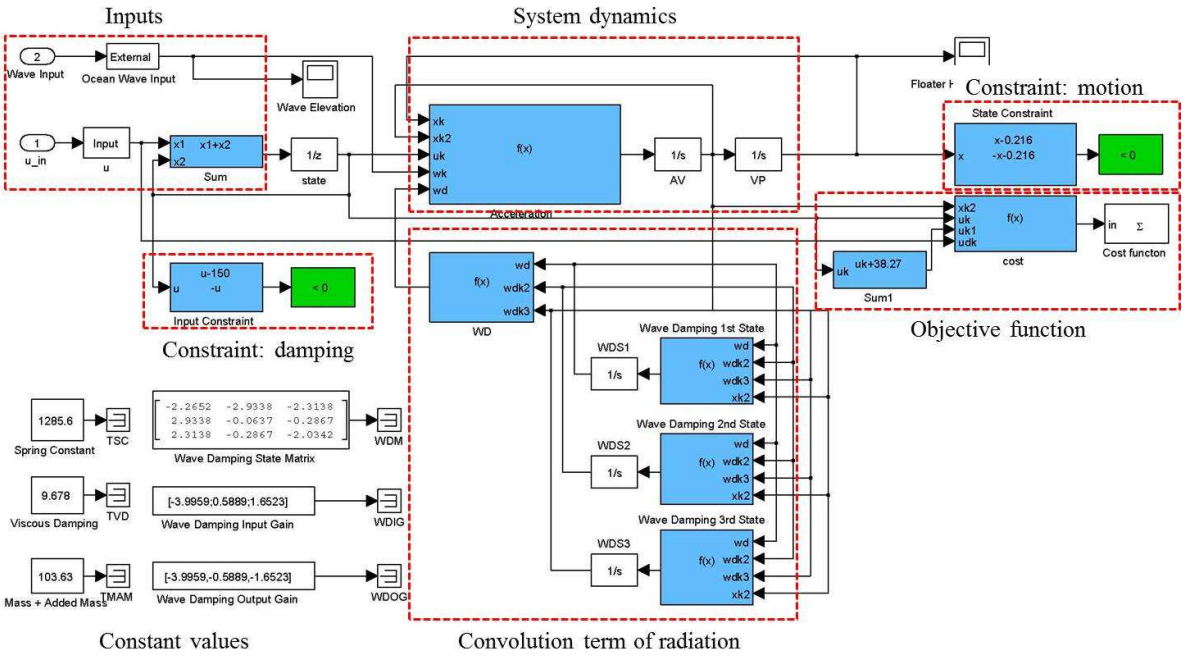

Figure 5.7: Simulink model of the optimization problem using BLOM function blocks

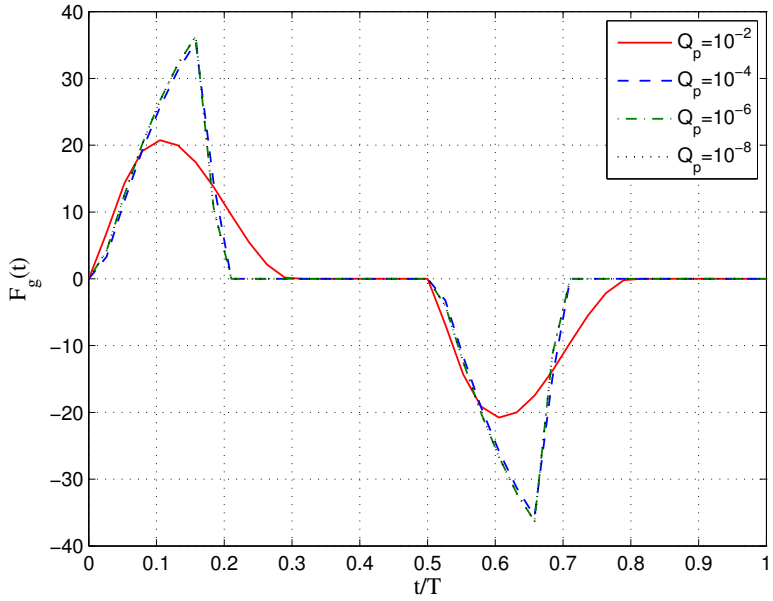

Figure 5.8: Generator force response with different penalty weight Q_p at T=1.9 sec

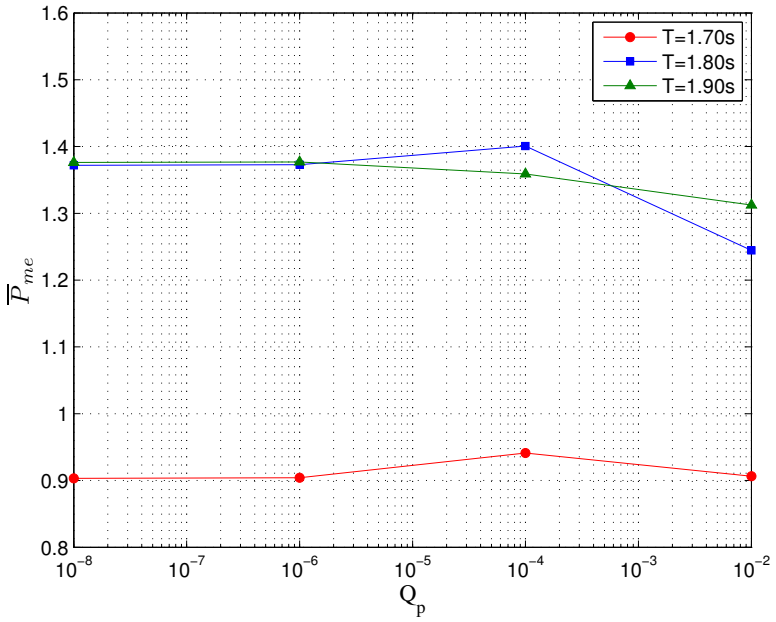

Figure 5.9: Effects of penalty weight on the time averaged power absorption for different wave periods

horizon is adequately long.

Based on this preliminary studies, a sampling time Δt of 0.05 sec, a prediction time horizon T_h of $2T$, and a penalty weight Q_p of 10^{-6} were selected to capture the advantage of active control for any wave periods. The initial conditions of heave displacement ζ_3 and velocity $\dot{\zeta}_3$ of the floater were set to zero for all simulations, and an incident-wave amplitude A of 0.0254 m was used.

5.5 NMPC Simulation Results in Regular Waves

5.5.1 Frequency-Domain Results

The NMPC results for the PMLG damping control in the frequency domain are presented in Fig. 5.11 through Fig. 5.13 for a given magnet-coil gap width w_{gap} of 0.635 cm. For comparison purposes, the plotted results are:

(a) Active control with ideal PTO efficiency, i.e., $\eta_{el} = 1$; it is the same as maximizing the absorbed power P_{me}.

(b) Active control with actual PMLG efficiency η_{el}; it maximizes the useful power output P_{el}.

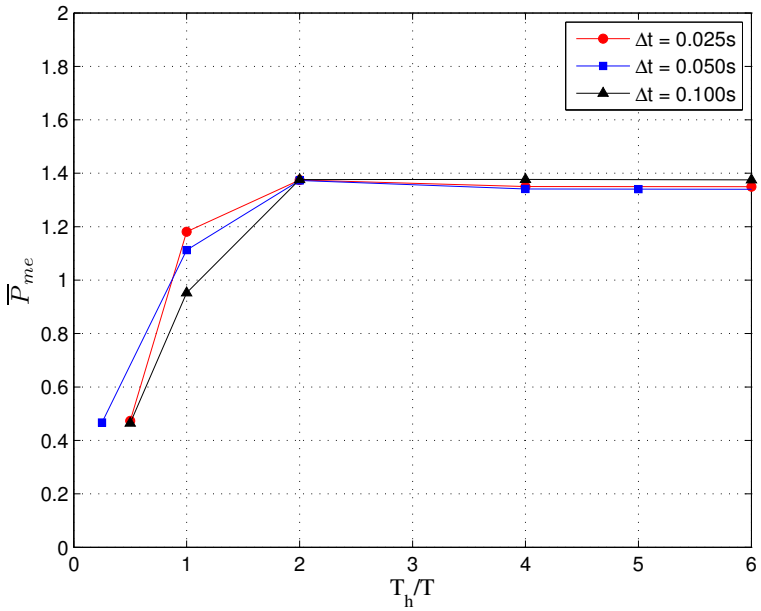

Figure 5.10: Effects of time horizon on the time averaged power absorption for different wave periods at T=1.8 sec

(c) Passive control with $\tilde{f} = 10$, at which it has a maximum allowable damping $B_{g|max}$; (2Ω, 0.635 cm)

(d) Passive control with $\tilde{f} = 5$, at which it has the maximum η_{el}; (9Ω, 0.635 cm)

(e) Passive control at optimal operating condition maximizing P_{el} at resonance, $\tilde{f} = 1.8$; (9Ω, 1.111 cm)

The performances of the WEC are strongly affected by the electrical efficiency of the PMLG η_{el} and damping value B_g. For actively controlled cases in RAO (see Fig. 5.11), case(a) yields about twice the motion response at the resonance frequency than case(b) because case(a) targeted only the maximization of mechanical power absorption. It is achieved by increasing motion response of the floater. The peak of non-dimensional capture width $\overline{C}_w$ in Fig. 5.12 shows that case(a) is increased by about 1.5 times compared to case(b). The non-dimensional effective capture width $\overline{C}_{w|out}$ of Fig. 5.13, however, shows that case(b), which considers the actual η_{el}, has slightly better performance and comparable near the peak frequency. Note that the $\overline{C}_{w|out}$ results for case(a) were obtained by simply multiplying by the actual η_{el} to the $\overline{C}_w$ results after simulation. These comparisons explain why including the power-conversion efficiency of the PMLG in the control scheme is important. It would be more efficient and stable in terms of survivability because much less motion is needed to get the same amount of useful power out.

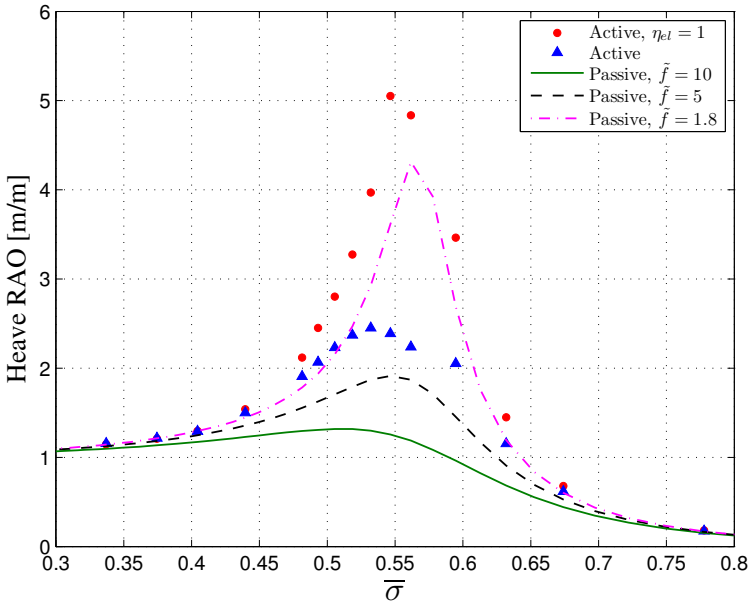

Figure 5.11: Comparison of Heave RAO for active and passive control

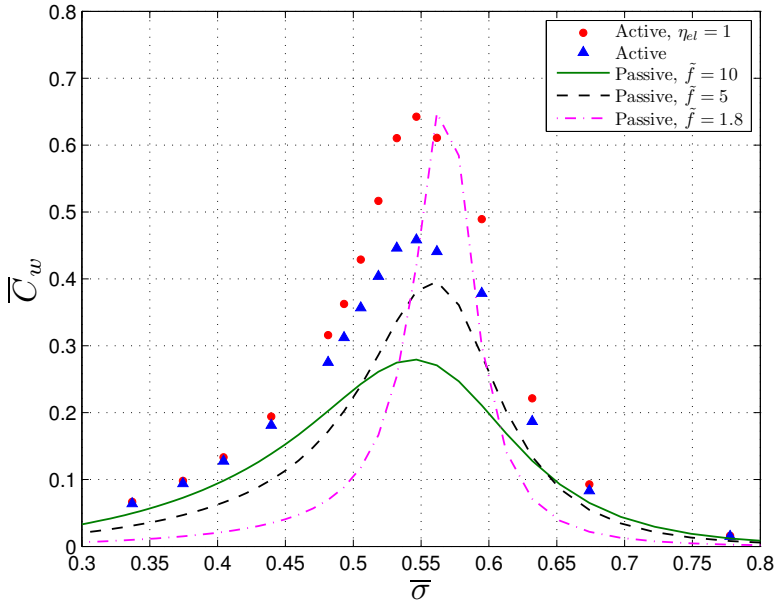

Figure 5.12: Comparison of capture width for active and passive control

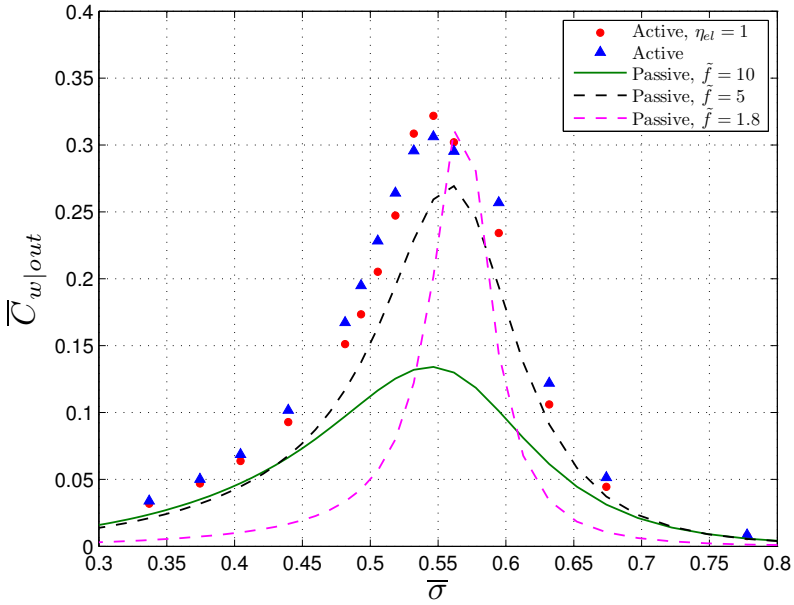

Figure 5.13: Comparison of effective capture width for active and passive control

For passive modes of case(c)-(e) represented by lines, peaks of performance decrease with damping value greater than $\tilde{f} = 1.8$, which is expected, while bandwidth increases. For the current operating principle of the coaxial-cylinder WEC system, the passive control sacrifices peak value to widen bandwidth, while the active control leads to increase in both peak and bandwidth.

Further, as can be observed in Figs. 5.11-5.13, the peak value tends to shift to lower frequencies when the damping is increased. Comparison of active control to passive control shows that active control leads to an increased peak value and bandwidth of the energy extraction for the frequency range shown. For example, under the same setting conditions of $\tilde{f}$=10, the active control of case(b) extracts more than 2 times energy at resonance frequency compared to the passive control of case(c), Fig. 5.13.

5.5.2 Effects of PMLG Capacity on Performance

The constructed active control optimizes time-varying $B_g(t)$ within the maximum allowable value $B_{g|max}$, which is determined by the magnet-coil gap width w_{gap}. At the same time, η_{el} of the PTO shows different dependencies on B_g for different w_{gap}, as shown in Fig. 5.6. To investigate the effect of $B_{g|max}$ on the performances, three active control cases were selected and compared:

(a) $\tilde{f}_{max} = 6$; w_{gap}=0.794 cm

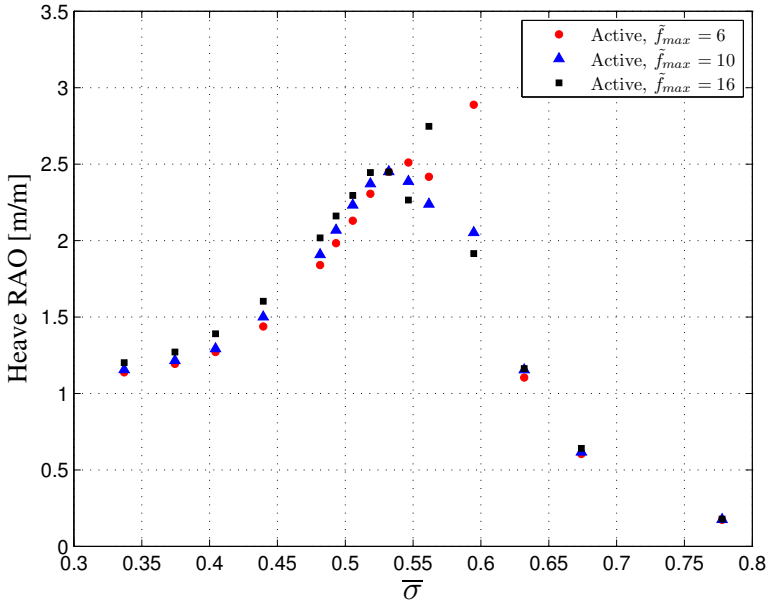

Figure 5.14: Active control results of Heave RAO for different $B_{g|max}$ values

(b) $\tilde{f}_{max} = 10$; w_{gap}=0.635 cm

(c) $\tilde{f}_{max} = 16$; w_{gap}=0.476 cm

Figures 5.14-5.16 show the results of NMPC simulation with different $B_{g|max}$. Increases in $\overline{C}_w$ and $\overline{C}_{w|out}$ were obtained when $B_{g|max}$ increases; however, the heave response shows no significant difference. The gain from the higher $B_{g|max}$ at lower frequencies is greater than at higher frequencies because of the shifts in peak $\overline{C}_w$ and $\overline{C}_{w|out}$. As a result, a smaller w_{gap} configuration that allows for higher $B_{g|max}$ and better η_{el} leads to improved performances of energy extraction, unless a higher cogging force at smaller w_{gap} is considering.

5.5.3 Time-Domain Results

As a result of the NMPC simulation, the optimal generator damping $B_g(t)$ was determined in a time series. The suggested damping behaviors for the wave periods of [1.3 s, 4.0 s] and w_{gap}=0.635 cm are plotted in Fig. 5.17, where the optimal damping value is normalized by maximum damping capacity $B_{g|max}$. A contour map projected from the damping behavior, located at the bottom, simply shows the pattern and values to be set with one motion cycle of the floater. The corresponding heave displacement of the floater $\zeta_3(t)$ normalized by the maximum value $\zeta_{3|max}$ is plotted in the same figure.

The NMPC results with the ideal power conversion efficiency $\eta_{el} = 1$ implies that the absorbed mechanical power is maximized; the results are plotted in Fig. 5.17(a). The on-off

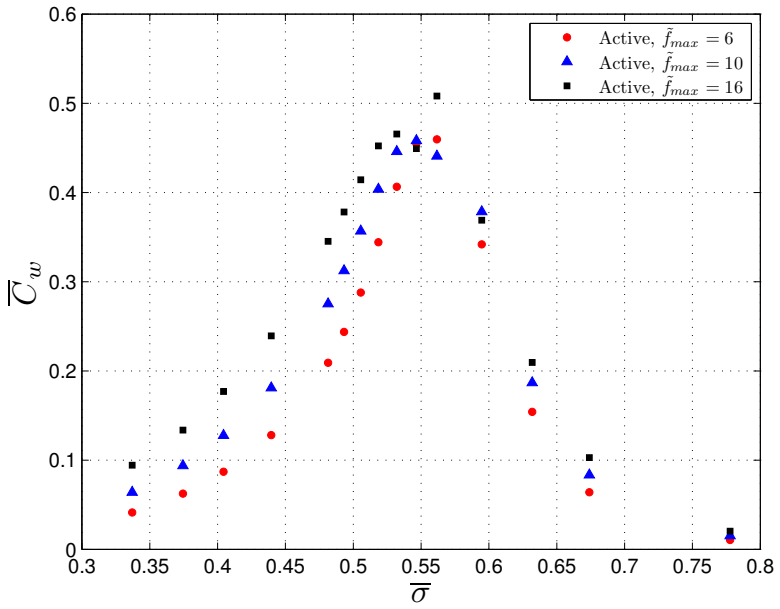

Figure 5.15: Active control results of capture width for different $B_{g|max}$ values

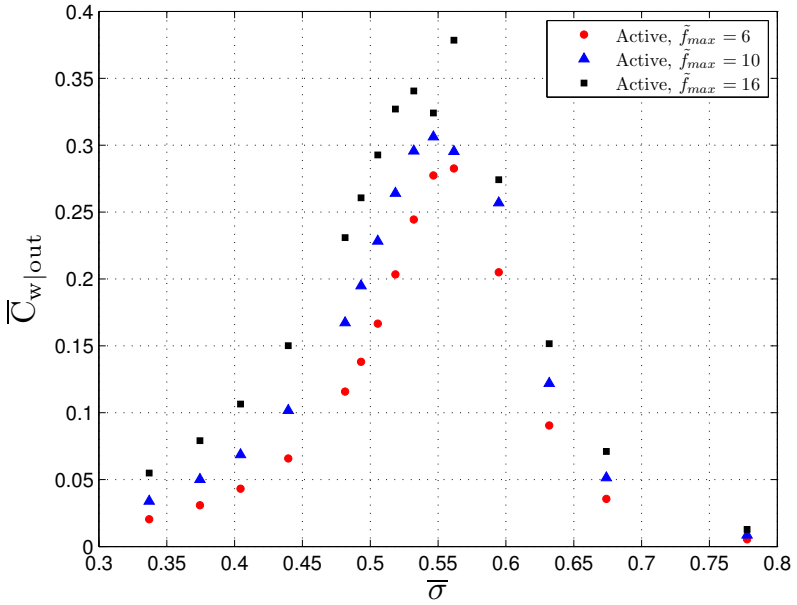

Figure 5.16: Active control results of effective capture width for different $B_{g|max}$ values

sequence, or bang-bang control profile, is retrieved and is shown in the previous investigations in [26, 57]. However, inclusion of the actual electrical efficiency gives a quite different behavior as shown in Fig. 5.17(b). The suggested optimal damping profiles have a transient value between zero and unity ($B_{g|max}$).

It became apparent that the η_{el} of the PMLG makes optimal damping time-history alteration and should be included in the control process to maximize the useful power extraction. In practice, the on-off sequence can be implemented with a mechanical on-off relay for the PTO damping bang-bang control [26]. However, for the optimal control with transient value, a more complicated controller is required to adjust damping value. A simple on-off controller is not adequate for these new results.

For example, direct comparison of the optimal damping behavior considering the ideal and the actual efficiency at T=1.9 sec is shown in Fig. 5.18. When considered the actual η_{el}, the PMLG has a two-times longer activating duration, with an transient values between zero and unity. This longer duration of the activated PMLG resulted in a smaller heave motion response, as shown in 5.11. Figure 5.19 shows the optimal damping profile for different incident-wave periods. When wave period is moving away from the resonance, $B_{g|max}$ is retained for longer period of time and approaches the bang-bang type profile, because a larger damping value is required to compensate for the reduced motion. For the different $B_{g|max}$ values achieved by changing the w_{gap} at T=1.9 sec, the NMPC tends to increase the duration of activation, but $B_g(t)$ is still strongly time dependent, which is shown in Fig. 5.20.

Figure 5.21 through Fig. 5.24 represent the performances of the WEC system in a time series at T=1.9 sec. The results for passive control with $\tilde{f} = 4$ are also plotted for comparison, which represent the optimal passive condition maximizing the electrical power output P_{el}. Figure 5.22 shows that active control pushes the floater velocity to have the same phase as the wave-exciting force, and enhances the maximum peak velocity as well. Moreover, the discontinuous damping behavior leads to the inconstant generator force and electrical power output, which are shown in Fig. 5.23 and Fig. 5.24. However, the peak and mean of the electrical power with active control are improved by 45% and 25% at T=1.9 sec, respectively.

5.6 NMPC Simulation Results in Irregular Waves

The proposed NMPC strategy was then applied in the irregular-wave condition for the final environment. The simulation set-up was based on a regular-wave condition, and mainly investigated how much energy extraction could be achieved by applying the proposed NMPC strategy.

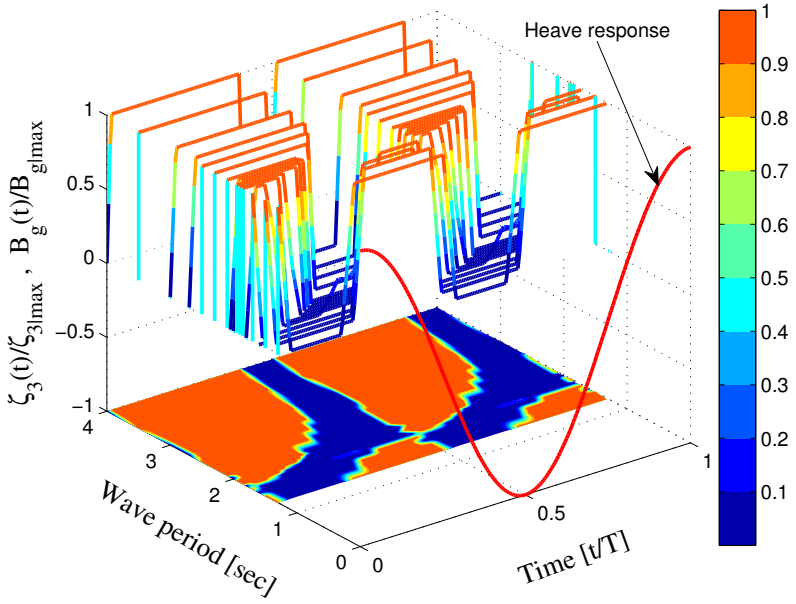

(a) Assuming the ideal efficiency of the PMLG $\eta_{el} = 1$

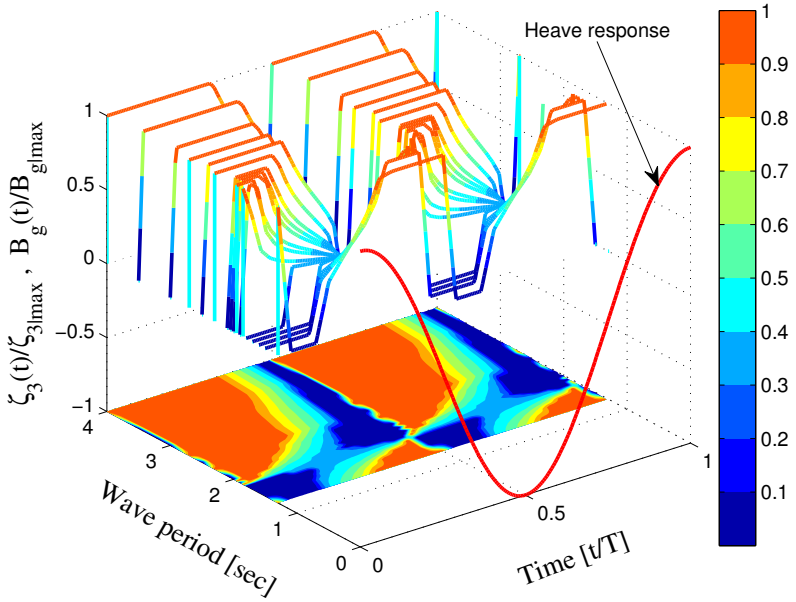

(b) Considering the actual conversion efficiency of the PMLG

Figure 5.17: Desired linear generator damping behavior map in regular waves, w_{gap}=0.635 cm

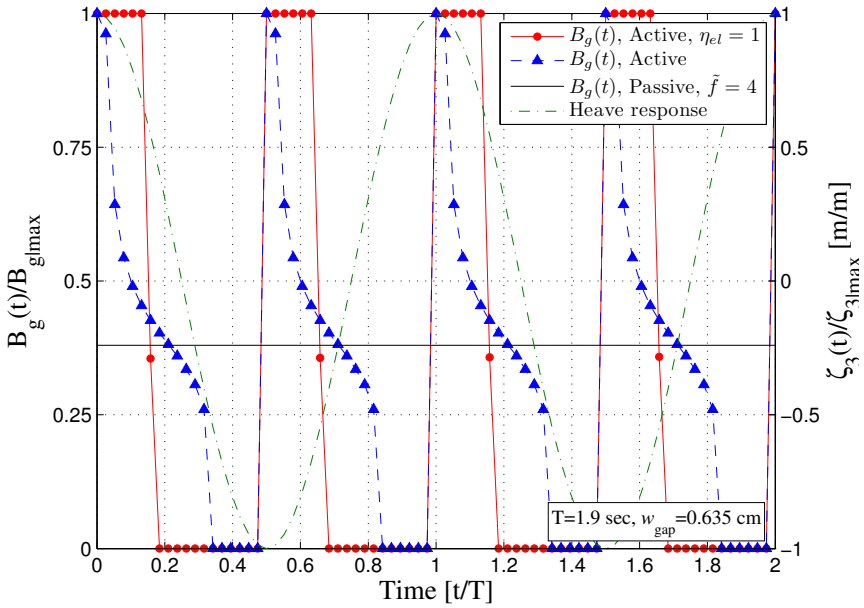

Figure 5.18: Normalized generator damping behavior and heave response

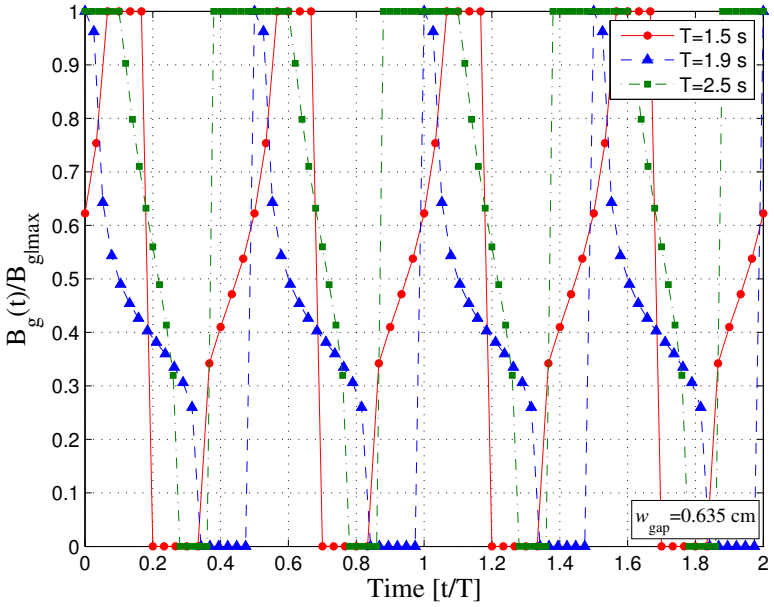

Figure 5.19: Desired generator damping profiles for different wave periods.

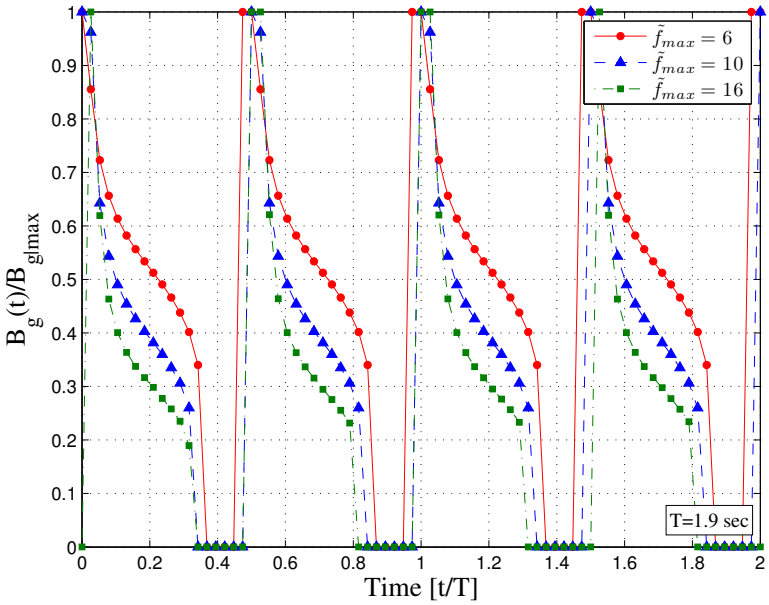

Figure 5.20: Desired generator damping profiles for different generator capacity of $B_{g|max}$

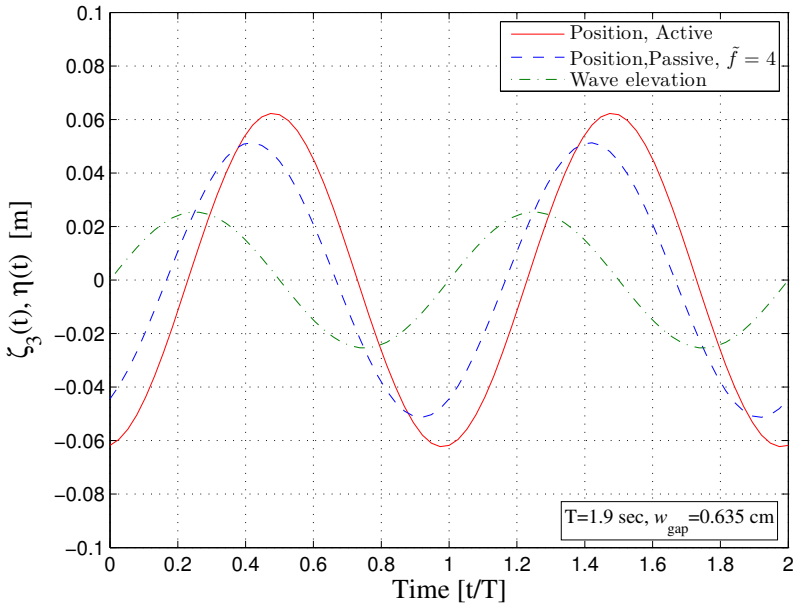

Figure 5.21: Vertical displacement of the floater and incoming wave elevation in time domain for active and passive control

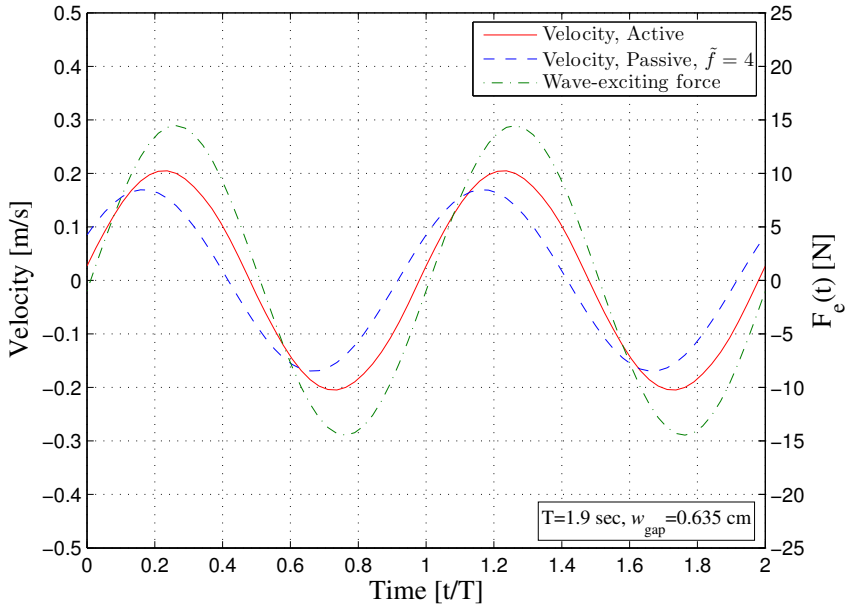

Figure 5.22: Vertical velocity of the floater and wave-exciting force comparison in time domain for active and passive control

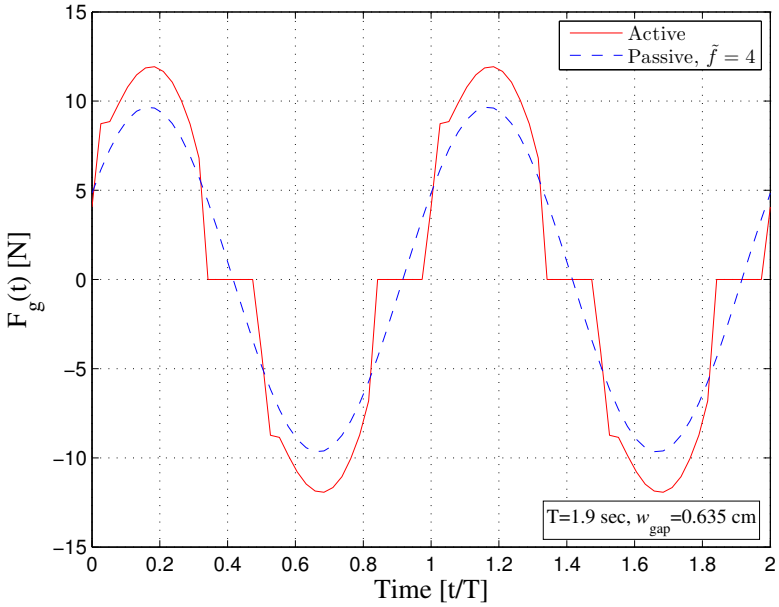

Figure 5.23: Generator force comparison in time domain for active and passive control

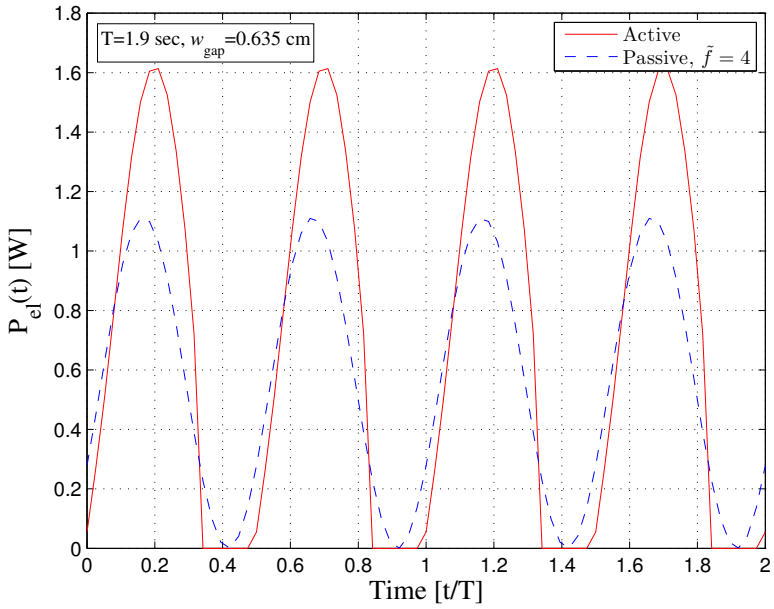

Figure 5.24: Instantaneous electrical power output comparison for active and passive control $P_{el}(t)$

5.6.1 Irregular-Wave Description

Statistically irregular waves can be modeled using superposition of a large number of regular waves under the linear theory:

$$\eta(t) = \sum_{j=1}^{N} A(\sigma_j) \sin(\sigma_j t + \epsilon_j) \tag{5.18}$$

where $A(\sigma_j)$ and ϵ_j are the wave amplitude and random phase angle between 0 and 2π of the j-th component. The wave amplitude $A(\sigma_j)$ can be expressed by a irregular wave spectrum:

$$A(\sigma_j) = \sqrt{2S(\sigma_j)\Delta\sigma} \tag{5.19}$$

where $\Delta\sigma$ is a constant frequency differences of successive waves. For irregular wave spectrum for fully developed sea, a modified Pierson-Moskowitz spectrum recommended by ISSC [72] was used:

$$S(\sigma) = H_s^2 T_1 \frac{0.11}{2\pi} \left(\frac{\sigma T_1}{2\pi}\right)^{-5} \exp\left[-0.44\left(\frac{\sigma T_1}{2\pi}\right)^{-4}\right] \tag{5.20}$$

where H_s is the significant wave height defined as mean wave height of the highest third of waves and T_1 is the mean wave period defined as

$$T_1 = 0.7713 T_p \tag{5.21}$$

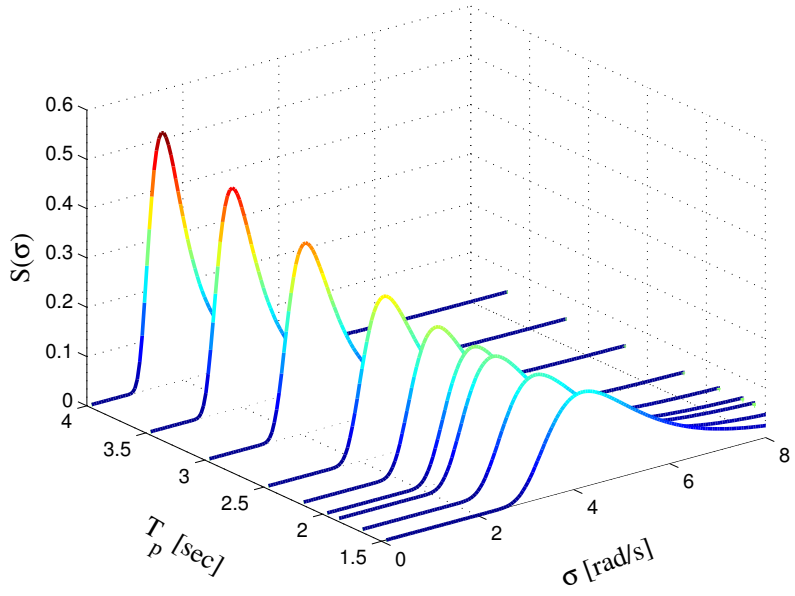

Figure 5.25: Pierson-Moskowitz spectrum for irregular waves

The wave-excitation force for irregular waves can then be constructed from the sum of wave component times frequency dependent force amplitude:

$$F^{exc}(t) = \sum_{j=1}^{N} |X_3(\sigma_j)| A(\sigma_j) \sin(\sigma_j t + \delta + \epsilon_j) \tag{5.22}$$

The irregular-wave profile of 10 minutes for the current model-scale work was constructed from frequency components between 0.1 rad/s and 8.75 rad/s spaced at 0.05 rad/s for 7.62 cm (3 in.) of H_s, while NMPC simulation was carried out for 5 minutes. Figure 5.25 shows the wave spectrum for given peak period and frequency range.

5.6.2 Irregular-Wave Results

Figure 5.26 shows the time-averaged electrical power output for 5 minutes as a function of peak period T_p for different control strategies:

(a) active control without η_{el} in NMPC objective function

(b) active control considering η_{el} in NMPC objective function

(c) passive control with $\tilde{f} = 10$ that is a maximum allowable damping at w_{gap}=0.635 cm

(d) passive control with optimal damping value at each T_p that makes maximization of P_{el}, listed in Table 5.2

By tuning the generator damping to have optimal value for different peak periods, but to remain constant over the time as case(d), the peak of time-averaged electrical power is increased by 40% when compared to the passive control case(c), which is maintaining one value regardless of wave periods. However, similar to the analysis for regular waves, active control outperforms passive control. For example, when case(b) and case(d) are compared, active control increases peak of P_{el} by 37%. Furthermore, in case(b), adding the actual conversion efficiency of the PMLG in the control process yields better electrical energy extraction than what was yielded in case(a), which showed approximately 10% increase at T_p=2.2 sec. It is also observed that peak value of P_{el} shifts towards higher T_p compared to the target resonance period of the system.

The time domain results at the given T_p=2.2 sec for case(b) and case(d) are shown in Figs. 5.27-5.29. For T_p=2.2 sec, the optimal constant damping that maximizes the electrical power output is $\tilde{f} = 4.5$. It is determined by performing the passive control simulation by sweeping the B_g. An increased motion response is achieved using NMPC with a strongly time-dependent $B_g(t)$ profile. The suggested $B_g(t)$ profile that has intermediate values between the maximum and zero is consistent with the regular wave when the actual power-conversion efficiency is considered. This time-varying damping leads to the enhanced, but discontinuous generator dynamics, as shown in Fig. 5.29.

5.7 Summary Remarks

This chapter has presented a constrained nonlinear model predictive control for the coaxial-cylinder WEC. At first, a time-domain model of integro-differential equation has been constructed and formulated in state-space form. A reduced model for radiation states has simplified the overall dynamic model and reduced the computational cost.

The optimal control problem of the heaving floater has been described in detail. Both the floater motion and PTO damping capacity constraints were considered. In addition, the power conversion efficiency of the PMLG has been added in the control scheme in order to maximize useful electrical power output. As revealed by NMPC simulation under constraints, strongly time-dependent and discontinuous PTO damping behavior is suggested in order to achieve maximum energy extraction. The conversion efficiency of the PMLG significantly

Table 5.2: Optimal constant generator damping values to maximize P_{el} for irregular waves

T_p [sec]	1.5	1.7	1.9	2.0	2.2	2.5	3.0	3.5	4.0
$\tilde{f} = B_g/\lambda_T$	3.7	3.9	4.1	4.2	4.5	5.0	5.8	7.0	7.7

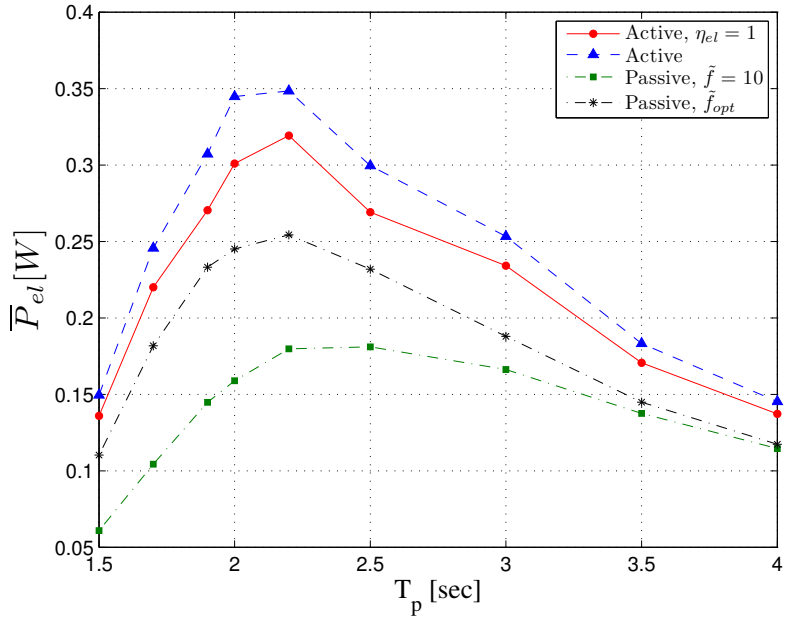

Figure 5.26: Time-averaged electrical power output for active and passive control for irregular waves

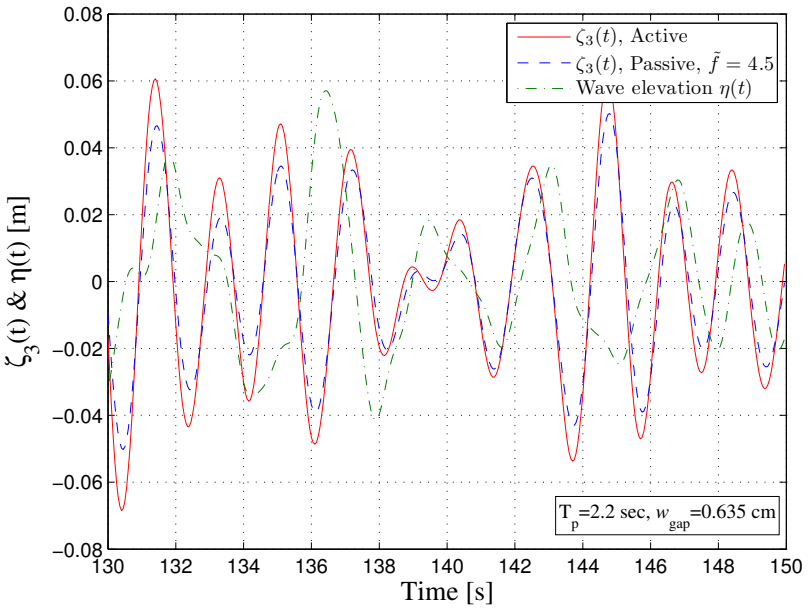

Figure 5.27: Vertical displacement comparison of the floater and irregular incident wave elevation

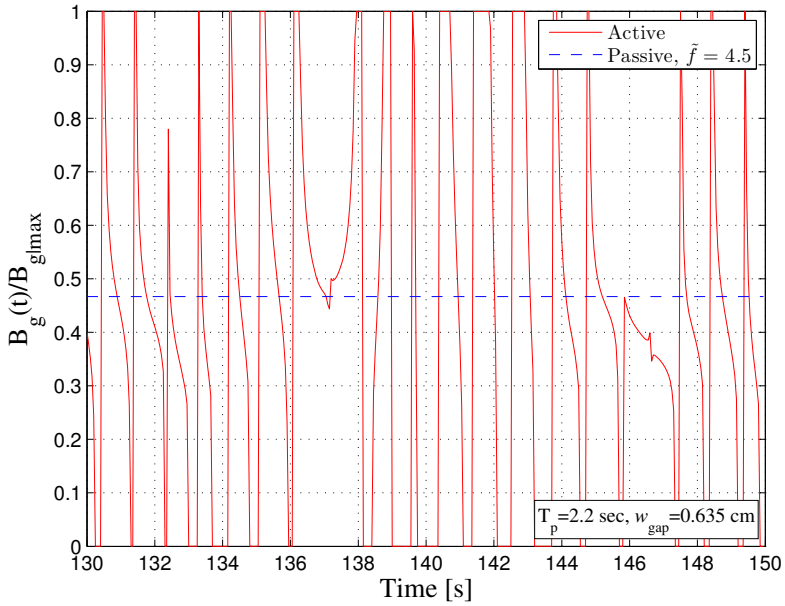

Figure 5.28: Normalized generator damping behavior comparison for active and passive control in irregular waves

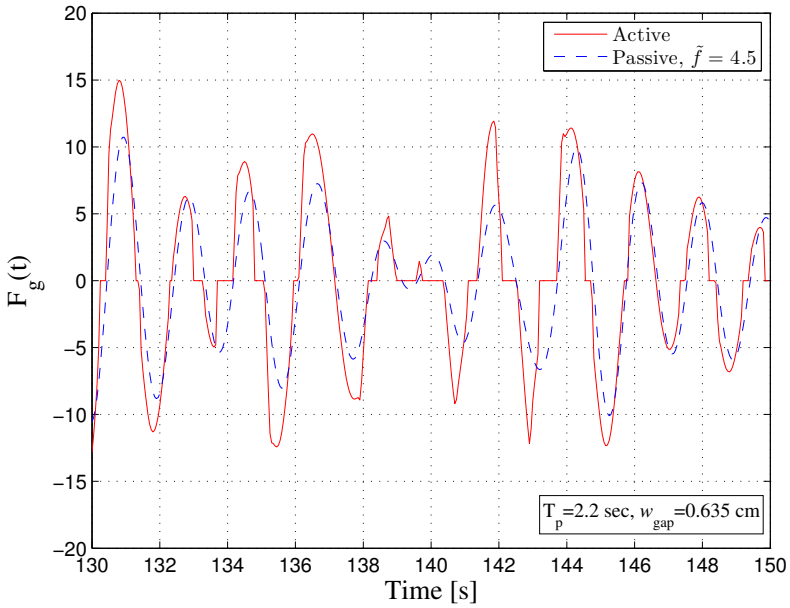

Figure 5.29: Instantaneous generator force comparison for active and passive control in irregular waves

affects the performances of the WEC system and the optimal PMLG damping time profile. The results, including the actual conversion effciency, require an intermediate level of PMLG damping, which is still within the allowable range.

Active control, in either a regular or irregular wave, significantly increases electrical power output when compared with passive control, which is constant damping. Both peak capture width and bandwidth are increased. Furthermore, a higher upper boundary for PMLG damping led to a further increase in energy extraction, especially at lower frequencies.

Chapter 6

Experimental Implementation and Verification of NMPC Control

The simulation algorithm in the previous chapter showed the effectiveness of the NMPC extraction for the dual coaxial-cylinder WEC in the presence of a PMLG but under a constrained motion and PMLG damping condition. The solution provides guidance for controller design and fabrication, to be followed by experimental validations. This chapter focuses on controlling the linear generator physically to have a system with variable damping function. The controller is designed so as to follow suggested generator damping time profile. The experimental results of WEC system so controlled are compared with the simulation data, as well as those results from passive control. The performance in regular and irregular waves are considered in sequence.

6.1 Controller for Damping Control of PMLG

6.1.1 Hardware Controller and Software Setup

Recall that the PMLG damping value B_g is driven by a combination of the applied load resistance R and magnet-coil gap width w_{gap}, which an empirical fit is given by Eqn. (3.7). In fact, to achieve a specific controller for the PMLG, controlling the load resistance would be much more preferable to controlling the magnet-coil gap width because varying the latter demands very strong reaction force within a complex structure that was designed to withstand mutually attractive force between the magnets and coils. However, to control the load resistance R, if an additional actuator or external active element is taken to manipulate the variable load resistor, reversed energy flow to the system occurs, which is undesirable in this design. This was pointed out in [58].

For this reason, a solid-state relay (SSR) was used with a pulse-width modulation (PWM) technique for controller materialization. The SSR is an electric switch between the source and the load when a low external voltage is applied to its control terminals. One of its advantages is that it can switch much faster than an electro-mechanical relay (EMR) because it contains no moving parts. EMR was used in [58] for bang-bang control. To adjust the SSR artificially to a specific fast rate, the pulse-width modulation (PWM) technique was employed. The PWM is a modulation technique for creating a constant pulses of ON for a certain time interval within a given period, called the duty cycle. By setting the duty cycle between 0% (OFF mode) and 100% (ON mode), the electrical current delivered to the electrical load from the PMLG within a certain period is thus varied. In a way, this effect is similar to achieving

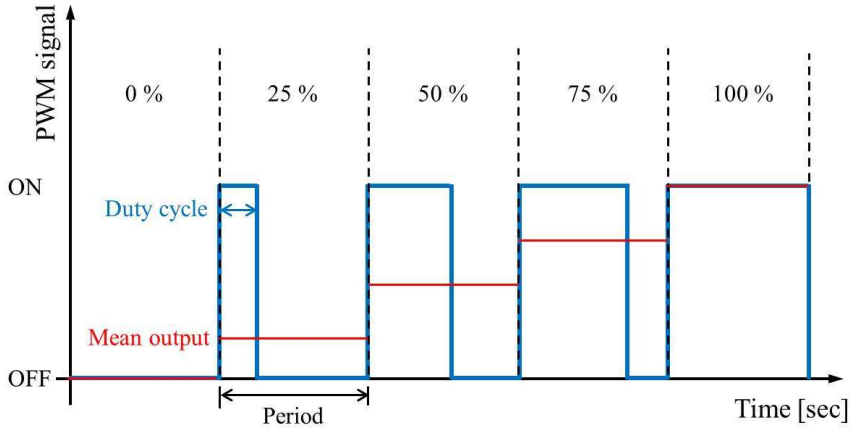

Figure 6.1: Principle of pulse-width modulation technique

analog load-control with a digital input. Figure 6.1 illustrates the working principle of the PWM. Hence, the SSR with PWM technique provides load resistance control without any external mechanical actuating element, a superior property of the design.

To generate the PWM signal, an Arduino Mega 2560 microcontroller platform was used, which can control and interact with other devices as well. For programming the microcontroller, the Arduino provides an integrated development environment (IDE) supporting C/C++ languages to organize code. The Arduino measures 2 milliseconds PWM time period, or 500 Hz frequency, which is enough for the current damping control at each time, 50 milliseconds. The Arduino scales the PWM signal from 0 to 255 such that 127 is a 50% duty cycle and 255 is a 100% duty cycle (always ON) [73].

The oscillating motion of the PMLG with the floater generates an AC voltage source, but this generated voltages are low and below 10 Volts, in a lab-scale model. Actually, the SSR for AC switching requires a high operating voltage source, approximately 110V and above. If operating voltage is under the minimum range of a SSR, the SSR will not work. If one considers the operating voltage of the current PMLG system, an AC SSR cannot be applied. Instead, a DC SSR can be applied after rectifying the AC source, by connecting the full-wave bridge rectifier using 6 diodes to the 3-phases of the PMLG. The overall schematic of controller wiring and circuit are illustrated in Fig. 6.2, and the experimental setup can be found in Fig. 6.3. Details of the controller hardware are also listed in Table 6.1.

Ideally, a diode used for rectification passes current in one direction only when voltage across the diode is greater than zero. As long as the negative voltage is charged in diode, it acts like a open circuit or just OFF mode. Actual behavior of diode, however, consumes small amount of power when conducting the forward current. It is because the P-N junction of the diode must be collapsed for current to go through by the applied voltage, which manifests about 0.7 Volts drop for silicon diode. Even though this voltage drop may not be neglected compared to the generated power from the PMLG, the loss from the use of diode did not

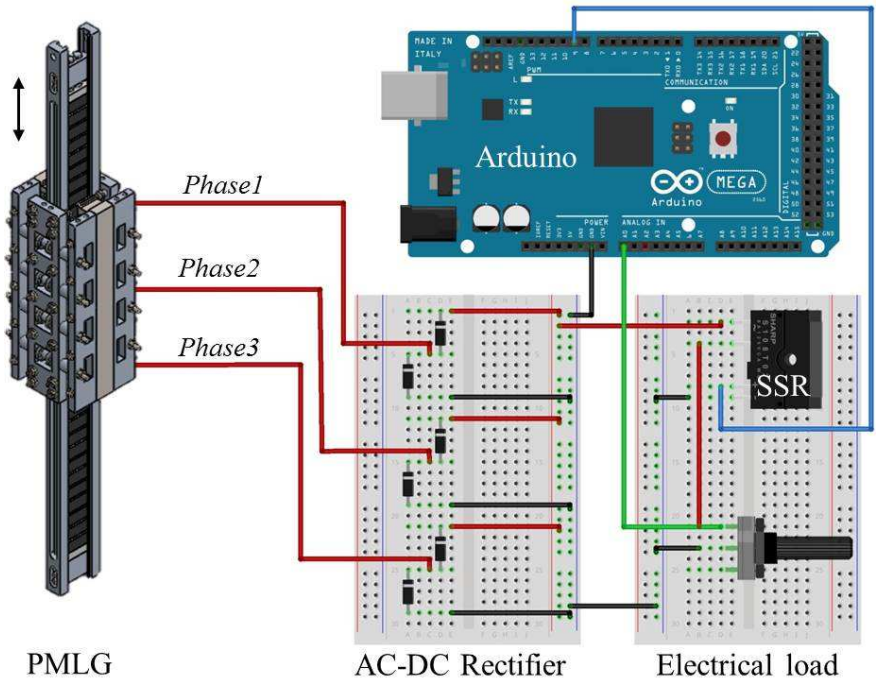

(a) Wiring for controller

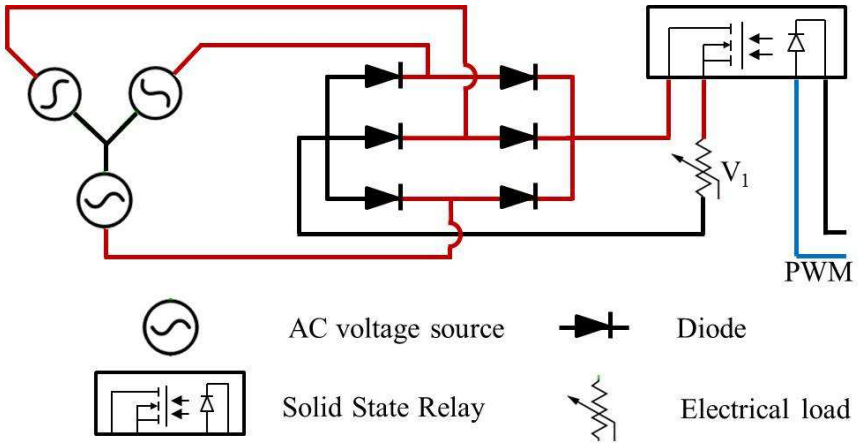

(b) Circuit for controller

Figure 6.2: Schematic of controller wiring and circuit

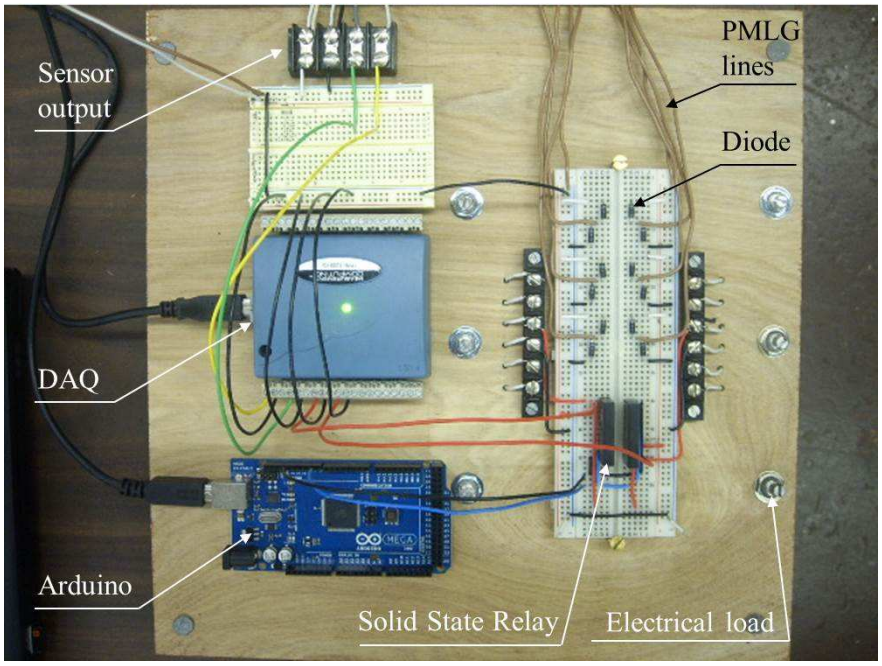

Figure 6.3: Constructed physical controller

count toward the overall power conversion efficiency of the generator η_{el} in this study.

6.1.2 Dry-Bench Test of the Controller

The dry-bench tests, described in details of bench-test instrumentation Section 3.2, were conducted to investigate the developed controller's capability for the PMLG damping control. During the experiments, the applied load resistance is set as 2 Ω, at which yields a maximum damping value $\tilde{f} = B_{g|max}/\lambda_T = 10$ at a given magnet-coil gap width w_{gap} of 0.635 cm. First,

Table 6.1: Controller hardware constitution

Microcontroller	Arduino Mega 2560
	16 analog inputs, 15 PWM outputs
Rectifier	3-phases full-wave bridge rectifier
	6 silicon diodes
Solid-State Relay	Crydom CN024D05 [74]
	0-24 VDC operating voltage, 3-12 VDC control voltage

rectified source after passing the full-wave bridge rectifier was confirmed. The alternating 3-phases PMLG voltage output and its rectified voltage output are shown in Fig. 6.4. The rectified signal is deemed to be satisfactory for using the DC-SSR, though the voltage drop due to the loss by diodes is observed after the rectification.

Next, the effect of the PWM duty cycle on the SSR performance was investigated. Figure 6.5 shows the measured voltage output at the applied load resistor with different PWM duty cycles. As an example, one oscillating cycle is shown for T=2.5 sec. This result demonstrates that the SSR acts as a variable switch controlled by the PWM duty cycle. As the PWM duty cycle is reduced to 92% and 50% from 100% (always ON mode), the time-averaged voltage output is decreased by 47% and 90%, respectively. It also can be seen in Fig. 6.5 that the voltage output contains high frequency components with decreasing the duty cycle. This is because the SSR has a fast ON-OFF mode changes within the time period, according to the PWM duty cycle.

Finally, in order to adjust the PMLG damping value B_g within its physical capacity, the corresponding PWM duty cycle needs to be quantified between 0% (OFF) and 100% (ON). For a given gap width of w_{gap}=0.635 cm, the PMLG damping values obtained for different PWM duty cycles at the resonance frequency are plotted in Fig. 6.6. The following exponential expression was used to represent the empirical damping behavior of the PMLG:

$$B_g = Ae^{B\cdot\mathrm{PWM}} + C \tag{6.1}$$

where A=0.05, B=8.1, and C=5. This empirical fit will be then used to adjust the generator damping value by manipulating the PWM duty cycle. Even in OFF mode, representing open circuit (0% duty cycle), a small generator damping value was detected. However, it is only related to the residual damping from cogging and friction losses; therefore, no power generation is observed.

6.2 Results for Wave-Tank Tests in Regular Waves

6.2.1 Frequency-Domain Results

The Arduino was programmed to tune the SSR by feeding a proper PWM input, so that the PMLG can have the desired damping value, with monitoring the floater position at the same time.

A compilation of the results in the frequency domain for active and passive control strategies can be found in Fig. 6.7 through Fig. 6.9. For the purpose of comparing different control strategies, four different cases (labeled as (a) to (d) below) were selected for consideration:

(a) Active control with ideal PTO efficiency, i.e., $\eta_{el} = 1$, implying that the absorbed power P_{me} is maximized, which led to the bang-bang control sequence shown in Fig. 5.17(a).

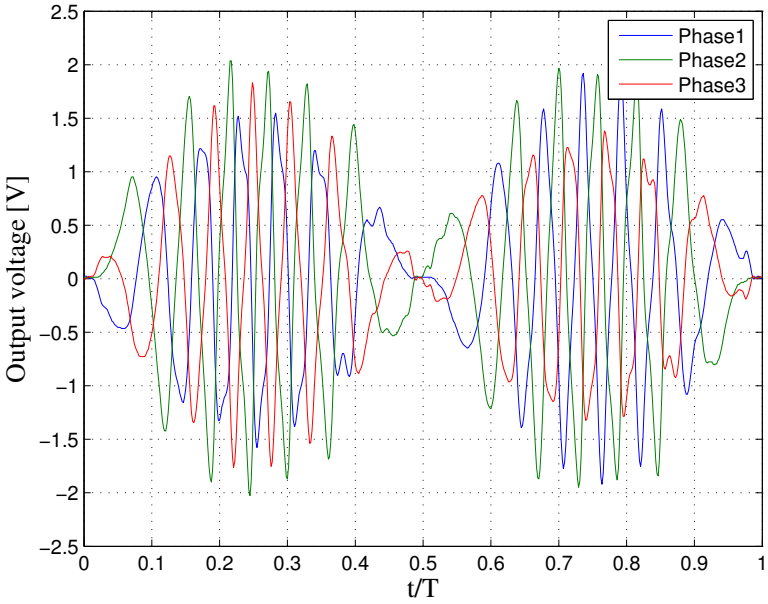

(a) 3-phase voltage output

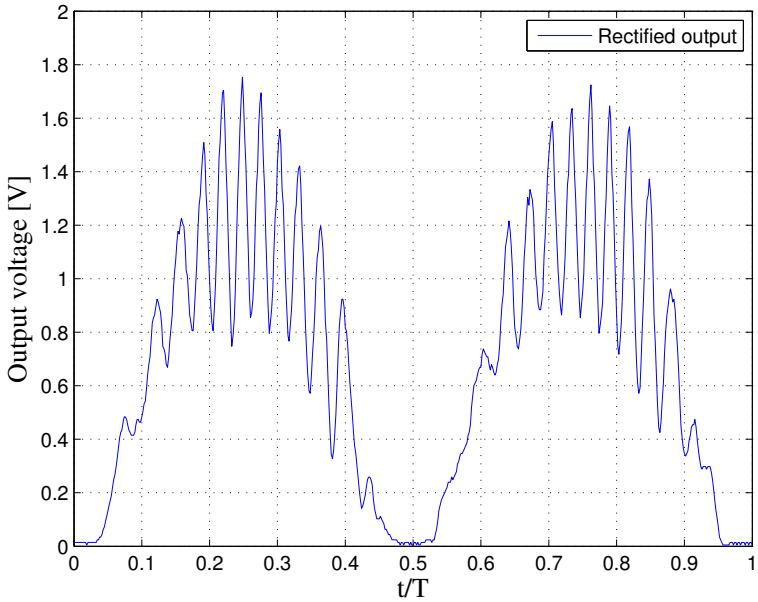

(b) Rectified voltage output

Figure 6.4: Voltage output before and after 3-phases bridge rectifier

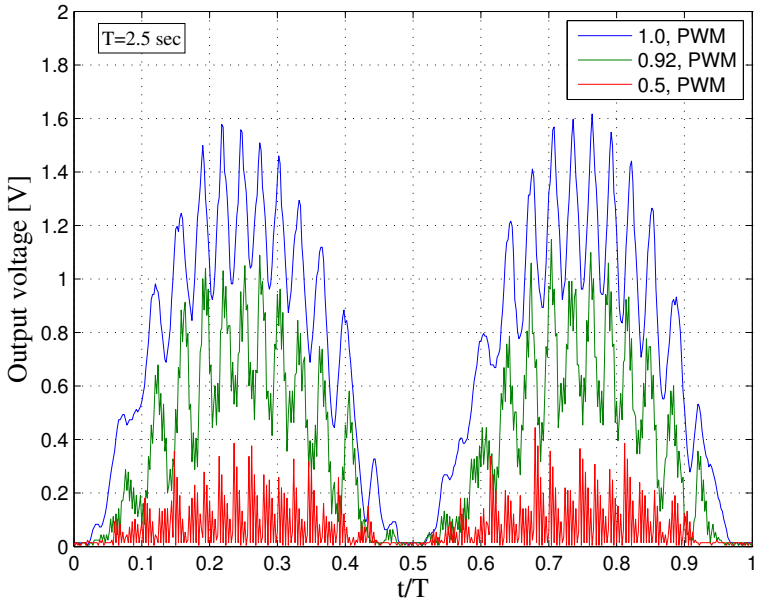

Figure 6.5: Voltage output for different PWM duty cycle

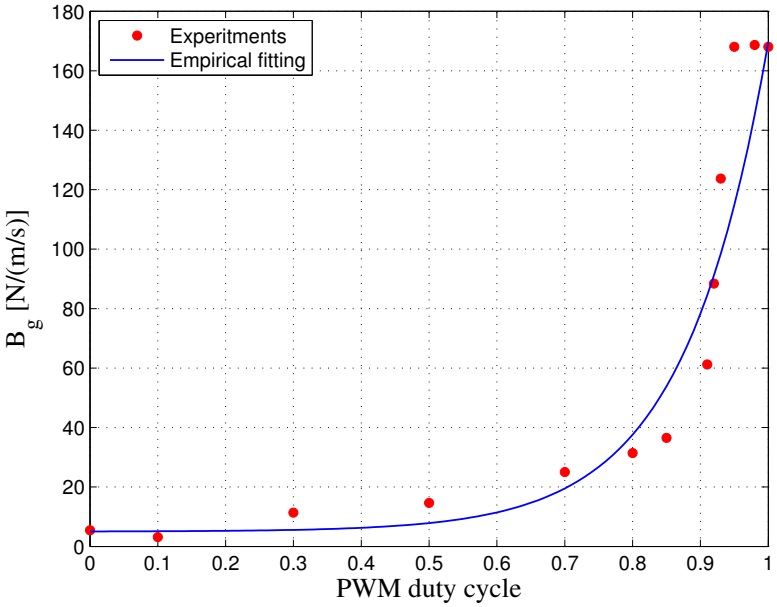

Figure 6.6: PMLG damping value control by the PWM duty cycle

(b) Active control with actual (physical) efficiency of the PMLG that maximizes the useful power output P_{el} by considering actual η_{el} in objective function, which led to the time-dependent control sequence shown in Fig. 5.17(b).

(c) Passive control with $\tilde{f} = 10$, at which the PMLG has a maximum allowable damping ($B_g = B_{g|max}$) at given w_{gap}=0.635 cm, corresponding to 100% of PWM duty cycle.

(d) Passive control with $\tilde{f} = 5$, at which power-conversion efficiency of PMLG has maximum, corresponding to 90% of PWM duty cycle.

Again, the desired constant and continuous PMLG damping $\tilde{f} = B_g/\lambda_T$ for case(c) and (d) determines value of the constant PWM duty cycle from the empirical expression, given in Eqn. (6.1).

For the overall performance of regular wave with different time period, Fig. 6.7 shows the heave RAO of the floater as a function of the non-dimensional frequency using different control strategies. Here, two cases of active damping control case(a) and (b) can be found in the upper plot of Fig. 6.7. The red markers are for case(a), which correspond to a bang-bang type control sequence, and the blue ones are for case(b), where the actual η_{el} was considered. In addition, we use the notation that the solid and hollowed symbols represent the measured data from the model test and the predictions from the simulation, respectively. It is observed that the peak value of heave RAO for case(a) is two-times higher than that of case(b), since case(b) has a longer activated duration of the PMLG causing the generator force, which restrains the motion response.

The experimental results agree very well with the simulation predictions. This confirms again that combination of the SSR and the PWM techniques can be useful for achieving load control, instead of mechanical actuator devices such as a motor to directly change variable resistor. The discrepancy between measured and predicted data occurred for case(a) in the range of frequency between 0.55 and 0.6 is because B_g was strongly restricted to the bang-bang sequence during experiments, even though simulation gives a few transient values for a short time. The lower figure shows the results of the passive control strategy for case(c) and (d) with the use of a constant and continuous damping value; the measurements also show good agreements with simulation.

The overall results of non-dimensional capture width $\overline{C}_w$, representing the energy absorption by the WEC, for different control strategies can be found in Figure 6.8. For all control strategies, experimental measurements match well with the predictions. As predicted, the active control mode results in a better performance since it increases the $\overline{C}_w$ for all frequencies. In the passive control strategy, on the other hand, the peak value of $\overline{C}_w$ can be increased by a decreased damping value B_g but the bandwidth would be narrowed. Between the two active control strategies, case(a) outperforms case(b) because the NMPC algorithm of case(a) targeted the maximum energy absorption.

The results of non-dimensional effective capture width $\overline{C}_{w|out}$, representing the useful electrical power output, are provided in Fig. 6.9. It should be noted again that the results

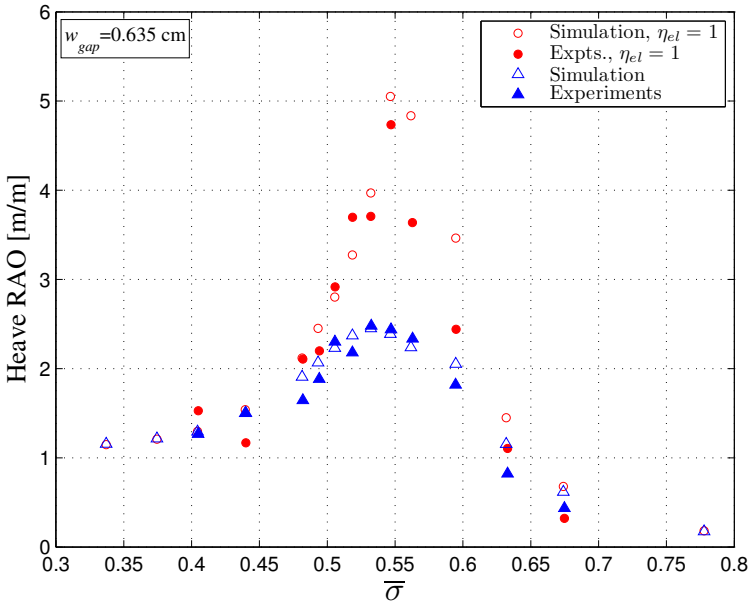

(a) Active control

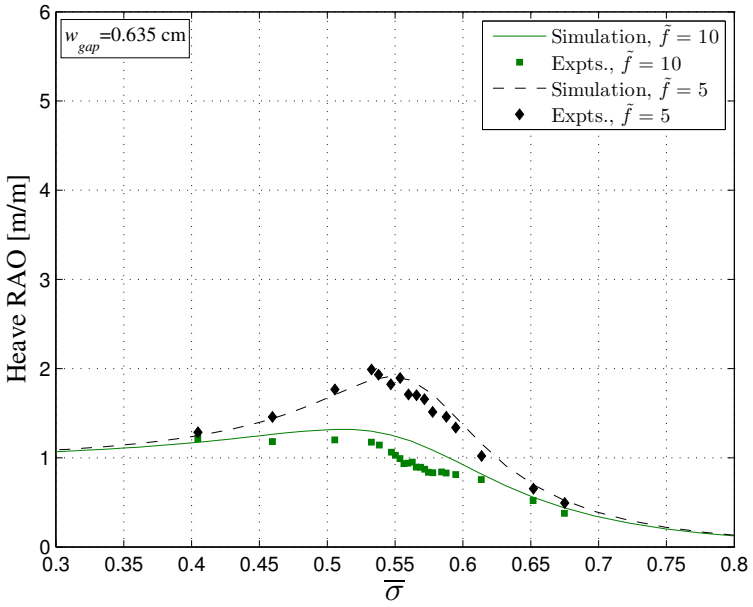

(b) Passive control

Figure 6.7: Comparison of simulations and experimental results of the heave RAO for different control modes

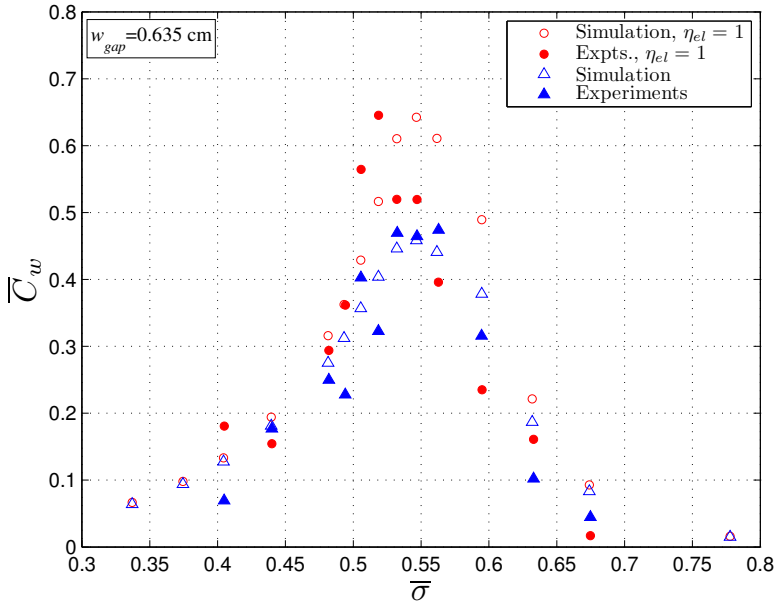

(a) Active control

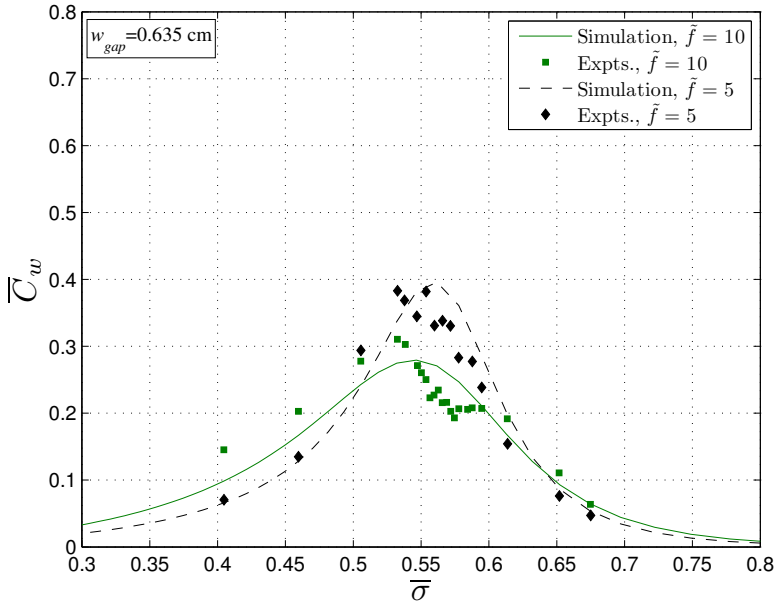

(b) Passive control

Figure 6.8: Comparison of simulations and experimental results of the capture width for different control modes

for case(a) is computed by multiplying the actual η_{el} to the $\overline{C}_w$ results. For all control strategies, predictions from numerical simulations were validated by the measurements. For the active control, after the actual efficiency of the PMLG was included, the performance of case(b) is comparable or greater than that of case(a). It is consistent with the simulation and expectations.

Thus, in real-world operations, case(b) would be superior because it produces more energy output with a smaller motion response of the WEC. Moreover, the results of passive control alternatively show that case(c) has a lower conversion efficiency than case(d) from the results of $\overline{C}_w$. Therefore, actual efficiency module of the PTO plays an important role in determining the electrical power extraction.

6.2.2 Time-Domain Results

Time-series data of the active control were also recorded. Figure 6.10 shows the motion of the floater with the active and passive control of PMLG respectively, as an example of T=1.9 sec. The first four cycles show the motion response of active-controlled system, and the rest of the cycles are under the passive control. The PWM input signal, or duty cycle, represents active or passive control mode. In the active control mode, the PWM input has varying duty cycle at each time step according to the desired PMLG damping value. In the passive control mode, however, the PWM input is a constant value (100%) meaning that it retains the constant generator damping value $B_{g|max}$ over time. When the control mode is changed from active to passive, the floater motion decreases and reaches the steady state after a few cycles of transition. The motion amplitude of the active-controlled system is approximately two-times greater than that of the uncontrolled system. In addition, the instantaneous electrical power output for active and passive control is shown in Fig. 6.11. The maximum value and time-averaged value of the electrical power output with the active control is improved by approximately factor of two.

It should be aware of that increasing motion response of the floater does not directly yield a higher energy output because the active control reduces the actual operational time of the PMLG to generate power. Thus, a correct activation timing of the PMLG is important for making use of the active control. The PMLG should be activated when the floater is at high velocity. Therefore, the current work synchronized the PWM control signal with the measured floater displacement to minimize an error from incorrect triggering of the PWM.

6.3 Results for Wave-Tank Tests in Irregular Waves

For the regular waves, implementation of the NMPC achieved success with regards to maximizing power extraction. The NMPC simulation was also performed for irregular waves, but tests in wave-tank were conducted for certain conditions. The incident wave follows the modified Pierson-Moskowitz spectrum, given in Eqn. 5.20, with the significant wave height H_s of 0.1 m and the running time of 1 minute in this model-scale experiment.

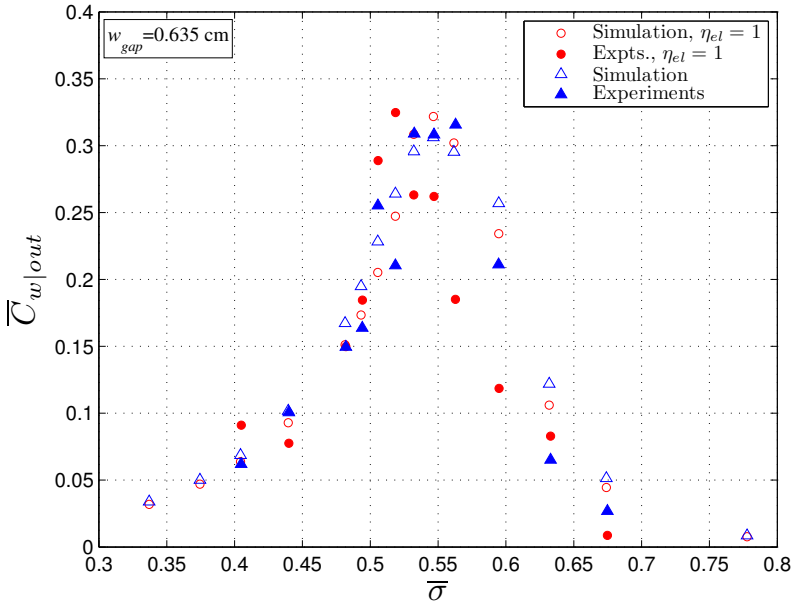

(a) Active control

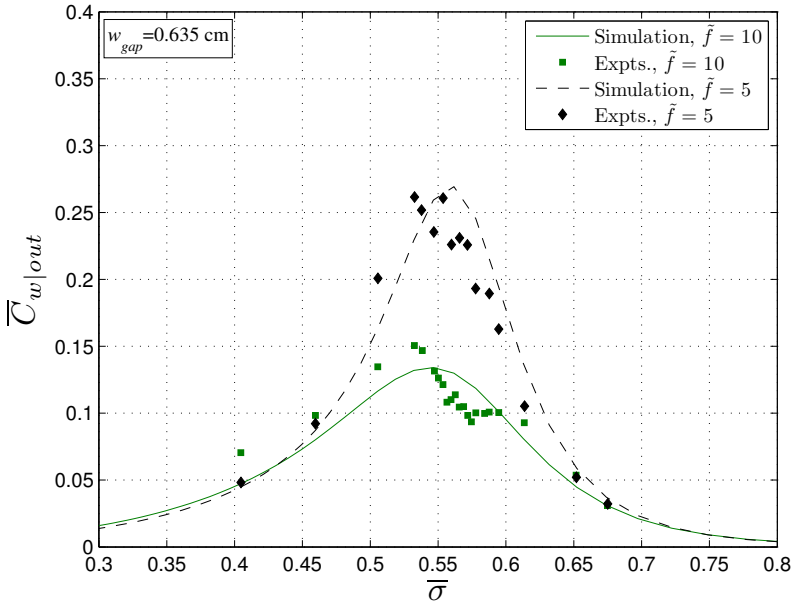

(b) Passive control

Figure 6.9: Comparison of simulations and experimental results of the effective capture width for different control modes

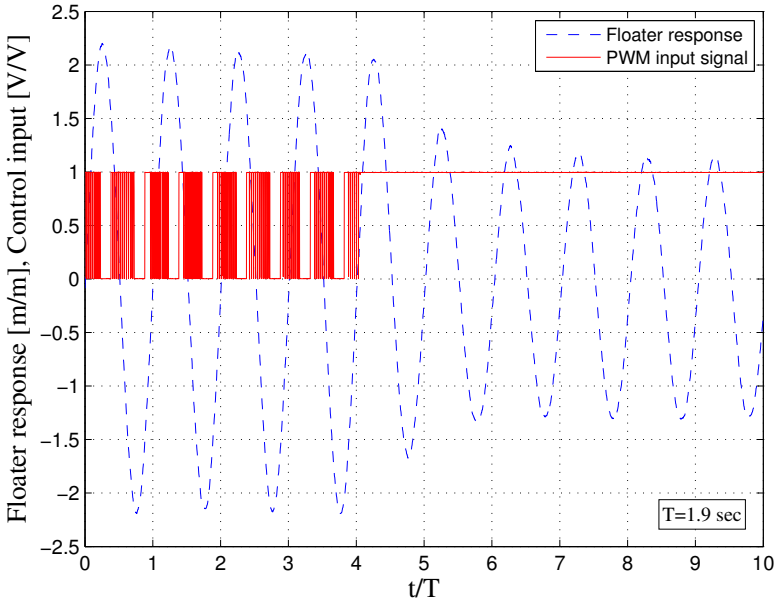

Figure 6.10: Transition of motion response from active control to passive control

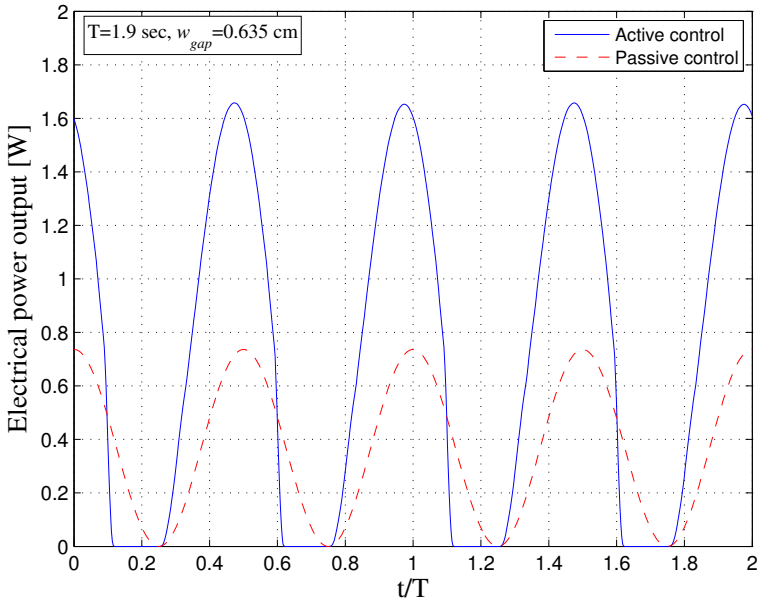

Figure 6.11: Instantaneous electrical power output for different control modes

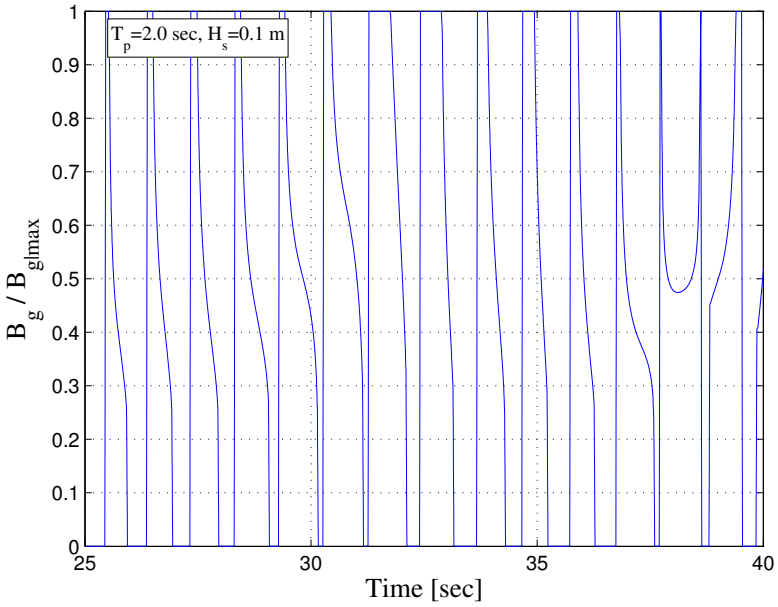

Figure 6.12: Suggested generator damping profile for irregular waves

The simulation of NMPC determines the time series of the optimal generator damping values that maximizes electrical power output. An example of such a generator damping profile is shown in Fig. 6.12, which can be used to decide the value of the PWM duty cycle using Eqn. (6.1). As seen in results of the regular-wave tests, the PWM duty cycle includes intermediate values at each time step. A measured motion response and velocity, as a results of the PMLG damping control, are compared to that of passive control with $B_g = B_{g|max}$ in Figs. 6.13 and 6.14. This improvement by using NMPC strategy is evident. Interestingly, the recorded time history between 35 and 40 seconds shows that the active control leads to a larger oscillation of the floater. This indicates that the WEC system may extract more power from waves, even though the PTO is not continuously activated.

Furthermore, the instantaneous wave-exciting force, generator force and electrical power output are shown in Figs. 6.15 and 6.16, for both active and passive control strategies. Since the incident-wave information is given in this study, the wave-exciting force is obtained from Eqn. (5.22). It is clear that for the actively controlled system, the amplitude of motion response increases along with electrical power output, discontinuous generator force is yielded though.

As a summary of the overall measured response and yield in irregular waves, the time-averaged electrical power output for different peak period T_p can be found in Fig. 6.17. The active control applied on the PMLG damping yields overall enhanced power extraction over the tests at given T_p, which is about 25% greater at T_p=2.2 sec than the energy extracted by the passive control mode.

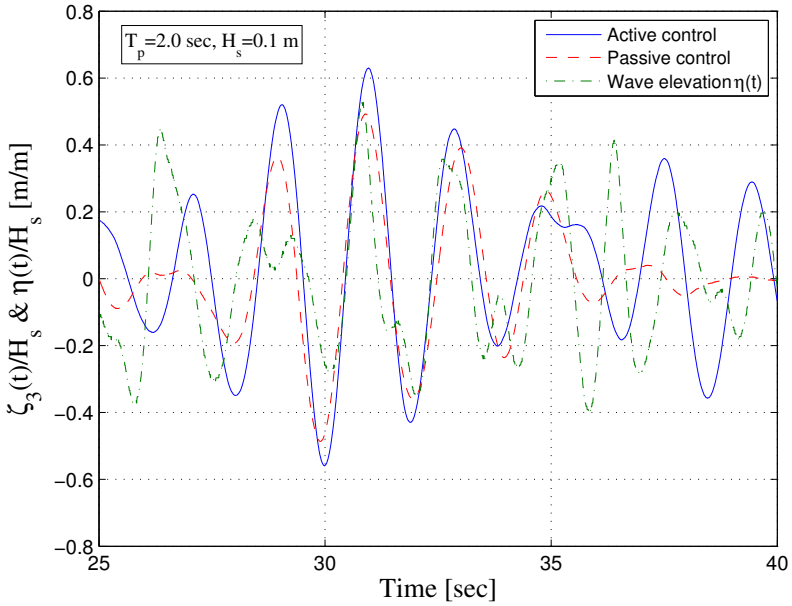

Figure 6.13: Time histories of the heave displacement for active and passive control in irregular waves

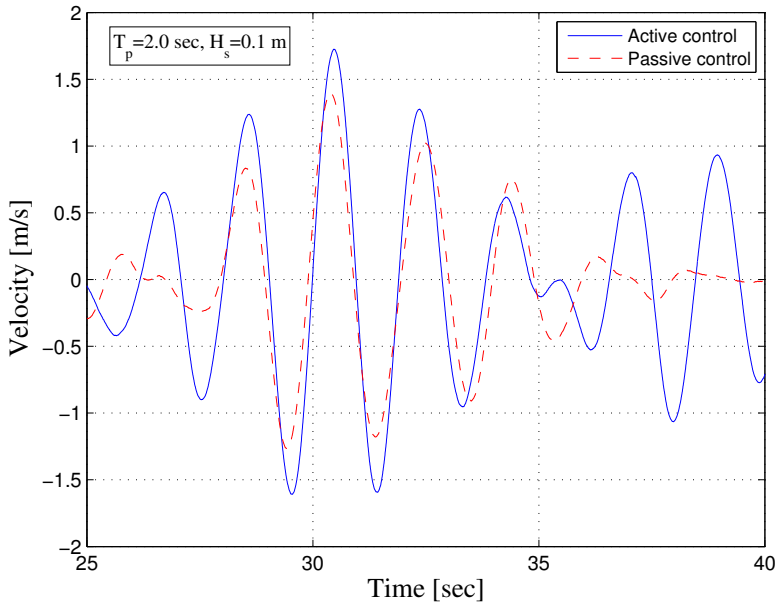

Figure 6.14: Time histories of the heave velocity for active and passive control in irregular waves

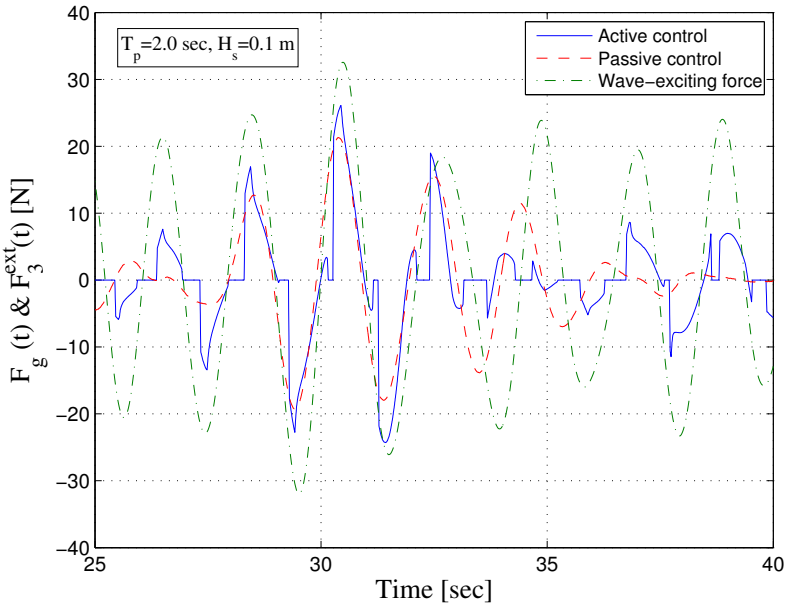

Figure 6.15: Time histories of the generator force for active and passive control and wave-exciting force in irregular waves

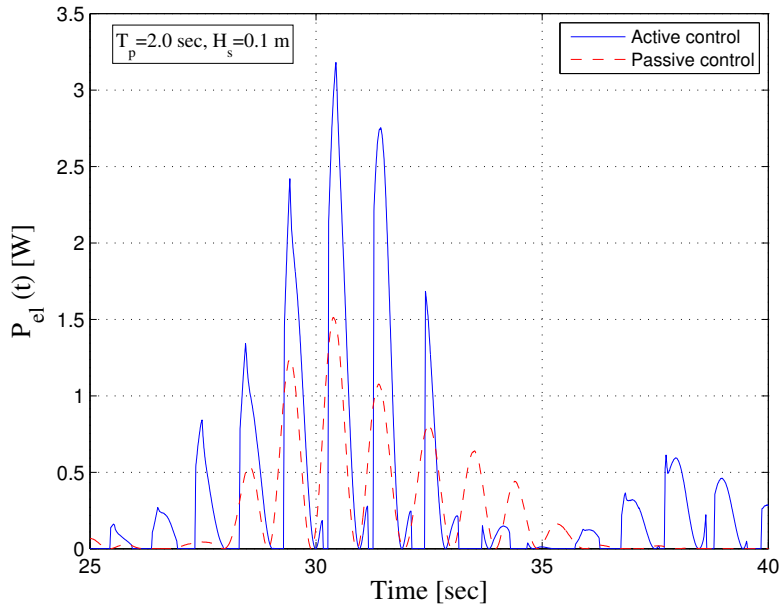

Figure 6.16: Instantaneous electrical power output for active and passive control in irregular waves

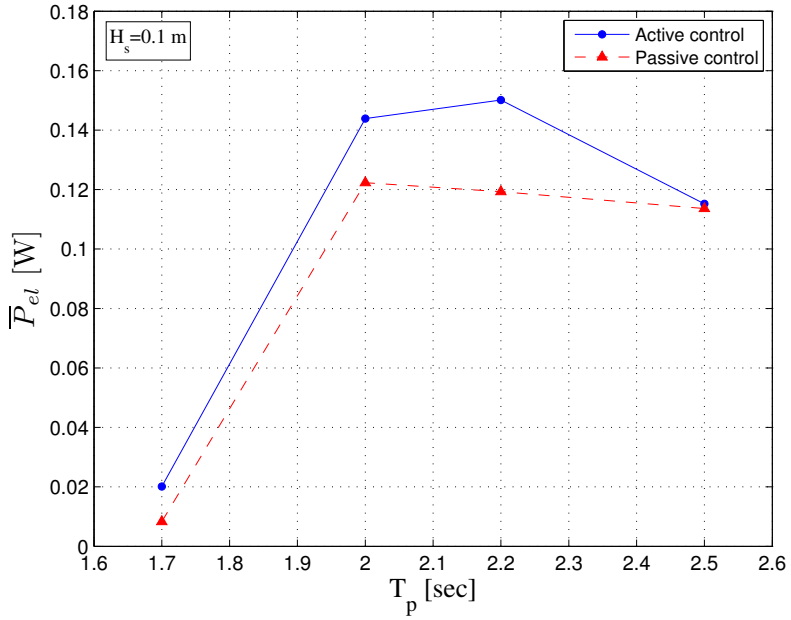

Figure 6.17: Time-averaged electrical power output for different control modes in irregular waves

6.4 Summary Remarks

This chapter has presented the experimental implementation of the optimal damping control for a fully coupled WEC system. As a direct consequence of the simulation, a controller was required to change the generator damping over time, which includes an intermediate damping value within an allowable damping capacity. This implementation of the NMPC into the WEC was realized by using a solid-state relay and a pulse-width modulation technique applied onto controlling the load resistor, using an intrinsic relation between the PMLG damping B_g and load resistance R. The SSR behaves like an analog switch that changes the generator damping, which is controlled by the duty cycle of pulse width. By means of the developed controller, PMLG damping could be adjusted to follow the desired optimal value at each time step quickly, without an additional energy input to the PTO system.

The controller so deployed on the WEC system has been experimentally examined in regular and irregular waves. The WEC performances have been compared to the simulation results for different control strategies: active control with the ideal or actual conversion efficiency of the PMLG, and also passive control. The actively controlled WEC outperformed, as expected, the passive controlled system by increasing the peak value and encouragingly broadening the bandwidth of energy extraction. The measurements were in agreement with predictions, which demonstrates and verifies that the proposed control strategy is attractive for real-time implementation.

Chapter 7

Conclusions and Future Research

This dissertation covered the mathematical modeling for the optimization of a heaving wave-energy converter, consisting of a dual coaxial cylinders, so as to maximize energy extraction. It includes some design aspects of the device, control system suitable for enhancement, numerical simulation of the controlled system, and experimental validation of the predictions. In this chapter, the most important findings are emphasized and possible future research topics are addressed.

7.1 Discussion and Conclusion

A heaving point-absorber consisting of dual coaxial cylinders has been modeled mathematically to simulate its performance as an ocean-wave energy converter using primarily linear-wave theory. The mathematical modeling of the system included the coupling interaction between the hydrodynamics of the wave-energy converter (WEC) and the the permanent-magnet linear generator (PMLG), acting as the power take-off (PTO). Existing semi-analytical-based solutions [30] for modeling the hydrodynamics of the dual cylinder were utilized, together with nonlinear control theory for the PTO, to predict the interacting performance of the WEC and the PTO unit. The prediction has been validated by means of model-scale experiments of about 1:24 scale in the Model-Testing Facility at UC Berkeley Richmond Field Station. Additional correction factors attributed to viscous effects were included in the radiation damping and added mass coefficients, which had not been included in a pure potential-flow model. Experimental results of this coupled system in regular waves have confirmed the validity of the theoretical predictions and soundness of the engineering design.

The mathematical modeling provides not only the performance predictions, but also a rational and effective way for optimization of certain design and performance-related variables. The flat-bottom shape of the outer cylinder or floater was modified into a needle-like curved shape, called The Berkeley Wedge [40], per a newly patented design of the research group, so as to minimize viscous losses. This prudent change in geometry led to a three-fold increase in the floater response at resonance frequency, compared to that for the flat-bottom geometry, thus improving wave-energy capturing capability. The damping behaviors of the PMLG in the presence of an appropriate supporting structure for the dual cylinders were investigated. Furthermore, optimal operating conditions as a function of output load resistance and magnet-coil gap width for energy extraction and mechanical to electrical power-conversion efficiency were also determined. This optimized the floater bottom shape and the operating

conditions of the PMLG has led to a two-fold increase in overall efficiency for useful energy extraction at resonance frequency, even without any active control strategy.

The continuous research on maximizing or improving energy extraction at off-resonance frequencies led to a our consideration of active control strategy for the WEC system. The nonlinear model predictive control (NMPC), with constraints on the PMLG damping and the floater displacement, was applied to the coupled system, following the initial work of [60] for a single cylinder. To apply the control strategy in wave-after-wave, the floater dynamics incorporating with the PMLG has been constructed in the time domain, and then formulated in the space-state representation so that the system can be solved effectively. The control-theory optimization problem is to determine an optimal PMLG damping value as a tuning parameter. A significant departure from previous approaches for active control of the WECs is that the power-conversion efficiency of the PMLG was added in the control scheme to maximize the useful electrical power output. Simulation results for the optimal behavior of the PMLG damping function indicated a time-varying and discontinuous damping profile for both regular and irregular waves. It is considerably different from the bang-bang type control strategy that was focused on maximum energy absorption in some previous works. It has been also shown that such NMPC-controlled WEC system outperforms the passive system by increasing the peak value of capture width and broadening the bandwidth of the energy extraction in terms of incident wave frequency.

The physical implementation and verification of the simulation results are important steps to confirm the feasibility and success of this present strategy. The solution for the desired damping time-profile, as obtained from the simulation to achieve damping control, is to use a combination of solid-state relay (SSR) and pulse-width modulation (PWM) techniques. Due to the PWM signal control, the SSR acts as an analog switch device, adjusting the current flow to change the damping value of the PMLG. The effectiveness of the combination of SSR and PWM was tested, and the benefit of the NMPC strategy in terms of energy extraction was evaluated and documented. Laboratory experiments conducted have shown the successful implementation of the NMPC strategy in the WEC system with a realization of the electrical controller. In addition, it has achieved an increase in power output in both regular and irregular waves, with the activated duration decreased, when compared to that of the passive control strategy.

Point by point, this research has provided:

- A mathematical modeling for performance computations of a heaving point absorber coupled with a power take-off unit.

- An improvement of the existing model with the consideration of viscous effects and validation of theoretical predictions.

- A detailed description on methods to improve WEC performance in terms of floater design and operating conditions of the PMLG.

- A control strategy for maximizing the power extraction.

- A detailed approach on control application to the system and examination of its advantages.

7.2 Estimation of Performance Capability

It is of interest to examine the amount of power extraction anticipated when the WEC model is scaled up to a prototype. As this study focuses on energy extraction from incident waves, the WEC system being research is assumed to be properly scaled and fully integrated. As the average dimension of floater diameters for heaving devices is taken as 12 m [75], a scale fratio of 24 was considered for scaling the current WEC system from our laboratory model. Table 7.1 lists the geometric properties of the scaled-up device.

First, the full-scale prototype WEC system is able to produce approximately 300 kW peak-power output in 3 m wave height of 8.8 sec wave period, with estimated non-dimensional effective capture width of 0.32 at resonance frequency from the current model-scale experiments.

Next, the power extraction capability of the dual coaxial-cylinder system at a promising reference site as a future deployment area is estimated. The wave resource (kW per frontal meter) is strongly dependent on location, which is proportional to the wave-amplitude square and wave period. As an example, the reference site for wave-energy resource was chosen near Eureka, in Humbolt County, California. At this site, the wave-energy density of 34 kW/m is obtained from the wave statistics data in terms of joint probability distribution [76], which is shown in Fig. 7.1. Based on this wave resource, the electrical power output for the current full-scale WEC system is estimated approximately to be 130 kW, with assumption that the WEC still has an effective capture width of 0.32 relative to the floater diameter. If the PMLG PTO efficiency is better, then the electrical power output is expected to increase. When a typical house requires 20 kW per year, the solo WEC system can adequately supply for the electricity usage of six such houses.

However, a point-absorber type WEC system extracts maximum power when it operates at resonance. If the current WEC system is non-resonated, the power extraction is reduced by a factor of three, see Figs. 6.7 and 6.9, as wave energy would no longer be all concentrated at resonance. It is therefore important to design the device to closely match a resonance fre-

Table 7.1: Geometric properties of the scaled-up device, scale ratio of 1:24

Outer cylinder inside radius	[m]	3.6
Outer cylinder radius	[m]	6.1
Outer cylinder draft	[m]	20
Resonance wave period	[s]	8.8

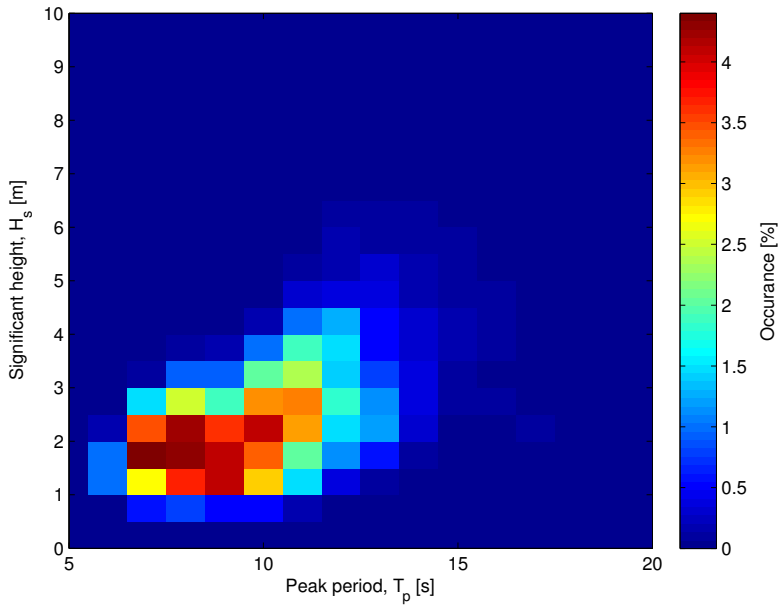

Figure 7.1: Wave statistics data for reference resource from [76]

quency with the dominant wave frequency of the deployment site. Consequently, additional efforts to widen more the performance bandwidth or to vary the resonance frequency of the system according to the incident-wave frequency would be worthwhile.

7.3 Recommendations for Future Research

Possible extensions of this project could include:

1. Improvements on the control process

The control process in this thesis does not include a prediction module for incoming waves. The current controller determined the optimal damping value with the assumption that the incident-wave information is given. However, it is required to estimate the non-causal function of the wave-exciting force for a real-time controller. In practice, wave forecasting is an essential part of the control process. Spatial measurements using radar [77] or a LIDAR [78] can make wave predictions in a real environment. Several forecasting models based on time series to predict incident waves ahead of time can be found such as deterministic wave prediction [79, 80], extended Kalman filter, auto regression model, and neural network [81, 82].

Furthermore, it would be interesting to extend the proposed control strategy to a two degrees-of-freedom system where the inner cylinder is allowed to heave. It was

found that the optimal performance is similar but the damping requirement is quite different when compared to the one degree-of-freedom [34, 35].

2. Computation of extreme loads for survivability

Designing a WEC system for survival in harsh ocean environment is essential and required for service. Therefore, a study regarding the loading, dynamic response, and stability is important for extreme sea-conditions and occasional events such as tsunamis, hurricanes, or rogue waves. Along with the need for an effective model using potential flow or CFD methods for large nonlinear waves, purposeful systematic framework must be employed for the survival aspect of WEC design [83]

3. Computation of viscous effects for different bottom shapes

In this study, the viscous factor that was added in the theoretical modeling was evaluated using the free-decay tests at resonance frequency. To provide high fidelity solution of viscous effects for a wide range of frequencies, several tests with varying resonance frequency are required. It would be challenging to change the resonance frequency while keeping inviscid hydrodynamic coefficients constant. Numerical approaches may be considered to compute the hydrodynamic coefficients with viscosity. Analytical and boundary integral methods are generally combined with empirical solutions to represent viscous effects, and hence, the Navier-Stokes equation method may be required which can be directly calculated in the solution [84]. If viscous-fluid analysis is possible, it would be useful to estimate the hydrodynamic performances of WECs directly.

4. Consideration of multiple WECs

Developing wave-farm field suggest multiple WECs, or even arrays of WEC will be deployed. As the study of a single WEC does not consider the interacting effects among the multiple WECs, a study focusing on an array of WECs is inevitable. It would be useful to study not only the interference phenomena, but also effects of design parameters, such as grid layout, spacing between WECs, and geometric properties, on the overall power extraction performances. The following step should be an implementation of the effective control strategy for multiple WECs. Works in this direction has already begun [85].

Bibliography

[1] "Intergovernmental panel on climate change 2014: Synthesis report." https://http://www.ipcc.ch/report/ar5/syr/.

[2] "Us energy information administration, international energy outlook 2011." https://www.eia.gov/forecast/aeo/index.cfm.

[3] B. Drew, A. R. Plummer, and M. N. Sahinkaya, "A review of wave energy conversion techonology," *Journal of Power and Energy*, vol. 223, pp. 887–902, 2009.

[4] K. Gunn and C. Stock-Williams, "Quantifying the global wave power resource," *Renewable Energy*, vol. 44, pp. 296–304, 2012.

[5] J. Falnes, "A review of wave-energy extraction," *Marine Structure*, vol. 20, pp. 185–201, 2007.

[6] A. Clément, P. McCullen, A. Falcão, A. Fiorentino, F. Gardner, K. Hammarlund, G. Lemonis, T. Lewis, K. Nielsen, S. Petroncini, M.-T. Pontes, P. Schild, B.-O. Sjöström, H. C. Sørensen, and T. Thorpe, "Wave energy in europe: current status and perspectives," *Renewable and Sustainable Energy Reviews*, vol. 6, pp. 405–431, 2002.

[7] C. McGowin, *Ocean tidal and wave energy - renewable energy technical assessment guide*. Electrical Power Research Institute, 2005.

[8] A. F. de O. Falcão, "Wave energy utilization: A review of the technologies," *Renewable and Sustainable Energy Reviews*, vol. 14, pp. 899–918, 2010.

[9] C. Retzler, "Measurements of the slow drift dynamics of a model pelamis wave energy converter," *Renewable Energy*, vol. 31, pp. 257–269, 2006.

[10] "Oscillating water column." https://wiki.uiowa.edu/display/greenergy/Oscillating+Water+Column.

[11] "Yam pro energy." https://yamproenergy.com.

[12] "Wave dragon." https://www.wavedragon.net.

[13] "Powerbuoy, ocean power technologies." https://www.oceanpowertechnologies.com.

[14] E. Enferad and D. Nazarpour, *Ocean's Renewable Power and Review of Technologies: Case Study Waves*. InTech, 2013.

[15] D. Elwood, A. Schacher, K. Rhinefrank, J. Prudel, S. Yim, E. Amon, T. Brekken, and A. von Jouanne, "Numerical modeling and ocean testing of a direct-drive wave energy device utilizing a permanet magnet linear generator for power take-off," in *Proceedings of the 28th International Conference on Ocean, Offshore, and Arctic Engineering*, no. OMAE2009-79146, (Hawaii, USA), 2009.

[16] M. J. Muliawan, Z. Gao, T. Moan, and A. Babarit, "Analysis of a two-body floating wave energy converter with particular focus on the effects of power take-off and mooring systems on energy capture," *Journal of Offshore Mechanics and Arctic Engineering*, vol. 135, p. 031902, 2013.

[17] C. Cochet and R. W. Yeung, "Dynamic analysis ans configuration design of a two-component wave-energy absorber," in *Proceedings of the 31st International Conference on Ocean, Offshore, and Arctic Engineering*, no. OMAE2012-83613, (Rio de Janeiro, Brazil), 2012.

[18] N. Tom and R. W. Yeung, "Performance enhancements and validations of a generic ocean-wave energy extractor," *Journal of Offshore Mechanics and Arctic Engineering*, vol. 135, p. 041101, 2013.

[19] J. A. Oskamp and H. T. Özkan Haller, "Power calculations of a passively tuned point absorber wave energy converter on the oregon coast," *Renewable Energy*, vol. 45, pp. 72–77, 2012.

[20] H. Yavuz, T. J. Stallard, A. P. McCabe, and G. A. Aggidis, "Time series analysis-based on adaptive tuning techiniques for a heaving wave energy converter in irregular seas," *Journal of Power and Energy*, vol. 221, pp. 77–90, 2007.

[21] J. N. Newman, *Marine Hydrodynamics*. Cambridge, Massachusetts: The MIT Press, 1977.

[22] J. V. Wehausen, "The motion of floating bodies," *Annual Review of Fluid Mechanics*, vol. 3, pp. 237–268, 1971.

[23] J. V. Wehausen, W. C. Webster, and R. W. Yeung, *Hydrodynamics of Ships and Ocean Systems*. University of California at Berkeley: Lecture notes for Course ME241, Revised Edition 2016.

[24] E. E. Bachynski, Y. L. Young, and R. W. Yeung, "Analysis and dynamic scaling of tethered wave-energy converters in irregular waves," in *Proceedings of the 30th International Conference on Ocean, Offshore, and Arctic Engineering*, no. OMAE2011-49684, (Rotterdam, The Netherlands), 2011.

[25] E. E. Bachynski, Y. L. Young, and R. W. Yeung, "Analysis and optimization of a tethered wave energy converters in irregular waves," *Renewable Energy*, vol. 8, pp. 133–145, 2012.

[26] N. Tom, *Design and control of a floating wave-energy converter utilizing a permanent magnet linear generator*. PhD thesis, University of California at Berkeley, 2013.

[27] C. Cochet, "Dynamics analysis and configuration design of a two-component wave-energy absorber," Master's thesis, University of California at Berkeley, 2011.

[28] A. Peiffer, "Modeling and evaluation of a wave-energy device - a point absorber with linear generator," Master's thesis, University of California at Berkeley, 2009.

[29] D. Son, V. Belissen, and R. W. Yeung, "Performance validation and optimization of a dual coaxial-cylinder ocean-wave energy extractor," *Renewable Energy*, vol. 92, pp. 192–201, 2016.

[30] F. P. Chau and R. W. Yeung, "Inertia, damping, and wave excitation of heaving coaxial cylinders," in *Proceedings of the 31st International Conference on Ocean, Offshore, and Arctic Engineering*, no. OMAE2012-83987, (Rio de Janeiro, Brazil), 2012.

[31] R. W. Yeung, A. Peiffer, N. Tom, and T. Matlak, "Design, analysis, and evaluation of the uc-berkeley wave-energy extractor," *Journal of Offshore Mechanics and Arctic Engineering*, vol. 134, p. 021902, 2012.

[32] R. W. Yeung, "Added mass and damping of a vertical cylinder in finite-depth waters," *Applied Ocean Research*, vol. 3, no. 3, pp. 119–133, 1981.

[33] D. Son and R. W. Yeung, "Performance predictions and validation of a two coaxial-cylinder system as a wave-energy extractor," in *Proceedings of the 33rd International Conference on Ocean, Offshore, and Arctic Engineering*, no. OMAE2014-24582, (San Francisco, USA), 2014.

[34] L. Wang, D. Son, and R. W. Yeung, "One the performance of a dual-cylinder wave-energy converter: single versus two degrees of freedom," in *Proceedings of the 35th International Conference on Ocean, Offshore, and Arctic Engineering*, no. OMAE2016-54422, (Busan, South Korea), 2016.

[35] L. Wang, D. Son, and R. W. Yeung, "Effect of mooring-line stiffness on the performance of a dual coaxial-cylinder wave-energy converter," *Applied Ocean Research*, vol. 59, pp. 577–588, 2016.

[36] R. W. Yeung and S. H. Sphaier, "Wave-interactino effects on a truncated cylinder in a channel," *Journal of Engineering Mathematics*, vol. 23, pp. 95–117, 1989.

[37] V. Belissen, "Redesign, optimization and fabrication of the supporting structure of the uc-berkeley pmlg system for wave energy extraction," Master's thesis, University of California at Berkeley, 2014.

[38] N. Tom, D. Son, V. Belissen, and R. W. Yeung, "Modeling of a permanent magnet linear generator for wave-energy conversion," in *Proceedings of the 34th International Conference on Ocean, Offshore, and Arctic Engineering*, no. OMAE2015-42370, (St. Johns, Newfoundland, Canada), 2015.

[39] R. W. Yeung and Y. Jiang, "Shape effects on viscous damping and motion of heaving cylinders," *Journal of Offshore Mechanics and Arctic Engineering*, vol. 136(4), pp. 041801–9, 2014.

[40] F. Madhi, M. E. Sinclair, and R. W. Yeung, "The berkeley wedge: an asymmetrical energy-capturing floating breakwater of high performance," *Marine Systems & Ocean Technology*, vol. 9(1), pp. 5–16, 2014, USPTO # 9,416,766.

[41] S. H. Salter, J. R. M. Taylor, and N. J. Caldwell, "Power conversion mechanisms for wave energy," *Proceedings of the Institution of Mechanical Engineers, Part M: Journal of Engineering for the Maritime Environment*, vol. 216(1), pp. 1–27, 2002.

[42] J. Falnes, "Optimal control of oscillation of wave-energy converters," *International Journal of Offshore and Polar Engineering*, vol. 12(2), pp. 147–154, 2002.

[43] U. A. Korde, "Control system applications in wave energy conversion," in *Proceedings of OCEANS 2000 MTS/IEEE Conference and Exhibition*, pp. 1817–1824, 2000.

[44] J. Falnes, *Ocean waves and oscillating systems*. New York, New York: Cambridge University Press, 2002.

[45] A. Babarit and A. H. Clément, "Optimal latching control of a wave energy device in regular and irregular waves," *Applied Ocean Research*, vol. 28, pp. 77–91, 2006.

[46] A. F. de O. Falcão, "Phase control through load control of oscillating-body wave energy converters with hydraulic pto system," *Ocean Engineering*, vol. 35, pp. 358–366, 2008.

[47] F. Kara, "Time domain prediction of power absorption from ocean waves with latching control," *Renewable Energy*, vol. 35, pp. 423–434, 2010.

[48] P. Gieske, "Model predictive control of a wave energy converter: Arcimedes wave swing," Master's thesis, Delft University of Technology, 2007.

[49] T. K. A. Brekken, "On model predictive control for a point absorber wave energy converter," in *Proceedings of the 2011 Trondheim PowerTech Conference*, pp. 1–8, 2011.

[50] J. A. M. Cretel, G. Lightbody, G. P. Thomas, and A. W. Lewis, "Maximisation of energy capture by a wave-energy point absorbr using model predictive control," in *Proceedings of Interantional Federation of Automation Control*, (Milano, Italy), pp. 3174–3721, 2011.

[51] G. Bacelli, J. V. Ringwood, and J.-C. Gilloteaux, "A control system for a self-reacting point absorber wave energy converter subject to constraints," in *Proceedings of 18th IFAC world congress*, pp. 11387–11392, 2011.

[52] J. Hals, J. Falnes, and T. Moan, "Constrained optimal control of a heaving buoy wave-energy converter," *Journal of Offshore Mechanics and Arctic Engineering*, vol. 133, p. 011401, 2011.

[53] J. Hals, J. Falnes, and T. Moan, "A comparison of selected strategies for adaptive control of wave energy converters," *Journal of Offshore Mechanics and Arctic Engineering*, vol. 133, p. 031101, 2011.

[54] M. A. Jama, H. Noura, A. Wahyudie, and A. Assi, "Enhancing the performance of heaving wave energy converters using model-free control approach," *Renewable Energy*, vol. 83, pp. 931–941, 2015.

[55] G. Li and M. R. Belmont, "Model predictive control of sea wave energy converters - part i: a convex approach for the case of a single device," *Renewable Energy*, vol. 69, pp. 453–463, 2014.

[56] M. Richter, M. E. Magana, O. Sawodny, and T. K. A. Brekken, "Nonlinear model predictive control of a point absorber wave energy converter," *IEEE Transactions on Sustainable Energy*, vol. 4(1), pp. 118–126, 2013.

[57] E. Abraham and E. C. Kerrigan, "Optimal active control and optimization of a wave energy converter," *IEEE Transactions on Sustainable Energy*, vol. 4(2), pp. 324–332, 2013.

[58] N. Tom and R. W. Yeung, "Nonlinear model predictive control applied to a generic ocean-wave energy extractor," *Journal of Offshore Mechanics and Arctic Engineering*, vol. 135(4), p. 041901, 2014.

[59] B. Teillant, J. C. Gilloteaux, and J. V. Ringwood, "Optimal damping profile for a heaving buoy wave energy converter," in *8th IFAC Conference on Control Applications in Marine Systems*, pp. 360–365, 2010.

[60] N. Tom and R. W. Yeung, "Experimental confirmation of nonliear-model-predictive control applied offline to a permanent magnet linear generator for ocean-wave energy conversion," *IEEE Journal of Oceanic Engineering*, vol. 99, pp. 281–295, 2015.

[61] W. E. Cummins, "The impulse response function and ship motions," Tech. Rep. Hydromechanics Laboratory Research and Development Report 1661, Department of the Navy David Taylor Model Basin, 1962.

[62] T. F. Ogilvie, "Recent progress towards the understanding and prediction of ship motion," in *The fifth Symposium on Naval Hydrodynamics*, pp. 3–128, 1964.

[63] Z. Yu and J. Falnes, "State-space modelling of a vertical cylinder in heave," *Applied Ocean Research*, vol. 17, pp. 265–273, 1955.

[64] E. Kristiansen and O. Egeland, "Frequency-dependent added mass in models for controller design for wave motion damping," in *Proceedings IFAC Conference on Manoeuvering and Control of Marine Systems*, (Girona, Spain), 2003.

[65] E. Kristiansen, Å. Hjulstad, and O. Egeland, "State-space representation of radiation forces in time-domain vessel models," *Ocean Engineering*, vol. 32, pp. 2195–2216, 2005.

[66] A. Ross, T. Perez, and T. I. Fossen, "Clarification of the low-frequency modelling concept for marine craft," in *Proceedings IFAC Conference on Manoeuvering and Control of Marine Systems*, (Lisbon, Portugal), 2006.

[67] T. Duarte, M. Alves, J. Jonkman, and A. Sarmento, "State-space realization of the wave-radiation force within fast," in *Proceedings of the 32nd International Conference on Ocean, Offshore, and Arctic Engineering*, no. OMAE2013-10375, (Nantes, France), 2013.

[68] T. Perez and T. Fossen, "Time- vs. frequency-domain identification of parametric radiation force models for marine structures at zero speed," *Model, Identification and Control*, vol. 29, pp. 1–19, 2008.

[69] D. R. Herber and J. T. Allison, "Wave energy extraction maximization in irregualr ocean waves using pseudospectral method," in *Proceedings of Interantional Design Engineering Technical Conference & Computer and Information in Engineering Conference*, no. DETC2013-12600, (Portland, Oregon), 2013.

[70] A. Wächer and L. T. Biegler, "On the implementation of a primal-dual interior point filter line search algorithm," *Mathematical programming*, vol. 106(1), pp. 25–57, 2006.

[71] A. Kelman, J. Kong, K. S. Vichik, Chiang, and F. Borrelli, "Blom: the berkeley library for optimization modeling," in *Proceedings of the American Control Conference*, pp. 2900–2905, 2014.

[72] O. M. Faltinsen, *Sea loads on ships and offshore structures*. New York, New York: Cambridge University Press, 1990.

[73] "Arduino products." `https://www.arduino.cc/en/Main/ArduinoBoardMega2560`.

[74] "Solid state relay - cn024d05." `http://www.crydom.com/en/products/pcb-mount-mini-sip/dc-output/cn-serie%s/`.

[75] A. Babarit, "A database of capture width ratio of wave energy converters," *Renewable Energy*, vol. 80, pp. 610–628, 2015.

[76] V. S. Neary, M. Previsic, R. A. Jepsen, M. J. Lawson, Y.-H. Yu, A. E. Copping, A. A. Fontaine, K. C. Hallett, and D. K. Murray, *Methodology for design and economic analysis of marine energy conversion (MEC) techonologies.* Sandia National Laboratories: Sandia Report SAND2014-9040, 2014.

[77] J. Dannenberg, P. Naaijen, K. Hessner, H. V. D. Boom, and K. Reichert, "The on board wave and motion estimator owme," in *Proceedings of international offshore and polar engineering conference*, pp. 424–431, 2010.

[78] M. R. Belmont, J. M. K. Horwood, R. W. F. Thurley, and J. Baker, "Shallow angle wave profiling lidar," *Journal of Atmosphere and Oceanic Techonology*, vol. 24, pp. 115–1156, 2007.

[79] M. R. Belmont, J. M. K. Horwood, R. W. F. Thurley, and J. Baker, "Filters for linear sea-wave prediction," *Ocean Engineering*, vol. 33, pp. 2332–2351, 2006.

[80] U. A. Korde, "Near-optimal control of a wave energy device in irregular waves with deterministic-model driven incident wave prediction," *Ocean Engineering*, vol. 53, pp. 31–45, 2015.

[81] F. Fusco, *Real-time forecasting and control for oscillating wave energy devices.* PhD thesis, National University of Ireland Maynooth, 2012.

[82] F. Paparella, K. Monk, V. Winands, M. F. P. Lopes, D. Conley, and J. V. Ringwood, "Benefits of up-wave measurements in linear shor-term wave forecasting for wave energy applications," in *Proceedings of IEEE conference on control application*, pp. 2048–2053, 2014.

[83] R. Coe and V. S. Neary, "Review of methods for modeling wave energy converter survival in extreme sea states," in *Proceedings of the 2nd Marine Energy Techonology Symposium*, (Seattle, WA), 2014.

[84] Y. Li and Y.-H. Yu, "A systhesis of numerical methods for modeling wave energy converter-point absorbers," *Renewable and Sustainable Energy Reviews*, vol. 16, pp. 4352–4364, 2012.

[85] Q. Zhong and R. W. Yeung, "Wave-body interactions among an array of truncated vertical cylinders," in *Proceedings of the 35th International Conference on Ocean, Offshore, and Arctic Engineering*, no. OMAE2016-55055, (Busan, Korea), 2016.